Impaired nuclear PTEN function drives macrocephaly, lymphadenopathy and late-onset cancer in PTEN Hamartoma Tumour Syndrome

Priyanka Tibarewal^{1,*}, Victoria Rathbone¹, Sarah E Conduit¹, Gala Anastasia Electra Classen¹, Fiona Black¹, Mohammad Amin Danesh¹, Georgia Constantinou¹, Zeinab Asgarian², Koujiro Tohyama³, Nisha Kriplani⁴, Virginia Alvarez Garcia⁴, Elizabeth Foxall¹, Djenat Belarbi^{5,6,7}, Marie Leverve^{5,6,7}, Wayne Pearce¹, Mahreen Adil¹, Zofia Varyova¹, Lucia Conde¹, Adriana Alves¹, Glenn R Masson⁸, Roger L Williams⁸, Adrienne M Flanagan^{9, 10}, Javier Herrero¹, Isra Ahmed Mohamed¹¹, Katerina Stroud¹², Marc Tischkowitz¹², Katherine Lachlan^{13,14}, Cheryl L Scudamore¹⁵, Mark G H Scott^{5,6,7}, Nicholas R Leslie⁴, Nicoletta Kessaris^{2,*}, Bart Vanhaesebroeck^{1,*}

ABSTRACT

PTEN Hamartoma Tumour Syndrome (PHTS), a rare disease caused by germline heterozygous *PTEN* mutations, is associated with multi-organ/tissue overgrowth, autism spectrum disorder and increased cancer risk. Phenotypic variability in PHTS is partly due to diverse *PTEN* mutations and the protein's multifaceted functions. PTEN is primarily a PIP₃ phosphatase regulating PI3K/AKT signalling

¹Cancer Institute, University College London, UK

²Wolfson Institute of Biomedical Research, University College London, UK

³Department of Physiology, School of Dentistry, Iwate Medical University, Yahaba, Japan

⁴Institute of Biological Chemistry, Biophysics and Bioengineering, Heriot Watt University, Edinburgh, UK

⁵Université de Paris, 75014 Paris, France

⁶Institut Cochin, INSERM U1016, 75014 Paris, France

⁷CNRS, UMR8104, 75014 Paris, France

⁸MRC Laboratory of Molecular Biology, Cambridge, UK

⁹Research Department of Pathology, University College London, UK

¹⁰Cellular and Molecular Pathology, Royal National Orthopaedic Hospital, Stanmore, UK

¹¹Cambridge University Hospitals NHS Foundation Trust, Cambridge, UK

¹²Department of Genomic Medicine, National Institute for Health Research Cambridge Biomedical Research Centre, University of Cambridge, Cambridge, UK

¹³Wessex Clinical Genetics Service, University Hospital Southampton, Princess Anne Hospital, Southampton, UK

¹⁴Human Development and Health, Faculty of Medicine, University of Southampton, Southampton, UK

¹⁵Exepathology, Exmouth, UK

^{*}Corresponding authors: p.tibarewal@ucl.ac.uk; n.kessaris@ucl.ac.uk; bart.vanh@ucl.ac.uk

but also maintains chromosomal stability through nuclear functions such as double-strand (ds) DNA damage repair. Here we show that *PTEN-R173C*, a pathogenic variant frequently found in PHTS and somatic cancer, has elevated PIP₃ phosphatase activity that effectively regulates canonical PI3K/AKT signalling. However, PTEN-R173C is unstable and excluded from the nucleus. We generated *Pten^{t/R173C}* mice which developed few tumours during their lifetime, aligning with normal PI3K/AKT signalling. However, they exhibit lymphoid hyperplasia, macrocephaly and brain abnormalities, associated with impaired nuclear functions of PTEN-R173C, demonstrated by reduced dsDNA damage repair. Integrating PHTS patient data with our mouse-model, we propose that defective nuclear functions of *PTEN* variants can predict the onset of PHTS phenotypes, and that late-onset cancer in these individuals may arise from secondary genetic alterations, facilitated by compromised dsDNA repair.

Keywords: PTEN, PI3K, PHTS, cancer, macrocephaly, ASD

SUMMARY STATEMENT

Germline heterozygous *PTEN* mutations are associated with tissue overgrowth, autism spectrum disorder and increased cancer risk; this study presents a mouse model representing recurrent human *PTEN*-variants, to elucidate disease outcomes.

INTRODUCTION

PTEN is a ubiquitously expressed tumour suppressor that shows complete loss of expression in some cancers (e.g. prostate cancer and glioblastoma) and overrepresentation of missense variants in others (e.g. endometrial cancer) (Alvarez-Garcia et al., 2019, Li et al., 1997, Steck et al., 1997, Yehia et al., 2020). Heterozygous germline variants of *PTEN* cause PTEN Hamartoma Tumour Syndrome (PHTS), a rare autosomal dominant disorder. Recent estimates puts the prevalence of PHTS at 1:8000-13,000 (White et al., 2025), 10-20 fold higher than previous estimates (Nelen et al., 1996). Clinical features of PHTS include macrocephaly, developmental delay (DD), autism spectrum disorder (ASD), dermatological pathologies, gastrointestinal (GI) polyps, immune dysfunction and vascular anomalies. Individuals with PHTS also face a significantly increased risk of developing cancers particularly of the breast, endometrium and thyroid (Ngeow and Eng, 2019, Yehia and Eng, 2018), with emerging evidence for non-PHTS cancers such as ovarian and prostate cancer (Schei-Andersen et al., 2025, Yehia et al., 2025).

PTEN predominantly acts as a lipid phosphatase metabolising phosphatidylinositol(3,4,5)trisphosphate (PIP_3) and phosphatidylinositol(3,4)bisphosphate ($PI(3,4)P_2$),

thereby antagonizing PI3K/AKT signalling (Myers et al., 1998). PTEN also has protein-phosphatase activity, reducing phosphorylation of Ser/Thr/Tyr on heterologous protein substrates (Leslie et al., 2009), in addition to auto-dephosphorylating its T366 site (Tibarewal et al., 2012). Nuclear PTEN has been implicated in cell cycle control, dsDNA repair, maintenance of chromatin structure, genome integrity and transcriptional control (Ho et al., 2019, Langdon, 2023).

The functional core of PTEN consists of a catalytic (amino acids (AA) 16-185) and a C2 (AA 186-350) domain (Lee et al., 1999), with mutations differentially impacting PTEN expression and function. 65% of PHTS patients express *PTEN* variants such as deletions, DNA insertions or non-sense mutation leading to STOP codons (such as R130X and R233X) resulting in PTEN truncation and are therefore predicted to cause heterozygous loss-of-expression. The remaining carry heterozygous missense mutations in the phosphatase or C2 domain, leading to altered PTEN function or subcellular distribution (Hendricks et al., 2022, Spinelli et al., 2015). These include mutations in the catalytic pocket resulting in loss of all catalytic activity [e.g. C124 (C124S/R), R130 (R130G/Q/L) and G129 (G129R)] (Lee et al., 1999) or selective loss of PIP₃ phosphatase activity, while retaining protein phosphatase activity (e.g. G129E) (Myers et al., 1998). Missense mutations leading to selective loss of protein phosphatase activity (Y138L/C) have also been described, although these have not been reported in PHTS (Davidson et al., 2010, Tibarewal et al., 2012). Recent reports have shown that a subset of PTEN variants in PHTS (including K289E, D252G, F241S, I101T and others) are excluded from the nucleus and therefore lack PTEN nuclear functions (Langdon, 2023).

The PIP₃ phosphatase activity of PTEN has long been regarded as critical in PHTS pathogenesis, yet other functions of PTEN are now also emerging as important. Various studies have attempted to establish genotype-phenotype associations in PHTS. Limited patient data make it challenging to ascertain the impact of individual variants in driving patient phenotypes. This challenge has been partially overcome by classifying the variants based on their position in the *PTEN* gene and their impact on PTEN expression and function (Lachlan et al., 2007, Leslie and Longy, 2016, Marsh et al., 1998, Marsh et al., 1999, Mighell et al., 2018). Recently, a large paediatric and adult patient cohort study revealed that missense variants are associated with early disease onset, with DD and macrocephaly being the reason for early diagnosis, whereas *PTEN* truncation variants are associated with late onset disease, with cancer being the reason for PHTS diagnosis at later stages in life (Hendricks et al., 2022). However, patient cohort studies have been limited by the variability in age and sex of the individuals, one of the key challenges in rare disease research.

Genetically modified mice have helped overcome some of the challenges in PHTS research by allowing assessment of PTEN functions in an endogenous tissue context (Lee and Pandolfi, 2020). They also serve as a platform for testing potential treatments, such as PI3K pathway inhibitors,

aimed at mitigating the effects of PTEN loss. An example are mice with heterozygous loss of PTEN expression ($Pten^{+/-}$), representing PTEN variants that result in loss of expression and function. This mouse model recapitulates many aspects of human PHTS remarkably well in terms of cancer development and lymphoid and brain overgrowth (Podsypanina et al., 1999, Tibarewal et al., 2022).

Several mouse models have been developed to distinguish the relative importance of the cytosolic *versus* nuclear functions of PTEN (Langdon, 2023). For instance, *Pten*^{m3m4} mice, feature non-naturally occurring *PTEN* mutations that result in a predominantly cytosolic PTEN distribution without affecting its PIP₃ phosphatase activity. These mice have been extensively studied for the impact of the nuclear-cytoplasmic partitioning of PTEN on neuronal and immune phenotypes, although their tumour spectrum has not been reported (Mester et al., 2011, Tilot et al., 2014, Jaini et al., 2020). Other models, expressing PTEN missense variants found in PHTS such as F341V (Caserta et al., 2015), and non-pathogenic mutations such as K13R, Y240F and D384V (Igarashi et al., 2018, Ma et al., 2019), that do not affect the catalytic functions of PTEN but impact its nuclear/sub-cellular localisation, have also been developed, but there is limited or no patient data for these individual variants (**Table 1** and **Table S1**).

Here we report the creation and characterisation of a novel mouse model for PHTS, carrying a *PTEN-R173C* (NM_000314.8(PTEN):c.517C>T (p.Arg173Cys)) missense variant in the germline. R173 is located in the TI (Thr-Ile) loop in the catalytic domain of PTEN important for catalytic activity. *PTEN-R173* variants, mainly *-R173C* and *-R173H* are commonly found in PHTS and in somatic cancers. We have identified 38 PHTS patients with *PTEN-R173* variants (**Table 1** and **Table S2**). In somatic cancers, the PTEN-R173 site is also one of the three frequent mutational hot-spots in *PTEN* with 89 cases with R173C, 83 with R173H, 2 with R173P and R173L, and 1 case each with R173S and a silent mutation reported in the COSMIC database (https://cancer.sanger.ac.uk/cosmic).

We first revisited the impact of this mutation on PTEN expression and function using biochemical and cell-based models and show that PTEN-R173C has reduced protein stability but retains its ability to dephosphorylate PIP₃ and therefore regulate the canonical PI3K/AKT pathway in the cytosol. However, we find that this PTEN mutant is largely excluded from the nucleus.

We created heterozygous germline $Pten^{R173C}$ knock-in mice ($Pten^{+/R173C}$) as a unique model of a frequent pathogenic PHTS PTEN variant representing nuclear-excluded PTEN missense variants. We examined the consequences of this mutation on embryonic development, glucose metabolism, development of PHTS-relevant cancers as well as immune, neurological and behavioural phenotypes. By integrating our findings with phenotypic data from patients for this variant, and by comparison of reported data on the $Pten^{m3m4}$ mice, we delineate the role of the nuclear functions of PTEN in the manifestation of PHTS phenotypes.

RESULTS

Increased PIP₃ phosphatase activity but reduced protein stability of PTEN-R173 mutant proteins upon transient expression in mammalian cells

Conflicting data on the catalytic activity of *PTEN-R173* variants have been published (Han et al., 2000, Post et al., 2020, Smith and Briggs, 2016). PTEN-R173 mutant proteins, expressed in *E. coli*, have been reported to be catalytically inactive (Han et al., 2000) however, mutant PTEN proteins expressed in non-mammalian systems often fail to fold properly, resulting in lack of activity (Spinelli et al., 2015). Consistent with this, in our hands, PTEN-R173C protein expressed in *E. coli* lacked *in vitro* PIP₃ lipid phosphatase activity (**Fig. S1A**) and when expressed in Sf9 insect cells precipitated upon purification (Masson et al., 2016a) (data not shown), rendering it unsuitable for use in *in vitro* assays. Affinity purified GST-PTEN-R173C after transient expression in mammalian Lenti-XTM 293T cells, possesses *in vitro* catalytic activity against soluble PIP₃, albeit lower than PTEN-WT (**Fig. S1B**). Although this assay validates PTEN-R173C as a *bona fide* PIP₃ phosphatase, these *in vitro* conditions limit the ability to fully recapitulate the complexity of plasma membrane-associated PIP₃ metabolism. Crucially, it does not account for potential modulatory effects arising from PTEN's interaction with the plasma membrane. We therefore decided to use cell-based assays that represent the natural lipid substrates for PTEN.

A commonly used assay to determine the ability of PTEN and its mutants to regulate PI3K/AKT signalling involves expression in PTEN-null U-87 MG glioblastoma cell line (further referred to as U87) and assessment of AKT phosphorylation and cell proliferation (Davidson et al., 2010). Transient lentiviral expression of untagged PTEN-R173C in U87 revealed consistently lower expression levels compared to PTEN-WT (**Fig. 1A**, left panel), despite similar mRNA expression levels (**Fig. 1A**, right panel). Similar results were seen with PTEN-R173H.

Expression of a dose range of PTEN proteins in U87 revealed that, compared to PTEN-WT, lower levels of PTEN-R173C or PTEN-R173H effectively downregulated AKT P-S473 phosphorylation (**Fig. 1B** and S1C) and suppressed U87 proliferation (**Fig. 1C** and S2A). We also assessed the impact of PTEN-R173C on recruitment of a PIP₃-biosensor protein to the plasma membrane in U87 cells. In insulinstimulated cells, the biosensor plasma membrane to cytosol ratio (PM:cytosol) was significantly reduced upon treatment with the pan-class I PI3K inhibitor GDC-0941 or upon expression of PTEN-WT or PTEN-R173C, with the strongest decrease upon PTEN-R173C expression (**Fig. 1D** and S2B), despite its lower expression levels compared to PTEN-WT (**Fig. S2C**).

Taken together, these data suggest that in mammalian cells, PTEN-R173C is less stable but catalytically more active than PTEN-WT.

Evidence for a more open, proteolytically-sensitive protein conformation of PTEN-R173 mutants

We next investigated possible biochemical mechanisms underlying the reduced expression of PTEN-R173C. Cycloheximide chase experiments of U87 cells transiently transduced with PTEN expression lentiviruses indicated a reduced protein half-life of PTEN-R173C compared to PTEN-WT (**Fig. 1E, S3A**). A recent study has shown similar findings with PTEN-R173H (Jun et al., 2024).

PTEN protein stability and activity is regulated, in part, by phosphorylation on multiple C-terminal sites (S380/T382/T383/S385) by CK2, resulting in a more closed and stable but less active protein conformation. Dephosphorylation releases the inhibitory effect of these phosphorylated residues on the C2 domain of PTEN, leading to a more open conformation with increased membrane binding and therefore enhanced activity (Torres and Pulido, 2001, Vazquez et al., 2001, Birle et al., 2002, Odriozola et al., 2007, Dempsey et al., 2021). Once at the membrane, the active form of PTEN becomes degraded (Maccario et al., 2010). Upon transient expression of similar levels of untagged proteins in U87 cells, PTEN-R173C showed a ~50% lower level of S380/T382/T383 phosphorylation compared to PTEN-WT (Fig. 1F). Similar data were observed using YFP-tagged Rluc-PTEN-R173C and PTEN-R173H in HEK-293T cells (Fig. S3B), suggesting that reduced phosphorylation may contribute to the observed instability of PTEN-R173 mutants.

A study using computational modelling predicted increased protein flexibility of PTEN-R173C/H mutants, leading to impaired protein stability (Smith and Briggs, 2016). In order to gain insight into these phenomena, we used an intramolecular bioluminescent resonance energy transfer (BRET)-based biosensor Rluc-PTEN-YFP in live HEK-293T and PTEN KO HeLa cells. This biosensor reveals dynamic changes in PTEN conformational rearrangement and function due to shifts in energy transfer between the donor/acceptor couple (Lima-Fernandes et al., 2014) (Fig. S4A-B). Using this approach, PTEN-R173C and PTEN-R173H were found to be in a more open/flexible conformation compared to PTEN-WT (Fig. 1G).

We previously reported that PTEN protein dephosphorylated on S380/T382/T383/S385 is more prone to ubiquitination at Lys66 and degradation (Maccario et al., 2010, Gupta and Leslie, 2016). In line with this, when transiently expressed in U87 cells, the PTEN-R173C/K66R double mutant which cannot be ubiquitinylated, showed increased protein expression levels compared to PTEN-R173C (Fig. 1H).

Altogether these data indicate that the PTEN-R173C protein has a more open conformation that allows ubiquitination and degradation, leading to reduced protein levels.

PTEN-R173 mutants are predominantly cytoplasmic and largely excluded from the nucleus

The tumour suppressor functions of PTEN have been mostly attributed to its ability to regulate the PI3K/AKT pathway, with the role of other PTEN functions such as protein phosphatase activity and nuclear functions less well-studied in this context (Ho et al., 2019). Given that our results so far show that PTEN-R173C/H mutants are effective at regulating the PI3K/AKT pathway, we investigated other PTEN functions to explain the high mutation frequency of this site in somatic cancers and PHTS.

To assess potential alterations in the intrinsic protein phosphatase activity of the PTEN-R173C variant, we quantified phosphorylation levels at threonine 366 (Thr366), a known auto-dephosphorylation site (Tibarewal et al., 2012). Comparative analysis revealed no significant difference in Thr366 phosphorylation between GFP-tagged PTEN-R173C and PTEN-WT, indicating normal protein phosphatase activity. (Fig. S5A).

We next analysed subcellular distribution of PTEN-R173C by transiently expressing C-terminally GFP-tagged PTEN constructs in Lenti-X[™] 293T cells. We observed a significantly lower nuclear:cytoplasmic ratio of the GFP signal in cells expressing PTEN-R173C-GFP than in cells with PTEN-WT-GFP, suggesting that PTEN-R173C was largely excluded from the nucleus (**Fig. 1I**). Nuclear exclusion of the R173 mutants was also revealed upon expression of YFP-tagged Rluc-PTEN-WT, -R173C or -R173H in HEK-293T or PTEN KO HeLa cells (**Fig. S5B**).

Homozygous germline PTEN-R173C expression is embryonically lethal in mice

To study the role of endogenously expressed PTEN-R173C in PHTS, we created heterozygous germline $Pten^{R173C}$ knock-in mice ($Pten^{+/R173C}$) by CRISPR-Cas9 technology (**Fig. S6**). Intercrosses of $Pten^{+/R173C}$ mice did not yield live-born homozygous $Pten^{R173C/R173C}$ mice (**Fig. 2A**). $Pten^{R173C/R173C}$ embryos were reabsorbed at embryonic day (E)11.5, with under-representation compared to Mendelian ratios at earlier time points (**Fig. 2A**). Intact $Pten^{R173C/R173C}$ embryos were found at E9.5 with 5/9 embryos smaller and had not undergone turning, with the remaining 4/9 reabsorbed, suggesting that $Pten^{R173C/R173C}$ embryos die around E9.5 (**Fig. 2A**).

Given the non-viability of homozygous $Pten^{R173C/R173C}$ mice, and the fact that PTEN mutations in PHTS individuals are heterozygous, we used heterozygous $Pten^{+/R173C}$ mice for further investigation. For these studies, we used $Pten^{+/-}$ mice, a well-characterised model for PHTS (Knobbe et al., 2008, Di Cristofano et al., 1998, Suzuki et al., 1998, Podsypanina et al., 1999, Freeman et al., 2006, Di Cristofano et al., 2001) alongside littermate wild-type ($Pten^{+/+}$) mice as controls.

PTEN-R173C expressed from its endogenous promoter is unstable but retains PIP₃ phosphatase activity

To study endogenous PTEN-R173C protein expression and function, we derived mouse embryonic fibroblasts (MEFs) of the following genotypes: $Pten^{+/R173C}$, $Pten^{R173C/R173C}$, $Pten^{-/R173C}$ and compared these to $Pten^{+/-}$, $Pten^{-/-}$ and $Pten^{+/-}$ MEFs.

PTEN protein expression levels in *Pten*^{+/R173C} and *Pten*^{+/-} MEFs were 60-70% of those in *Pten*^{+/+} MEFs (**Fig. 2B**). The PTEN levels observed in *Pten*^{+/-} MEFs agree with previous studies where the *Pten*^{WT} allele was shown to express higher than 50% level of PTEN protein (Alimonti et al., 2010). In *Pten*^{R173C/R173C} and *Pten*^{-/R173C} MEFs, PTEN protein levels were ~13% and ~2%, respectively, of those in *Pten*^{+/+} MEFs (**Fig. 2C and Fig. S7**), indicative of low protein stability of the PTEN-R173C protein, in line with our exogenous expression studies above.

We next assessed PI3K pathway activation, under standard cell culture conditions and upon insulin-stimulation. $Pten^{+/R173C}$, $Pten^{+/-}$ and $Pten^{+/+}$ MEFs growing in complete media showed similar basal levels of phosphorylation of AKT, S6 and other downstream effectors (**Fig. 2B**). Under these conditions, $Pten^{-/-}$ MEFs had increased levels of AKT P-S473, which was not observed in $Pten^{R173C/R173C}$ MEFs (**Fig. 2C**). In $Pten^{-/R173C}$ MEFs, the levels of AKT P-S473 were elevated compared to $Pten^{+/-}$ and $Pten^{+/-}$ MEFs, but still substantially lower compared to $Pten^{-/-}$ MEFs (**Fig. S7**).

Despite the very low levels of PTEN-R173C expression, upon insulin stimulation, there was no increase in AKT P-S473 above basal levels in $Pten^{R173C/R173C}$ MEFs, in contrast to increased AKT P-S473 observed in $Pten^{+/+}$ and $Pten^{-/-}$ MEFs (**Fig. 2D**).

Taken together, these data indicate that, even at low levels of expression, PTEN-R173C is still capable of effectively downregulating unstimulated and insulin-stimulated AKT P-S473 phosphorylation and thus retains overall PIP₃ phosphatase activity.

PTEN-R173C regulates glucose metabolism in vivo

PTEN plays an important role in glucose metabolism by dampening insulin signalling, with *Pten*^{+/-} mice showing enhanced acute insulin signalling and increased glucose metabolism (Chen et al., 2018, Garcia-Cao et al., 2012, Pal et al., 2012). PHTS patients also often show constitutive insulin sensitization (Pal et al., 2012). In line with these reports, insulin tolerance tests on 3-month-old mice revealed enhanced insulin sensitivity in *Pten*^{+/-} mice, evidenced by lower levels of blood glucose post insulin injection compared to *Pten*^{+/+} littermates (**Fig. 2E**). In contrast, *Pten*^{+/R173C} mice showed a similar insulin response up to 60 min after insulin injection (**Fig. 2E**). This indicates that, at the organismal level, PTEN-R173C maintains the ability to downregulate acute insulin/PI3K/AKT signalling and therefore glucose homeostasis (**Fig. 2E**). However, from the 90 min time point

onwards, $Pten^{+/R173C}$ mice showed slightly increased clearance of blood glucose compared to WT littermates (**Fig. 2E**). It is tempting to speculate that this might be due to recruitment of PTEN-R173C to the plasma membrane upon insulin stimulation and associated rapid degradation, with total PTEN protein levels becoming similar as $Pten^{+/-}$ tissues, resulting in an increased insulin sensitivity at these later time points.

Endogenously expressed PTEN-R173C is predominantly nuclear-excluded with reduced ability to regulate dsDNA damage repair

To determine the subcellular distribution of PTEN-R173C upon expression from its endogenous locus, we used immunocytochemistry and quantification of the PTEN nuclear/cytoplasmic ratio in $Pten^{R173C/R173C}$ and $Pten^{-/R173C}$ MEFs. These data showed that PTEN-R173C expressed from its endogenous locus was predominantly nuclear-excluded, in contrast to PTEN-WT protein which was present in both the nucleus and cytoplasm (**Fig. 2F and S8A**). Given that R173 is not located in a known PTEN nuclear localisation signal, one reason for the apparent nuclear exclusion of PTEN-R173C could be sequestration at the plasma membrane, with little protein available for nuclear import. To investigate this, we treated $Pten^{R173C/R173C}$ MEFs with the pan-class I PI3K inhibitor GDC-0941, with the aim to reduce the PIP3 substrate levels for PTEN at the plasma membrane and to potentially restore the presence of PTEN-R173C in the nucleus. However, GDC-0941 treatment did not affect the subcellular distribution of PTEN-R173C (**Fig. S8B**), suggesting that plasma membrane PIP3 levels do not significantly contribute to the nuclear exclusion of PTEN-R173C.

Nuclear PTEN has numerous functions including regulation of DNA repair, transcription, chromatin structure, chromosomal stability and genome integrity by various mechanisms (Ho et al., 2019, Langdon, 2023). We investigated one of these nuclear functions in *Pten*^{+/R173C} mice, namely dsDNA damage repair. Nuclear PTEN deficiency has been shown to cause a homologous recombination (HR) defect in cells, leading to increased γH2AX expression and decreased Rad51 foci formation upon genotoxic stress such as ionizing radiation (IR) (Bassi et al., 2013, Mendes-Pereira et al., 2009, Shen et al., 2007). Analysis of *Pten*^{+/R173C} and *Pten*^{+/-} mice, 5 h post-IR treatment, showed a significant increase in γH2AX levels in protein extracts from uteri, kidney and liver, compared to wild-type mice (**Fig. 2G and S9**), indicative of a similarly reduced dsDNA repair capacity upon heterozygous PTEN loss or heterozygous PTEN-R173C expression. This suggests that PTEN-R173C has a reduced ability to regulate DNA damage repair in these tissues compared to PTEN-WT.

Reduced cancer predisposition of *Pten*^{+/R173C} mice compared to *Pten*^{+/-} mice

Individuals with PHTS have an increased risk of cancers of multiple tissues including breast, endometrium and thyroid (Yehia and Eng, 2018, Yehia et al., 2020, Yehia et al., 2019). To gain insight into the cancer predisposition of germline $Pten^{R173C}$ expression, we aged heterozygous $Pten^{+/R173C}$ mice alongside $Pten^{+/-}$ and $Pten^{+/+}$ littermate controls. We used mice on a mixed C57Bl/6JxSv129 background, as on this background $Pten^{+/-}$ mice develop PHTS-relevant phenotypes, with an overlapping tumour spectrum including hyperplasia/tumours of the thyroid, endometrium, lymphoid tissue, small intestine and adenomyoepithelioma and malignant mammary tumours in the females (Tibarewal et al., 2022). $Pten^{+/-}$ mice also develop lesions not seen in PHTS patients including, pheochromocytoma and intraepithelial neoplasia (PIN) and adenocarcinoma of the prostate (Knobbe et al., 2008, Di Cristofano et al., 1998, Suzuki et al., 1998, Podsypanina et al., 1999, Freeman et al., 2006, Di Cristofano et al., 2001).

Gross morphology and development of $Pten^{+/R173C}$ mice was found to be similar to $Pten^{+/+}$ littermates, with a tendency for a slight increase in body weight at young age in both $Pten^{+/R173C}$ and $Pten^{+/-}$ mice (**Fig. S10**).

Mice were aged and sacrificed at first appearance of signs of ill health or palpable masses. The reasons for humane culling of mice are listed in **Table S3**. Under these experimental conditions, the median survival age of $Pten^{+/R173C}$ mice was 585 and 302 days for male and female mice, respectively. This is significantly longer than the median survival age of 310 and 179 days for male and female $Pten^{+/-}$ mice, respectively (**Fig.3A**). However, $Pten^{+/R173C}$ mice had a shorter lifespan compared to wild-type mice (**Fig.3A**), especially female $Pten^{+/R173C}$ mice, who were mainly euthanised due to palpable masses or ill health.

Histopathological analysis of selected tissues from *Pten*^{+/-} and *Pten*^{+/R173C} mice revealed very similar gross morphologies of all tissues analysed, with overall histopathology data summarized in **Fig. 3B** and **Tables S4-S7**.

Pten^{+/R173C} mice developed far fewer tumours than Pten^{+/-} mice, with occasional hyperplasia of the small intestine (2/14 mice) and low-grade PINs of prostate (4/14 mice), one case of mammary adenocarcinoma (1/22 mice) and one case of endometrial hyperplasia (1/28) (Fig. 3B; Fig. S11-S12; Tables S4 and S5). However, similar to Pten^{+/-} mice, Pten^{+/R173C} mice had a high incidence of pheochromocytoma (Fig. 3B, Fig. S11-S12; Tables S4 and S5).

One out of 28 *Pten*^{+/R173C} mice displayed a single focus of endometrial hyperplasia, with loss of immunostaining for PTEN and increased AKT P-S473 (**Fig. 3C**). Interestingly, loss of PTEN immunoreactivity was also observed in microscopically *normal* endometrial glands from 5-month-old and 10-month-old *Pten*^{+/R173C} mice, but this was not accompanied by a concomitant increase in AKT

P-S473 immunoreactivity in these regions (**Fig. 3C**). In the absence of reagents which allow us to specifically stain for WT or PTEN-R173C protein and, based on the low expression level of endogenous PTEN-R173C protein when expressed alone (**Fig. S7**), it is most likely that expression of the wild-type *Pten* allele is lost in these morphologically normal glands. We speculate that, while the very low expression level of PTEN-R173C from the endogenous allele may not be detectable by IHC, it is still sufficient to partially downregulate PI3K signalling and AKT P-S473 and thereby prevent the development of endometrial tumours. Although this observation is based on a single mouse, we speculate that the hyperplastic gland found in the endometrium of this *Pten*^{+/R173C} mouse may have resulted either from loss-of-expression of the remaining *Pten*^{R173C} allele, or from acquisition of PI3K pathway-activating mutations. These events likely led to PI3K pathway hyperactivation, ultimately contributing to the development of endometrial hyperplasia. This hypothesis is supported by the fact that somatic cancers with the PTEN-R173 mutation, along with mutation of the wild-type allele of *PTEN*, also contain mutations in other cancer drivers such as *PIK3CA* (**Fig. 3D**).

Prominent but delayed lymphoid hyperplasia in Pten+/R173C mice compared to Pten+/- mice

Previous studies have reported a range of lymphoid and immune phenotypes in PHTS patients including peripheral lymphoid hyperplasia, enlargement of tonsils and adenoids, hypogammaglobulinemia, recurrent respiratory tract infection and autoimmune disorders (Chen et al., 2017, Drissen et al., 2024). Some of these phenotypes are found in PHTS patients with *PTEN*-R173 variants and other nuclear-excluded variants (**Table 1** and **Tables S1 and S2**).

In *Pten* mutant mice, including *Pten*^{+/m3m4} mice, lymphoid hyperplasia leads to enlarged cervical, brachial, inguinal and axillary lymph nodes (Podsypanina et al., 1999, Alimonti et al., 2010, Jaini et al., 2020). While this does not cause discomfort to the mice, in our study it was a main reason for sacrificing *Pten*^{+/-} mice (75% males and 80% females) and many *Pten*^{+/R173C} mice (21% males and 50% females), due to animal welfare regulations on the allowed tissue overgrowth size (**Table S3**).

Histological analysis revealed a similar severity grade of hyperplasia (assessed by semi-quantitative histopathological scoring) in female $Pten^{+/R173C}$ and $Pten^{+/-}$ mice but of significantly lower grade in $Pten^{+/R173C}$ males than $Pten^{+/-}$ males (**Fig. 3E**).

Flow cytometry analysis of lymph nodes of 5-month-old female $Pten^{+/-}$ and 10-month-old female $Pten^{+/R173C}$ mice, the age at which they have visibly enlarged lymph nodes, compared to littermate $Pten^{+/+}$ mice, revealed a significant increase in the proportion of B-cells and a corresponding decrease in T-cell proportions (**Fig. 3F-G**), a phenotype also reported in $Pten^{+/m3m4}$ mice (Jaini et al., 2020).

Macrocephaly, increased neuronal size and white matter disturbances in Pten^{+/R173C} mice

PHTS patients, including the majority of patients with PTEN-R173 mutations (**Table S2**), commonly present with macrocephaly, DD and ASD. We therefore explored neurological and behavioural phenotypes in $Pten^{+/R173C}$ mice.

We examined the brains and neurons from $Pten^{+/+}$, $Pten^{+/R173C}$ and $Pten^{+/-}$ mice and, where possible, conditional knock-out mice that selectively lack PTEN expression in cortical pyramidal neurons (referred to here as cKO)(Kessaris et al., 2006, Lesche et al., 2002). These cKO mice were further crossed to $Pten^{+/R173C}$ mice to obtain conditional knock-in mice (referred to here as cKI) which express PTEN-R173C in cortical pyramidal neurons without a copy of the PTEN-WT allele and hence are overall hemizygous for the $Pten^{R173C}$ allele ($Pten^{-/R173C}$). The observed phenotypes are summarized in **Table 2**, which also shows a comparison to phenotypes published for $Pten^{m3m4}$ mice. The latter models germline expression of non-naturally occurring PTEN mutations that leave PTEN PIP₃ phosphatase activity intact, but leads to its nuclear exclusion, and whose neuronal phenotypes have been extensively characterised (Mester et al., 2011, Tilot et al., 2014, Jaini et al., 2020).

We first assessed the levels of PTEN protein and downstream pathways in protein lysates from cortical neurons. In the absence of a PTEN-WT allele, the level of PTEN protein in cKI was minimal and similar to that seen in protein extracts of cKO mice (Fig. S13A-B). However, the level of AKT P-S473 in cKI brains was significantly lower compared to the cKO mice (Fig. S13A and C). These observations mirror our data in MEFs (Fig. S7), indicating that PTEN-R173C is also highly active in the brain despite its low level of expression.

At 3 months of age, $Pten^{+/R173C}$ and $Pten^{+/-}$ mice of both sexes had enlarged brains with increased mass compared to $Pten^{+/+}$ littermates (**Fig. 4A-B**), indicating a macrocephalic phenotype. Also, at 3-and 6-months of age, and independent of the genetic background, $Pten^{+/R173C}$ and $Pten^{+/-}$ mice showed a similar increase in brain mass (**Fig. S14**). Given the apparently normal PI3K/AKT regulatory capacity of PTEN-R173C, and the neurological phenotypes and macrocephaly previously observed in nuclear-excluded PTEN in heterozygous $Pten^{+/m3m4}$ and homozygous $Pten^{m3m4/m3m4}$ mice (Mester et al., 2011, Tilot et al., 2014), these observations allow us to postulate that the nuclear function of PTEN is key to the development of macrocephaly.

We next quantified several brain parameters to characterize the macrocephalic phenotype. $Pten^{+/R173C}$ mice had increased cortical thickness as measured at the level of the somatosensory barrel field (**Fig. 4C-D**). A significant increase was also observed in the thickness of the corpus callosum at four different Bregma levels (**Fig. 4E**) in both $Pten^{+/R173C}$ and $Pten^{+/-}$ mice. Consistent with macrocephaly, a lengthwise enlargement of the corpus callosum at Bregma levels together with an increase in the thickness and total area were also observed (**Fig. 4F**). The increased thickness of the

cortex was not caused by increased neuronal cell numbers or neuronal densities in $Pten^{+/R173C}$ mice (**Fig. 4G**). In contrast, immunohistochemistry for OLIG2 revealed a small but significant increase in oligodendrocyte lineage cell numbers (**Fig. 4H**). Interestingly, this increase was not seen in our $Pten^{+/-}$ mice and has not been reported in $Pten^{+/m3m4}$ mice but was observed in $Pten^{m3m4/m3m4}$ mice (**Table 2**). Astrocyte overabundance and astrogliosis, as detected by GFAP immunostaining, were not observed (**Fig. 4H**). However, astrogliosis has been reported in $Pten^{m3m4/m3m4}$ mice (**Table 2**), suggesting that the remaining wild type Pten allele protects the brain from this immunoinflammatory phenotype.

To gain further insight into the causes of macrocephaly, we quantified neuronal and glial parameters *in vitro*. Morphologies of cortical pyramidal neurons *in vitro* were assessed following transfection with a GFP expression vector to allow visualisation of the cells (**Fig. 5A**). $Pten^{+/R173C}$ neurons had enlarged cell body size and a tendency for increased process complexity (not statistically significant) compared to $Pten^{+/+}$ controls (**Fig. 5B,C**). While cKO neurons demonstrated a more severe phenotype, comparable to $Pten^{m3m4/m3m4}$ mice with regards to cell body size (**Table 2**), this phenotype was not observed in $Pten^{+/-}$ neurons (**Fig. 5B,C**) or $Pten^{+/m3m4}$ neurons (**Table 2**).

To determine whether glial and/or axonal defects contribute to the enlargement of the white matter, we examined the corpus callosum of $Pten^{+/+}$, $Pten^{+/R173C}$ and $Pten^{+/-}$ mice using transmission electron microscopy (**Fig. 5D**). While there was no statistically significant difference in the average axonal diameter in $Pten^{+/R173C}$ mice compared to controls, there was a reduction in the number of small diameter axons and a gain of larger diameter axons (**Fig. 5E**). This phenotype was much less pronounced in $Pten^{+/-}$ mice (**Fig. 5E**). Quantification of the G-ratio in the corpus callosum showed an increase in average myelin thickness in both $Pten^{+/R173C}$ and $Pten^{+/-}$ mice (**Fig. 5F**). However, scatter plot analysis of the g-ratio as a function of axonal diameter did not show significant changes in either $Pten^{+/R173C}$ and $Pten^{+/-}$ mice compared to controls (**Fig. 5G**).

Altogether, our experiments show that the macrocephalic *Pten*^{+/R173C} phenotype is caused by alterations in multiple parameters, including increases in neuronal cell body size, axonal thickness, oligodendrocyte lineage cell numbers and myelin thickness.

Pten^{+/R173C} mice have a similar degree of macrocephaly as Pten^{+/m3m4} heterozygous mice and have multiple neuronal phenotypes, partially overlapping with Pten^{m3m4/m3m4} and Pten^{+/-} mice (**Table 2**). Importantly, the apparently intact or even increased PI3K/AKT regulatory capacity of PTEN-R173C, and the phenotypic overlap with Pten^{m3m4} mice, suggests that the impaired nuclear function of PTEN is key to the development of macrocephaly and several neuronal phenotypes.

Defective dsDNA damage repair is increasingly being associated with macrocephaly and ASD with studies showing increased dsDNA breaks in cells isolated from these patients (Wang et al., 2020, Attia et al., 2020). To explore the possible involvement of impaired dsDNA damage repair in neurons

in the macrocephalic phenotype, we treated $Pten^{+/-}$ and $Pten^{+/R173C}$ mice with IR and examined the levels of γ H2AX in the brain 5 h post-IR treatment. While there was an increase in the γ H2AX levels in protein extracts from the brains of both $Pten^{+/-}$ and $Pten^{+/R173C}$ mice, compared to that seen in littermate wild-type mice, the difference observed was not statistically significant (**Fig. S15**). This might be due to the IR dosage and/or time of analysis and warrants further investigation.

Pten+/R173C mice display mild behavioural aberrations

ASD is common in PHTS (Yehia et al., 2020). Behavioural abnormalities are found in mice with germline expression of heterozygous loss-of-function of *Pten* (Clipperton-Allen and Page, 2014) or homozygous expression of the nuclear-excluded *Pten*^{m3m4} mutations (Tilot et al., 2014). To examine this in *Pten*^{+/R173C} mice, we used a range of tests associated with ASD-like mouse behaviours.

In Crawley's sociability test, *Pten**/R173C mice were indistinguishable from *Pten**/+ littermate controls, indicating normal social interactions (**Fig. S16A-D**). In the open field test, male mice were not significantly different from their *Pten**/+ littermates with regards to distance travelled and time spent moving (**Fig. S17B,C**). However, female *Pten**/R173C mice travelled less and spent less time moving than controls (**Fig. S17F,G**), suggesting decreased exploratory behaviour and/or locomotion. This was not caused by increased anxiety since female (and male) mice spent equal length of time exploring the different compartments of the open field test as controls (**Fig. S17D,H**), with defecation during the test being comparable between the two groups (**Fig. S17E,I**). Reduced exploratory locomotion in females was also observed in a hole board test (**Fig. S18A**). Changes in repetitive behaviours, as assayed in a marble burying test were absent in both males and females (**Fig. S18B**).

PHTS patients with nuclear excluded PTEN variants develop malignant cancers later in life

To understand the impact of *PTEN* variants such as *PTEN-R173C* on PHTS pathogenesis, we collated patient phenotype information from published sources, from the PHTS Patient Registry UK, and from personal communication with physicians who see PHTS patients. These have been summarised in **Table 1** with details in **Tables S1 and S2**. Most patients received PHTS diagnosis at young age due to presentation of phenotypes such as macrocephaly (53/59), DD (34/59) and cutaneous pathology (28/59) seen at a high frequency. Patients developed various benign lesions with a moderate frequency such as thyroid cysts or adenomas (10/59) and GI polyps (9/59). Other benign lesions such as endometrial polyps and fibroids, ovarian cysts and lipomas were seen at low frequencies. Vascular malformations, including haemangiomas, venous malformations, arterio-venous malformations were also seen in adult patients (8/59).

Malignant cancer was seen in few patients with onset later in life. With the exception of one 29-year-old male patient with *PTEN-D310G* variant who developed thyroid and testicular cancer, most patients were above the age of 50. This included two female patients with *PTEN-R173C*, one 63-year-old patient who had developed malignant cancers of the breast, skin and ovary, and a 59-year-old patient with malignant cancers of breast and thyroid. A 54-year-old female patient with *PTEN-R173H* variant developed malignant breast cancer.

The clinical observations in *PTEN-R173* PHTS patients mirror the phenotypes of $Pten^{+/R173C}$ mice; while most patients display neurodevelopmental phenotypes early on in life, they develop malignant cancers at a low frequency.

DISCUSSION

Since the discovery of *PTEN* as a tumour suppressor in somatic cancer, multiple genetic mouse models targeting *Pten* have been generated, highlighting the importance of PIP₃ phosphatase activity of PTEN in tumour suppression, embryonic development, immunomodulation, neuronal development and the development of autism spectrum traits (Lee and Pandolfi, 2020).

Mouse models have also improved our understanding of PHTS, a rare genetic condition caused due to heterozygous germline *PTEN* mutations. These include *Pten*^{+/-} mice which represent the heterozygous genetic constellation of *PTEN* in PHTS, and on a mixed C57BL6xSv129 background develop multiple phenotypes overlapping with the clinical presentation of PHTS, including brain and lymphoid overgrowth and the development of specific cancers (Tibarewal et al., 2022). While the PIP₃ phosphatase activity of PTEN has been the focus of research over the last three decades, there is an increasing body of evidence for other PTEN functions in disease pathogenesis, in particular its nuclear function (Langdon, 2023). Recently, the *Pten*^{m3m4} mouse model with germline expression of an engineered, nuclear-excluded non-naturally-occurring *Pten* mutations, has indicated a role for nuclear PTEN defects in driving neuronal and immune phenotypes in PHTS (Tilot et al., 2014, Jaini et al., 2020).

In this study, we developed a new mouse model featuring the pathogenic *PTEN-R173C* variant commonly found in PHTS and somatic cancer. We report that this *PTEN* variant retains its ability to regulate PI3K/AKT signalling but is impaired in dsDNA damage repair through HR, likely due to nuclear exclusion. Contrary to previous reports (Han et al., 2000, Smith and Briggs, 2016, Post et al., 2020), we found that PTEN-R173 mutant proteins (R173C and R173H) were catalytically more active PIP₃ lipid phosphatases than PTEN-WT, both in cells and tissues. However, these mutants displayed reduced protein stability, possibly resulting from a more open protein configuration that is more

susceptible to ubiquitination-mediated degradation. Upon heterozygous germline expression in $Pten^{+/R173C}$ mice, this biochemical feature results in PTEN protein expression levels comparable to those in $Pten^{+/-}$ mice but an overall lipid phosphatase activity similar to wild-type mice, as demonstrated by effective downregulation of insulin-stimulated PI3K/AKT signalling.

To assess the importance of nuclear functions of PTEN in tumourigenesis, we aged Pten+/R173C mice and found only a modest predisposition to solid tumour development compared to Pten+/mice. This is reminiscent of mouse models of genes involved in dsDNA damage repair via HR such as Brca, Rad51 and Palb (Matos-Rodrigues et al., 2021, Tsuzuki et al., 1996, Roy et al., 2011, Rantakari et al., 2010, Yan et al., 2004, Hakem et al., 1996). Indeed, while homozygous inactivation of these genes frequently leads to embryonic lethality, as also observed in PtenR173C/R173C mice, their heterozygous inactivation only leads to a very low to absent tumour burden, most likely because the lifespan of mice is insufficiently long to accumulate the additional mutations required for tumourigenesis (Drost and Jonkers, 2009). That additional genetic defects may be required to allow phenotypic output of PTEN-R173 defects is indicated by the observation that somatic cancers with PTEN-R173 mutation have a range of co-occurring mutations, including but not limited to oncogenic mutation in PIK3CA or loss of second allele of PTEN (Fig. 3D). Also mouse models carrying a combination of Pten mutations with other oncogenic drivers such as mutant Pik3ca and ErbB2 have accelerated development of mammary tumours (Kato et al., 2020, Yip et al., 2020). Combining the Pten-R173C mutation in mouse models carrying additional cancer drivers (such as PIK3CA mutation) or defects in DNA repair genes (such as Brca or Rad51) could provide evidence for this speculation, but such experiments are outside the scope of the current study.

Our data further show that, in a germline configuration, deficient nuclear localisation of PTEN, and consequently its nuclear function, is associated with brain and lymphoid overgrowth. The role of nuclear PTEN in regulating these phenotypes has been reported but the mechanism by which nuclear PTEN regulates these phenotypes is unclear. $Pten^{+/m3m4}$ mice expressing a nuclear excluded Pten mutant develop macrocephaly and lymphadenopathy (Jaini et al., 2020, Mester et al., 2011, Tilot et al., 2014). Increased neuronal cell body size has also been reported in neurons expressing other nuclear excluded PTEN variants such as PTEN-F241S, D252G, N276S and W274L (Fricano-Kugler et al., 2018). On the contrary, mice expressing nuclear excluded, non-pathogenic, Pten mutations such as $Pten^{K13R/D384V}$ have smaller neurons and develop microcephaly (Kato et al., 2021, Igarashi et al., 2018). The discrepancy between these studies may result from mutation-specific changes in PTEN function.

While our study does not establish a direct link between these overgrowth phenotypes in our mice and dsDNA damage repair, it is possible that such a link exists. Indeed, one study reported increased IR-induced DNA strand breaks in lymphocytes from autistic children compared to non-

autistic controls supporting such a functional link (Attia et al., 2020). On the other hand, lymphoid cells isolated from PHTS patients with PTEN-R173C mutation, who all present with ASD, did not exhibit increased DNA damage following IR treatment (Wei et al., 2024). This suggests that nuclear functions of PTEN other than dsDNA repair may underlie the observed lymphoid overgrowth and macrocephaly in our *Pten*^{+/R173C} mice. This is further supported by the absence of lymphoid overgrowth and macrocephaly in patients and mouse models with germline mutations in other genes regulating dsDNA damage repair by HR, such as the *Brca*, *Rad51* and *PalB2* genes.

We find that the macrocephalic *Pten*^{+/R173C} phenotype is associated with alterations in multiple parameters, including increases in neuronal cell body size, axonal thickness, oligodendrocyte lineage cell numbers and myelin thickness. While these brain alterations in *Pten*^{+/R173C} mice are very clear, their impact on animal behaviour is less prominent. It has to be said that while mice with heterozygous germline expression of *Pten* accurately reflect the genetic makeup of patients with PHTS, the behavioural abnormalities observed in heterozygous mutant mice are often subtle and highly variable (Clipperton-Allen and Page, 2014). This necessitates the use of large mouse numbers to achieve quantifiable significant differences between genotypes. Consequently, the field of behavioural analysis has mostly relied on the use homozygous mouse models. This approach is particularly true for PHTS models, with numerous studies conducted on homozygous brain-specific *Pten* knockout models (Kwon et al., 2006, Zhou et al., 2009) and homozygous *Pten*^{m3m4} models (Tilot et al., 2014). Similar homozygous models are also utilized in behavioural research on other rare diseases such as Tuberous Sclerosis (Yuan et al., 2012, Bateup et al., 2013). Although these models do not share the exact genetic composition of patients, they serve as platforms for behavioural and neurological studies and testing therapeutics.

Our study suggests that the status of nuclear function of PTEN alongside its PIP₃ phosphatase activity, allows refinement of genotype/phenotype analysis in PHTS. Based on our findings and assessment of patient phenotypes (**Table 1** and **Tables S1 and S2**), our data indicate that individuals carrying *PTEN* variants such as *PTEN*^{R173C} that retain their PIP₃ phosphatase function but are nuclear-excluded tend to follow a characteristic progression of known PHTS disease phenotypes: early-signs such as neurological abnormalities – including macrocephaly and global developmental delay - alongside cutaneous features which together lead to a PHTS diagnosis during childhood. As they enter early adulthood, they may be prone to developing vascular abnormalities and benign tumours in the thyroid and GI tract, with an increased likelihood of developing malignant cancers later in life.

Our study also highlights the possibility of new therapeutic treatments for cancer in PHTS patients. A previous study has shown that glioma cells expressing PTEN-Y204F, a mutation that leads to lack of PTEN nuclear localisation and functions such as dsDNA damage repair are sensitive to

radiation therapy (Ma et al., 2019). It is therefore tempting to speculate that radiation therapy and dsDNA damage repair antagonist drugs, such as *PARP* inhibitors, might be additional therapeutic options beyond PI3K pathway inhibitors for cancer in PHTS patients carrying *PTEN-R173* like variants.

Methods

Plasmids. DNA constructs are detailed in **Table S8**. Point mutations were introduced in PTEN WT cDNA in different vectors using primers listed in **Table S9** and KOD hot start DNA polymerase (Sigma-Aldrich) using the manufacturer's instructions.

Mice. All mice were maintained at University College London in accordance with the UK Animals (Scientific Procedures) Act 1986 and following UK Home Office guidance. All procedures were authorized by a UK Home Office Project Licence subject to local ethical review. Pten+/- mice (Pten^{tm1Rps}, MGI:2151804 (Podsypanina et al., 1999), Pten^{flox/flox} mice (Pten^{tm1Hwu}, MGI:2156086 (Lesche et al., 2002), CAG CreER^{T2} mice (Gt(ROSA)26Sor^{tm3(CAG-Cre/ERT2)Dsa}, MGI:5616874) (Schonhuber et al., 2014) and Emx1-Cre mice (Tg(Emx1-cre)1Wdr, MGI ID:3761167) (Kessaris et al., 2006) have been described elsewhere. Pten+/R173C mice were generated by Taconic Biosciences using a CRISPR/Cas9 approach. gRNA was designed to contain the R173C mutation (c.517C>T) and a silent mutation containing the EcoNI restriction site upstream of the R173 site (to allow discrimination of wild-type and knock-in allele following PCR). Fig. S6 shows the gRNA sequence and the targeting strategy. gRNA was microinjected into C57BL/6J mouse zygotes along with recombinant Cas9. The zygotes were then transferred to pseudo-pregnant mothers. The litters born (founder animals) were sequenced to check for the incorporation of the R173C mutation and percentage of mosaicism. They were then used to as a breeder to generate F1 animals. F1 males positive for the R173C mutation and negative for any off-target mutations were used to generate further animals by IVF using C57BL/6J females. All mouse lines were maintained on a C57BL/6J background. Sv129 mice were purchased from Charles River or Envigo. Pten+/- and Pten+/R173C mice were crossed with Sv129 mice to obtain mixed background F1 mice that were used for some experiments as described. For neuronal studies, conditional knock-out mice that selectively lack PTEN expression in cortical pyramidal neurons were generated by crossing Pten^{flox/flox} mice with Emx1-Cre mice to give Emx1-Cre;Pten^{fl/fl}; referred to here as cKO. The cKO mice were crossed with Pten+/R173C mice to obtain Emx1-Cre;Pten^{fl/R173C}, referred to here as cKI, which express one only copy of Pten-R173C in the cortical pyramidal neurons.

For genotyping, mouse tissue samples (from ear biopsy or from the embryonic yolk sac) were lysed in 25 mM NaOH/0.2 mM disodium EDTA for 1 h at 95°C. The samples were neutralized by adding an equal volume of a buffer containing 40 mM Tris-HCl, pH 4.5. Two μ l of the DNA extract was used for PCR using and Titanium polymerase PCR kit (Takara) and primers listed in **Table S10**. For genotyping of *Pten*^{+/R173C} mice, an additional restriction digestion step was performed on the PCR products using *Eco*NI (New England Biolabs).

Mouse survival studies. For sample size calculations for long term survival study, we use ClinCalc (www.clincalc.com). The mean survival age of *Pten*^{+/-} on a mixed C57BL6J x Sv129 background has been reported to be 12±1.8 months (Alimonti et al., 2010). The sample size required for *Pten*^{+/R173C} mice needed to see a 15% improvement in mean survival age compared to *Pten*^{+/-} mice was calculated as 16 (probability of Type-I error was set to 0.05 and Power was set to 80%). We used at least 16 mice for each genotype and each sex. At least 10 Littermate wild type mice were used for both *Pten*^{+/-} and *Pten*^{+/R173C} mice. For survival analysis, mice were weighed twice a week. They were monitored and euthanized upon showing a more than 20% reduction in body weight, any signs of ill health such as hunched appearance, laboured breathing, sluggish behaviour, or palpable masses with a total surface area of 1.4 cm² surface area. Animals showing no clinical signs were euthanized at the end of the study (600 days for females and 730 days for males).

Cell lines. U-87 MG (U87), HEK-293T and Phoenix cells were purchased from ATCC, Lenti-X™ 293T cells were purchased from Clontech. Human PTEN knockout HeLa cell line and control HeLa cells was obtained from Abcam (ab255419 and ab255928); PTEN knockout was validated using western blotting (**Fig. S4C**). All cell lines were maintained in DMEM (Sigma-Aldrich), supplemented with 10% Filtered Bovine Serum (FBS) (Pan-Biotech) and Pen-Strep (Sigma-Aldrich) using standard cell culture methods. All cell lines were routinely tested for mycoplasma contamination.

Preparation of MEFs. For preparation of E13.5 MEFs, timed matings were set up between $Pten^{+/-}$ mice and $Pten^{+/R173C}$ mice, $Pten^{flox/+}CreER^{T2}$ and $Pten^{+/-}$ or $Pten^{+/R173C}$ mice. Pregnant females were euthanized on day 13.5 and embryos harvested from the uterus. Following removal of the head and visceral organs, the rest of the embryo was minced in 2x Trypsin/EDTA using a sterile scalpel and incubated at 37°C for 40 min. The cell suspension was plated on 10 cm dishes in DMEM (Sigma-Aldrich) medium supplemented with 10% FBS (Pan-Biotech) and Pen-Strep (Sigma-Aldrich), and cells maintained using standard cell culture procedures. For preparation of E9.5 MEFs, timed intercrosses were set up between $Pten^{+/R173C}$ mice. Pregnant females were euthanized on day 9.5, embryos

removed from the uterus and gently dissociated by pipetting up and down using a p1000 pipette and 2 ml of media containing DMEM (Sigma-Aldrich), supplemented with 10% FBS (Pan-Biotech) and Pen-Strep (Sigma-Aldrich). The cell suspension was plated in 48-well plates and cells maintained using standard cell culture procedures. To induce Cre-mediated recombination of the floxed *Pten* allele in *Pten*^{flox/+}*CreER*⁷² MEFs, 4-hydroxy tamoxifen (Sigma Aldrich) was added to the cells at a final concentration of 1 μM and refreshed every 24 h for 3 days.

Primary neuron culture. Primary cortico-hippocampal cultures were prepared from P1 or P2 pups after genotyping. Cortex and hippocampus were dissected, digested with Trypsin, dissociated using glass pipettes and 40,000 cells were plated per 12 mm coverslip. Neurons were cultured in serumfree medium (neurobasal, NBA) medium supplemented with B27 supplement, L-glutamine, penicillin/streptomycin and 10 mM HEPES pH 7.4. Cells were cultured at 5% CO2 at 37°C with replacement of half of the medium every 2-3 days. Cells were transfected on DIV6 with a GFP expression vector using Lipofectamine 3000 according to the manufacturer's instructions. On DIV 12/13 cells were fixed with 4% PFA/4% sucrose in PBS for 10 min at room temperature (RT) and washed 3x in PBS. Cells were blocked and permeabilized in immunofluorescence (IF) buffer (PBS supplemented with 0.3% Triton X and 3% BSA) for 20 min and incubated with primary antibodies to NeuN (Millipore MAB377 and GFP, Abcam 1:1000) for 2 h at RT in IF buffer in a humidity chamber. After 3 washes with PBS, cells were incubated with cross-absorbed Alexa Fluor labelled secondary antibodies (Invitrogen) in IF buffer for 1 h at RT in a humidity chamber in the dark, washed 3x with PBS and mounted with Immunomount. Neurons were imaged using a LSM 880 microscope (Leica) acquiring Z-stacks at 40 x magnification. Dendritic complexity was determined using the Sholl macro in FIJI. Interceptions were analysed in 10 µm radii within a 200 µm distance from the centre of the soma. To measure cell body size in FIJI, stacks were processed to z-projections, ROIS were drawn manually around the cell bodies and the ROI area was measured in FIJI.

PTEN activity assays. For purification of bacterially-expressed GST-tagged PTEN proteins, pGEX6P1 vectors with cDNA for WT or mutant PTEN were introduced in *E. coli* and recombinant PTEN was purified by glutathione-affinity chromatography followed by cleavage of the GST tag as described (Davidson et al., 2010). PIP₃ assays using purified recombinant PTEN were performed with diC8 PIP₃ (Cell Signals Inc) and malachite green phosphate assay kit (Sigma Aldrich) and have been described elsewhere (Maehama and Dixon, 1998). Purification of recombinant PTEN protein from insect cells was as described in Ref.(Masson et al., 2016b).

Lentiviruses and retroviruses. Lentiviruses for PTEN and PIP₃ biosensor were generated by cotransfecting Lenti-X™ 293T cells or HEK-293T cells with plasmids expressing the cDNA of interest along with packaging vectors using TransIT-LT1 following the manufacturer's instructions. For preparation of retroviruses, Phoenix cells were transfected with p53 shRNA expressing vector (Dickins et al., 2005) using TransIT-LT1 following the manufacturer's protocol. 24 h post transfection, sodium butyrate was added to the cells to a final concentration of 12.5 mM for 6 h, followed by washing the cells with warm PBS and addition of fresh media. The supernatant containing lentiviral particles was collected after 20 h, passed through a 0.45 μm filter and stored at -80°C. Target-cells for transductions were plated at 40-50% confluency. Once the cells had attached, lentiviral/retroviral particles were added to the cells along with polybrene (Sigma-Aldrich) at 20 μg/μl. The media was changed 24 h post transduction.

Immunoblotting analysis. Protein extracts from cell cultures were prepared by scraping cells into lysis buffer containing 25 mM Tris-HCl pH 7.4, 150 mM NaCl, 1% Triton X-100, 10% glycerol, 1 mM EGTA, 1 mM EDTA, 5 mM sodium pyrophosphate, 10 mM β-glycerophosphate, 50 mM sodium fluoride, 1 mM sodium orthovanadate, 1 mM DTT and Protease inhibitor cocktail (Millipore). Mouse tissues harvested from mice upon euthanasia were homogenize using Lysing Matrix M tubes (MP Biomedicals) in double the volume (v/w) of lysis buffer (25 mM Tris-HCl pH 7.4, 150 mM NaCl, 1% Triton X-100, 0.1% SDS, 10% glycerol, 1 mM EGTA, 1 mM EDTA, 10 mM sodium pyrophosphate, 20 mM β-glycerophosphate, 100 mM sodium fluoride, 2 mM sodium orthovanadate, 1 mM DTT and protease inhibitors) on a FastPrep 24 homogeniser (MP Biomedicals) at 4 m/sec for 20 sec. Cell or tissue lysates were pre-cleared by centrifugation at 20,000xg for 10 min and protein extracts analysed by immunoblotting. 293T cells expressing Rluc-PTEN-YFP constructs were lysed in buffer containing 50 mM HEPES (pH 7.4), 250 mM NaCl, 2mM EDTA, 0.5% NP-40, 10% glycerol supplemented with protease and phosphatase inhibitors (Roche) and protein A/G PLUS-Agarose (30µl/IP) and GFP antibody (Roche, Cat #11814460001, Mouse, Dilution 1:200) was used to immunoprecipitate YFP-tagged PTEN protein which was used for immunoblotting as described below. Protein gel electrophoresis was conducted with 10 µg of total soluble protein per lane on NuPage Bis-Tris 4-12% gradient polyacrylamide gels (Thermofisher Scientific) following the manufacturer's protocols. Proteins were transferred onto PVDF membrane (Millipore) and membranes blocked in 5% milk powder/TBST for 1 h at RT. Blocked membranes were incubated overnight with primary antibodies (Table S11). Antibody complexes were detected by 1 h incubation at RT with HRP-conjugated secondary antibodies (GE healthcare). Blots were developed with

Immobilon Forte Western HRP substrate (Millipore) and chemiluminescence imaged using an ImageQuant LAS4000 imaging system (GE healthcare).

qRT-PCR assays. Total RNA was extracted from U87cells non-transduced or transduced with lentiviruses for PTEN-WT, PTEN-C124S, PTEN-R173C or PTEN-R173H, using RNAEasy kit (Qiagen) following the manufacturer's instructions. 1 µg of RNA was converted to cDNA using iScript RT kit (BioRad). 50 ng of cDNA was used for QRT-PCR reactions using primers in **Table S12**. The reactions were run on a QuantStudio™ 5 Real-Time PCR machine (Applied Biosystems). dCT was calculated by deducting the CT for GAPDH from CT of PTEN. ddCT was calculated by deducting the dCT of untransduced cells from the dCT of the sample of interest.

Cycloheximide chase studies. U87 cells were transduced with lentiviruses for PTEN-WT, PTEN-C124S, PTEN-R173C or PTEN-D252G. 48 h post transduction, cells were treated with 200 μ g/ml cycloheximide, lysed at different time points and protein extracts analysed for PTEN expression by immunoblotting.

BRET assays. BRET assays using the Rluc-PTEN-YFP biosensor were performed as described in Refs (Misticone et al., 2016, Lima-Fernandes et al., 2014). Briefly, 24 h post-transfection, cells were detached from 12-well plates, using trypsin-EDTA, and resuspended in 1 ml of complete media. The cells were subsequently distributed into poly-L-ornithine-coated (30 μg/ml) white 96-well optiplates (Perkin Elmer). The next day media was replaced with Opti-MEM (Gibco) and Coelenterazine substrate (Interchim) was added to a final concentration of 5 μM and incubated for 3 min at 25°C. BRET readings were then collected using a Multilabel Reader Mithras2 LB 943 (Berthold Technologies). Sequential integration of light output was measured for 1 sec using two filter settings (480+10nm for YFP and 540+20nm for Rluc). The BRET signal represents the ratio of the light emitted by YFP and the light emitted by Rluc (YFP/Rluc). The ratio values were corrected by subtracting background BRET signals obtained with Rluc-PTEN. MilliBRET (mBRET) values were calculated by multiplying these ratios by 1,000. Data are represented as specific mBRET values or ΔmBRET when compared to the signal obtained with WT PTEN set to 0.

MTS assays. U87 cells were transduced with lentiviruses for GFP, PTEN-WT, PTEN-C124S, PTEN-R173C or PTEN-R173H. 48 h post transduction, 5000 cells/well were plated in 96-well plates. A different plate was prepared for each day. 20 μ l of MTS assay reagent (Abcam) was added to the

cells, incubated at 37°C for 1 h, followed by measurement of absorbance at 490 nm using a plate reader.

PIP₃ biosensor analysis and PTEN localization using fluorescence microscopy. For plasma membrane PIP₃ quantification, U87-MG cells were transduced with lentiviral particles expressing the PIP₃ biosensor on its own or with lentiviral particles for PTEN-WT or PTEN-R173C, were pretreated + GDC-0941 (1 µM) for 1 h and stimulated + insulin (100 nM) for 2 min. For PTEN localization studies, MEFs were treated + GDC-0941 (1 μM) 1 h prior to fixation. For both plasma membrane PIP₃ quantification and localization of untagged or endogenous PTEN, cells were fixed with 4% PFA for 20 min, washed in PBS, permeabilized with 0.1% Triton X-100 in PBS for 90 sec, washed 3 times with PBS and blocked with PBS containing 1 or 3% (w/v) BSA for 30 min. Primary antibodies to PTEN were diluted in 1 or 3% BSA block solution and incubated for 1 h at RT. Following 3 washes with PBS, secondary antibodies and Phalloidin were diluted in 1 or 3% BSA block solution and incubated for 45 min at RT. Cells were then washed 3 times and mounted using ProLong Gold antifade reagent containing DAPI (P36935, Life Technologies). To examine GFP-PTEN localization during different stages of the cell cycle, Lenti-X™ 293T cells were transfected with DNA for PTEN-WT-GFP or PTEN-R173C-GFP. 18 and 36 h post transfection, the cells were subjected to double thymidine block as below. The same procedure was used for Pten-/R173C and PtenR173C/R173C MEFs. For double thymidine block, culture medium was changed to fresh media containing 2 mM thymidine (Sigma). 18 h post the second media change, the cells were released from double thymidine block by changing into fresh, complete media. Cells were fixed with 4% PFA for 15 min, washed in 3 times in PBS and permeabilized with 0.1% Triton X-100 in PBS for 5 min. Cells were then washed 3 times with PBS and once with water before mounting using ProLong Gold antifade reagent containing DAPI. Confocal microscopy was performed using a Zeiss LSM 880 microscope with AiryScan and a 63x PL APO objective and Zen Black acquisition software or Zeiss LSM900 microscope and a 63x or 40x PL APO objective and Zen Black acquisition software. Image processing was performed using Image J software (National Institutes of Health, Rockville, MD, United States) and was limited to alterations of brightness, subjected to the entire image. Quantification of plasma membrane PIP3 intensity was performed using Image J as described previously with minor modifications (Ooms et al., 2015). The average fluorescence intensity was measured within a box of defined size (20 x 10 pixels) at three random regions of the plasma membrane and three random regions of the cytosol (box size 20 x 20 pixels). The plasma membrane and cytosol fluorescence intensity measurement were each averaged and the ratio of plasma membrane to cytosolic fluorescence intensity determined. The PTEN nuclear to cytoplasmic ratio was measured using Image J. First, the nuclear PTEN fluorescence intensity was

measured, followed by the cytoplasmic PTEN fluorescence intensity. The ratio of nuclear to cytoplasmic PTEN fluorescence intensity was then calculated.

Insulin tolerance test (ITT). 3-month-old male *Pten*^{+/-} and *Pten*^{+/R173C} mice and their WT littermates were starved for 6 h. The tip of the tail was punctured using a 26G needle and time-0 blood glucose levels were recorded using a standard glucometer. The mice were given an IP injection of insulin to a final concentration of 0.75 U/kg. Blood glucose readings were recorded at 15 min, 30 min, 45 min, 60 min, 90 min and 120 min post injection.

Irradiation of mice: 8-12-week-old mice were subjected to whole body irradiation of 7 Gy dose using the Small Animal Radiation Therapy Platform (SARRP). 5 h post irradiation, the mice were euthanised with a lethal injection of pentobarbital. Tissues of interest were harvested and snap frozen in liquid nitrogen for biochemical analysis.

Flow cytometry. Mouse spleens and lymph nodes were mashed with a syringe plunger in RPMI containing 10% FBS and filtered through a 70 μm filter. Cell suspensions from spleen were treated with RBC lysis buffer (Biolegend). The cell suspensions were washed with PBS and stained with Fixable Viability Dye eFluor™ 780 (ThermoFisher scientific) in PBS for 40 min followed by a few PBS washes. For staining of surface antigens, antibodies were diluted in FACS staining buffer at 1:100 and added to the cells for 30 min followed by two washes with FACS buffer. Details on antibodies and reagents used is shown in **Table S11**. The stained cells were analysed on BD FACSymphony™ analyser.

Tissue processing for histological analysis and immunohistochemical analysis. Mouse tissues were fixed in 10% neutral buffered formalin for 24 h, followed by processing and embedding into paraffin blocks. The tissues were orientated with the biggest surface down, to obtain complete sections. 3 μm serial sections were cut and stained for Haematoxylin and Eosin, followed by immunohistochemistry staining on the Leica BOND Rxm. Tissue sections for immunohistochemistry were incubated for 40 min at 100°C in BOND epitope retrieval solution 2 (Leica, Germany), followed by blocking and staining using the BOND polymer refine detection kit (Leica, DS9800), primary antibody (Table S11) and DAB enhancer (Leica, Germany). All tissue slides except brain were analysed by Dr Cheryl Scudamore, a veterinary pathologist.

Histopathological analysis. Non-neoplastic lesions, e.g. splenic extramedullary haematopoiesis and lymph node hyperplasia, were graded using a standard semi-quantitative grading scheme from 0 to 5, where 0 = lesion not present and 5 = the maximum lesion size/extent (Scudamore, 2014). In general, where present, the presence of other proliferative lesions including hyperplasia and neoplasia was recorded for each individual organ, allowing the overall incidence to be established for each lesion in each group. Prostatic intraepithelial neoplasia (PIN) was graded as low or high grade according to the consensus suggested by Ittmann *et al.* (Ittmann et al., 2013). Low-grade PIN lesions are focal, with one to two layers of cells and mild nuclear atypia. High-grade lesions tend to be more extensive, filling the prostatic lumen but without stromal invasion; have two or more cell layers often forming papillary or cribriform patterns; increased nuclear atypia and mitoses.

Perfusion and preparation of brain sections for DAB immunostaining and immunofluorescence. Mice were perfused with saline (0.9 % NaCl) followed by 4% PFA (w/v) in PBS through the left ventricle of the heart. Brains were removed and post-fixed overnight at 4°C in 4% PFA, cryoprotected in 20% sucrose in PBS for 24 h at 4°C and embedded in Tissue-Tek OCT compound (Sakura) in isopentane cooled on dry ice. Frozen brains were stored at -80°C until use. Brains were processed on a Cryostat (30 µm thickness) and sections were collected in PBS for immunohistochemistry. For DAB immunostaining, floating sections were incubated with 0.3 % H₂O₂ in PBS for 30 min while shaking at RT, and then blocked using blocking buffer (10% FBS in PBS supplemented with 0.1% Triton X-100) for 1 h at RT. After blocking, sections were incubated overnight at 4°C with primary antibodies diluted in blocking buffer. Primary antibodies were detected with biotinylated secondary antibodies (Donkey Anti-Mouse IgG Biotinylated Antibody, R&D systems) diluted 1:300 in blocking buffer for 1 h at RT. The signal was amplified using the Vectastain ABC Kit HRP kit (Vector, PK-6100), according to the manufacturer's instructions and developed using a DAB Peroxidase (HRP) Substrate Kit (Vector, SK-4100) until the desired staining intensity was reached. Floating sections were mounted on Superfrost plus slides in 0.2 % pork skin gelatine dissolved in 50 mM Tris-HCl pH 7.4, dried at RT overnight and dehydrated in ethanol and xylene before mounting with DPX mounting medium (Merck). Images were acquired using 20x magnification on a ZEISS Axio Scan.Z1 microscope and processed using ZEISS ZEN lite software. For immunofluorescence, sectioned brains were blocked for 1 h before primary antibodies were applied overnight. AlexaFluor 488 secondary antibody was used to detect OLIG2 (1:1000; Invitrogen, Carlsbad, CA) for 60 min at room temperature together with Hoechst 33258 (1:1000; Sigma) to detect cell nuclei. All secondary antibodies were diluted in block solution. Floating sections were transferred onto Superfrost plus slides (BDH Laboratory Supplies) and air dried before being coverslipped with Dako fluorescent mounting medium.

Analysis of corpus callosum and cortex thickness and cell counting. Matched sections at specified Bregma levels were measured using the Zeiss Blue software measurement length tool. Counting boxes were positioned onto matched slices in the barrel field of the primary somatosensory cortex perpendicular to the corpus callosum. In each box, cells were counted from the border of the corpus callosum to the pial surface. The length of the box was adjusted to fit the cortical thickness while the width was not changed. All cells positive for NeuN within the box were counted and cell numbers displayed as crude numbers in the box as well as density considering the area of the boxes analysed. Four animals per genotype were used and quantifications were performed on 4 hemispheres from 2 consecutive sections.

Electron microscopy (EM). EM was performed as described in Ref. (Kougioumtzidou et al., 2017). Briefly, mice were prepared for EM by PBS perfusion followed by 2.5% (v/v) glutaraldehyde and 2% (w/v) paraformaldehyde in 0.1 M sodium cacodylate buffer (pH 7.6). Brains were removed and kept at 4°C for 48 h in the same fixative, before being washed with 0.1 M cacodylate buffer, rinsed briefly with 0.1 M phosphate buffer and shipped to Japan at ambient temperature. Sagitally-sectioned brains were processed for EM. After immersion in a 1% (w/v) osmium tetroxide solution for 2 h at 4°C, the specimens were dehydrated through a graded alcohol series and embedded in Epon 812 (TAAB Laboratories, UK). The required area was trimmed, and ultrathin sections were cut, collected on a platinum-coated glass slide, stained with uranyl acetate and lead citrate and imaged in a scanning electron microscope equipped with a back-scattered electron beam detector (Hitachi SU8010) at 1.5 kV accelerating voltage. EM images of sagittal sections of corpus callosum were taken at 15000x magnification. To estimate g-ratios, the circumference of the axon and the external circumference of the myelin sheath were measured using ImageJ, avoiding paranodal areas. The diameters of axon and myelin sheath were calculated from these circumferential measurements, assuming a circular profile, and the g-ratio was calculated.

Behavioural analysis. Behaviour testing was carried out as previously described (Magno et al., 2021). 12-week-old mice on mixed C57BL/6 x Sv129 background were used in this study. All mice used were group housed (maximum 5 animals per cage) with standard bedding without environmental enrichment in a room with 12 h light and 12 h dark cycle and with food and water ad libitum. Experiments took place during the 12 h light cycle between 09:00 to 17:00 in a room where external sounds were masked by white noise. All sessions were video-recorded for analysis purposes. All procedures for the care and treatment of animals were in accordance with the Animals (Scientific Procedures) Act 1986. The indicated numbers of WT mice and their *Pten*+/R173C littermates were

tested in the open field test, three chambers test, hole board and marble burying. Mice tested in behavioural experiments were habituated to handling and the experimenter for 9 days before the start of behavioural experiments to reduce stress and habituated mice were generally handled by cupping. Mice were analysed in three cohorts and male and female mice were tested on separate days. During experiments white noise was played at around 50 Db to mask external noises and all experiments were video recorded. Before every experiment, mice were brought into the behavioural room 30 min before the first experiment for habituation and animals that had finished a test were transferred into a new cage in order not to influence the behaviour of the remaining experimental animals. Directly before the first experimental animal was tested and after every mouse the set up (open field, sociability chamber, hole board) was cleaned thoroughly with water and 70% ethanol in a consistent manner for every animal. Open field: the experimental animal was placed in an open field box measuring 30 cm x 30 cm. The walls were white and 40 cm high so that the animal could not get any visual clues. The mouse was allowed to roam freely for 30 min to explore the arena without any prior habituation. Distance, time spent in different areas and the time moving were analysed using Ethovision software while faecal boli were counted manually. Sociability: The experimental animal was placed into the central compartment of Crawley's chamber for 5 min with closed doors for habituation. After 5 min empty cages were placed into the middle of the left and right compartments and a stranger mouse was gently put into one of the cages (counterbalance left and right sides). The stranger mouse matched the subject mouse with regards to the breeding background, age and gender and had no contact with the subject mouse ever before. Both doors were opened at the same time and the experimental mouse was allowed to explore the area for 10 min. A stopwatch was used to determine the time the subject mouse spent closely interacting with either cage (direct contact/sniffing/cage climbing). The time spent with the empty cage versus the first stranger was measured, referred to as sociability. Calculation of discrimination indices: (time spent with mouse – time spent with empty cage)/(sum of the time spent with both). Hole board: since the experimental animals were familiar with the open field arena from the open field experiment, they were only briefly re-exposed to the empty arena for 10 min on day 1 of the hole board test. On the next day a hole board with 16 holes evenly spaced was placed into the arena, the subject mouse was put into the middle of the field and was recorded for 15 min. A manual cell counter was used to determine the total number of head dips into the holes. Marble burying: a cage was filled with 5cm of bedding that was tamped down lightly to produce an even surface. 12 glass marbles were distributed evenly spaced out in the cage and the animal was allowed to roam freely for 15 min. Marbles that were buried to 2/3 of their depth with bedding were visually counted.

Statistical analysis: GraphPad Prism (San Diego, CA, United States) was used for statistical analysis. The method used for individual datasets is indicated in the figure legends. Details such as post hoc tests and p values are listed in **Table S13**.

Patient data: Patient data in Tables 1, S1 and S2 were collected from the PHTS Patient Registry UK which has patient consent for data release. Dr Katherine Lachlan and Dr Isra Ahmed Mohamed provided data with patient consent. The remaining data is from published sources.

ACKNOWLEDGEMENTS

Personal funding was from the Jean Shanks Pathological Society (Clinical PhD fellowship; to V.R.), CRUK UCL Centre Non-Clinical Training Awards (C416/A29287 to G.C. and CANTAC721\100022 to F.B.) and the European Commission (H2020-MSCA-IF-2018 GA: 838559; to S.C.). Research in the B.V. laboratory was supported by PTEN Research (UCL-16-001, UCL-20-001), Cancer Research UK (C23338/A25722) and the UK Biotechnology and Biological Sciences Research Council (BB/W007460/1). Research in N.R.L. laboratory was supported by PTEN Research. Research in the M.G.H.S. group was supported by Fondation ARC pour la recherche sur le cancer (ARCPJA2022060005118) and Ligue Contre le Cancer (Comité de Paris). The UCL Cancer Institute Translational Technology Platforms are supported by the CRUK UCL Centre Award (C416/A25145). The N.K. lab is funded by grants from the UK Biotechnology and Biological Sciences Research Council (BB/N009061/1) and the Wellcome Trust (108726/Z/15/Z). M.T. and K.S. are supported by PTEN Research and the NIHR Cambridge Biomedical Research Centre (NIHR203312). The PHTS Patient Registry UK is funded by PTEN Research (UOC-17-001). G.R.M. and R.L.W. were supported by MRC funding (MC-A024-5PF91 to R.L.W.). We thank staff at the Technical Support Centre for Life Science Research in IMU for excellent technical support with EM processing. We also thank the UCL Research Capital Infrastructure Fund (RCIF) and the National Institute for Health Research University College London Hospitals Biomedical Research Centre for upgrade of the UCL Cancer Institute Microscopy facility and Dr Maria Whitehead and Dr Paul Elvin and members from the B.V. group for excellent feedback on the manuscript.

Author contributions

PT, NRL, NK and BV conceived the study, PT, VR, SEC, GAEC, FB, MAD, GC, ZA,KT, NK, VAG, EF, DB, ML,WP, MA, ZV, SH, LC, AA, GRM and MGHS performed and analysed the experiments, CLS

performed the histological analysis, RLW, AMF and JH provided reagents/resources for the study, PT, NK and BV wrote the manuscript.

Competing interest statement

BV is a consultant for iOnctura (Geneva, Switzerland) and a shareholder of Open Orphan (Dublin, Ireland).

REFERENCES

- ALIMONTI, A., CARRACEDO, A., CLOHESSY, J. G., TROTMAN, L. C., NARDELLA, C., EGIA, A., SALMENA, L., SAMPIERI, K., HAVEMAN, W. J., BROGI, E., RICHARDSON, A. L., ZHANG, J. & PANDOLFI, P. P. 2010. Subtle variations in Pten dose determine cancer susceptibility. *Nat Genet*, 42, 454-8.
- ALVAREZ-GARCIA, V., TAWIL, Y., WISE, H. M. & LESLIE, N. R. 2019. Mechanisms of PTEN loss in cancer: It's all about diversity. *Semin Cancer Biol*, 59, 66-79.
- ATTIA, S. M., AL-HAMAMAH, M. A., AHMAD, S. F., NADEEM, A., ATTIA, M. S. M., ANSARI, M. A., BAKHEET, S. A. & AL-AYADHI, L. Y. 2020. Evaluation of DNA repair efficiency in autistic children by molecular cytogenetic analysis and transcriptome profiling. *DNA Repair (Amst)*, 85, 102750.
- BASSI, C., HO, J., SRIKUMAR, T., DOWLING, R. J., GORRINI, C., MILLER, S. J., MAK, T. W., NEEL, B. G., RAUGHT, B. & STAMBOLIC, V. 2013. Nuclear PTEN controls DNA repair and sensitivity to genotoxic stress. *Science*, 341, 395-9.
- BATEUP, H. S., JOHNSON, C. A., DENEFRIO, C. L., SAULNIER, J. L., KORNACKER, K. & SABATINI, B. L. 2013. Excitatory/inhibitory synaptic imbalance leads to hippocampal hyperexcitability in mouse models of tuberous sclerosis. *Neuron*, 78, 510-22.
- BIRLE, D., BOTTINI, N., WILLIAMS, S., HUYNH, H., DEBELLE, I., ADAMSON, E. & MUSTELIN, T. 2002.

 Negative feedback regulation of the tumor suppressor PTEN by phosphoinositide-induced serine phosphorylation. *J Immunol*, 169, 286-91.
- CASERTA, E., EGRIBOZ, O., WANG, H., MARTIN, C., KOIVISTO, C., PECOT, T., KLADNEY, R. D., SHEN, C., SHIM, K. S., PHAM, T., KARIKOMI, M. K., MAUNTEL, M. J., MAJUMDER, S., CUITINO, M. C., TANG, X., SRIVASTAVA, A., YU, L., WALLACE, J., MO, X., PARK, M., FERNANDEZ, S. A., PILARSKI, R., LA PERLE, K. M., ROSOL, T. J., COPPOLA, V., CASTRILLON, D. H., TIMMERS, C., COHN, D. E., O'MALLEY, D. M., BACKES, F., SUAREZ, A. A., GOODFELLOW, P., CHAMBERLIN, H. M., MACRAE, E. R., SHAPIRO, C. L., OSTROWSKI, M. C. & LEONE, G. 2015. Noncatalytic PTEN

- missense mutation predisposes to organ-selective cancer development in vivo. *Genes Dev,* 29, 1707-20.
- CHEN, C. Y., CHEN, J., HE, L. & STILES, B. L. 2018. PTEN: Tumor Suppressor and Metabolic Regulator. Front Endocrinol (Lausanne), 9, 338.
- CHEN, H. H., HANDEL, N., NGEOW, J., MULLER, J., HUHN, M., YANG, H. T., HEINDL, M., BERBERS, R. M., HEGAZY, A. N., KIONKE, J., YEHIA, L., SACK, U., BLASER, F., RENSING-EHL, A., REIFENBERGER, J., KEITH, J., TRAVIS, S., MERKENSCHLAGER, A., KIESS, W., WITTEKIND, C., WALKER, L., EHL, S., ARETZ, S., DUSTIN, M. L., ENG, C., POWRIE, F. & UHLIG, H. H. 2017. Immune dysregulation in patients with PTEN hamartoma tumor syndrome: Analysis of FOXP3 regulatory T cells. *J Allergy Clin Immunol*, 139, 607-620 e15.
- CLIPPERTON-ALLEN, A. E. & PAGE, D. T. 2014. Pten haploinsufficient mice show broad brain overgrowth but selective impairments in autism-relevant behavioral tests. *Hum Mol Genet,* 23, 3490-505.
- DAVIDSON, L., MACCARIO, H., PERERA, N. M., YANG, X., SPINELLI, L., TIBAREWAL, P., GLANCY, B., GRAY, A., WEIJER, C. J., DOWNES, C. P. & LESLIE, N. R. 2010. Suppression of cellular proliferation and invasion by the concerted lipid and protein phosphatase activities of PTEN. *Oncogene*, 29, 687-97.
- DEMPSEY, D. R., VIENNET, T., IWASE, R., PARK, E., HENRIQUEZ, S., CHEN, Z., JELIAZKOV, J. R., PALANSKI, B. A., PHAN, K. L., COOTE, P., GRAY, J. J., ECK, M. J., GABELLI, S. B., ARTHANARI, H. & COLE, P. A. 2021. The structural basis of PTEN regulation by multi-site phosphorylation. *Nat Struct Mol Biol*, 28, 858-868.
- DI CRISTOFANO, A., DE ACETIS, M., KOFF, A., CORDON-CARDO, C. & PANDOLFI, P. P. 2001. Pten and p27KIP1 cooperate in prostate cancer tumor suppression in the mouse. *Nat Genet,* 27, 222-4.
- DI CRISTOFANO, A., PESCE, B., CORDON-CARDO, C. & PANDOLFI, P. P. 1998. Pten is essential for embryonic development and tumour suppression. *Nat Genet,* 19, 348-55.
- DICKINS, R. A., HEMANN, M. T., ZILFOU, J. T., SIMPSON, D. R., IBARRA, I., HANNON, G. J. & LOWE, S. W. 2005. Probing tumor phenotypes using stable and regulated synthetic microRNA precursors. *Nat Genet*, 37, 1289-95.
- DRISSEN, M., VOS, J. R., COLLADO CAMPS, E., SCHUURS-HOEIJMAKERS, J. H. M., SCHIEVING, J. H. & HOOGERBRUGGE, N. 2024. Increased frequency of infections and autoimmune disease in adults with PTEN Hamartoma Tumour Syndrome. *Eur J Med Genet*, 70, 104960.
- DROST, R. M. & JONKERS, J. 2009. Preclinical mouse models for BRCA1-associated breast cancer. *Br J Cancer*, 101, 1651-7.

- FREEMAN, D., LESCHE, R., KERTESZ, N., WANG, S., LI, G., GAO, J., GROSZER, M., MARTINEZ-DIAZ, H., ROZENGURT, N., THOMAS, G., LIU, X. & WU, H. 2006. Genetic background controls tumor development in PTEN-deficient mice. *Cancer Res*, 66, 6492-6.
- FRICANO-KUGLER, C. J., GETZ, S. A., WILLIAMS, M. R., ZURAWEL, A. A., DESPENZA, T., JR., FRAZEL, P. W., LI, M., O'MALLEY, A. J., MOEN, E. L. & LUIKART, B. W. 2018. Nuclear Excluded Autism-Associated Phosphatase and Tensin Homolog Mutations Dysregulate Neuronal Growth. *Biol Psychiatry*, 84, 265-277.
- GARCIA-CAO, I., SONG, M. S., HOBBS, R. M., LAURENT, G., GIORGI, C., DE BOER, V. C., ANASTASIOU, D., ITO, K., SASAKI, A. T., RAMEH, L., CARRACEDO, A., VANDER HEIDEN, M. G., CANTLEY, L. C., PINTON, P., HAIGIS, M. C. & PANDOLFI, P. P. 2012. Systemic elevation of PTEN induces a tumor-suppressive metabolic state. *Cell*, 149, 49-62.
- GUPTA, A. & LESLIE, N. R. 2016. Controlling PTEN (Phosphatase and Tensin Homolog) Stability: A DOMINANT ROLE FOR LYSINE 66. *J Biol Chem*, 291, 18465-73.
- HAKEM, R., DE LA POMPA, J. L., SIRARD, C., MO, R., WOO, M., HAKEM, A., WAKEHAM, A., POTTER, J., REITMAIR, A., BILLIA, F., FIRPO, E., HUI, C. C., ROBERTS, J., ROSSANT, J. & MAK, T. W. 1996.

 The tumor suppressor gene Brca1 is required for embryonic cellular proliferation in the mouse. *Cell*, 85, 1009-23.
- HAN, S. Y., KATO, H., KATO, S., SUZUKI, T., SHIBATA, H., ISHII, S., SHIIBA, K., MATSUNO, S., KANAMARU, R. & ISHIOKA, C. 2000. Functional evaluation of PTEN missense mutations using in vitro phosphoinositide phosphatase assay. *Cancer Res*, 60, 3147-51.
- HENDRICKS, L. A. J., HOOGERBRUGGE, N., VENSELAAR, H., ARETZ, S., SPIER, I., LEGIUS, E., BREMS, H., DE PUTTER, R., CLAES, K. B. M., EVANS, D. G., WOODWARD, E. R., GENUARDI, M., BRUGNOLETTI, F., VAN IERLAND, Y., DIJKE, K., THAM, E., TESI, B., SCHUURS-HOEIJMAKERS, J. H. M., BRANCHAUD, M., SALVADOR, H., JAHN, A., SCHNAITER, S., ANASTASIADOU, V. C., BRUNET, J., OLIVEIRA, C., ROHT, L., BLATNIK, A., IRMEJS, A., GROUP, P. S., MENSENKAMP, A. R. & VOS, J. R. 2022. Genotype-phenotype associations in a large PTEN Hamartoma Tumor Syndrome (PHTS) patient cohort. *Eur J Med Genet*, 65, 104632.
- HO, J., CRUISE, E. S., DOWLING, R. J. O. & STAMBOLIC, V. 2019. PTEN Nuclear Functions. *Cold Spring Harb Perspect Med*.
- IGARASHI, A., ITOH, K., YAMADA, T., ADACHI, Y., KATO, T., MURATA, D., SESAKI, H. & IIJIMA, M. 2018.

 Nuclear PTEN deficiency causes microcephaly with decreased neuronal soma size and increased seizure susceptibility. *J Biol Chem*, 293, 9292-9300.

- ITTMANN, M., HUANG, J., RADAELLI, E., MARTIN, P., SIGNORETTI, S., SULLIVAN, R., SIMONS, B. W., WARD, J. M., ROBINSON, B. D., CHU, G. C., LODA, M., THOMAS, G., BOROWSKY, A. & CARDIFF, R. D. 2013. Animal models of human prostate cancer: the consensus report of the New York meeting of the Mouse Models of Human Cancers Consortium Prostate Pathology Committee. *Cancer Res*, 73, 2718-36.
- JAINI, R., LOYA, M. G., KING, A. T., THACKER, S., SARN, N. B., YU, Q., STARK, G. R. & ENG, C. 2020. Germline PTEN mutations are associated with a skewed peripheral immune repertoire in humans and mice. *Hum Mol Genet*, 29, 2353-2364.
- JUN, H. J., PAULO, J. A., APPLEMAN, V. A., YARON-BARIR, T. M., JOHNSON, J. L., YEO, A. T., ROGERS, V. A., KUANG, S., VARMA, H., GYGI, S. P., TROTMAN, L. C. & CHAREST, A. 2024. Pleiotropic tumor suppressive functions of PTEN missense mutations during gliomagenesis. *iScience*, 27, 111278.
- KATO, T., IGARASHI, A., SESAKI, H. & IIJIMA, M. 2021. Generating a new mouse model for nuclear PTEN deficiency by a single K13R mutation. *Genes Cells*, 26, 1014-1022.
- KATO, T., YAMADA, T., NAKAMURA, H., IGARASHI, A., ANDERS, R. A., SESAKI, H. & IIJIMA, M. 2020.

 The Loss of Nuclear PTEN Increases Tumorigenesis in a Preclinical Mouse Model for Hepatocellular Carcinoma. *iScience*, 23, 101548.
- KESSARIS, N., FOGARTY, M., IANNARELLI, P., GRIST, M., WEGNER, M. & RICHARDSON, W. D. 2006.

 Competing waves of oligodendrocytes in the forebrain and postnatal elimination of an embryonic lineage. *Nat Neurosci*, 9, 173-9.
- KNOBBE, C. B., LAPIN, V., SUZUKI, A. & MAK, T. W. 2008. The roles of PTEN in development, physiology and tumorigenesis in mouse models: a tissue-by-tissue survey. *Oncogene*, 27, 5398-415.
- KOUGIOUMTZIDOU, E., SHIMIZU, T., HAMILTON, N. B., TOHYAMA, K., SPRENGEL, R., MONYER, H., ATTWELL, D. & RICHARDSON, W. D. 2017. Signalling through AMPA receptors on oligodendrocyte precursors promotes myelination by enhancing oligodendrocyte survival. *Elife*, 6.
- KWON, C. H., LUIKART, B. W., POWELL, C. M., ZHOU, J., MATHENY, S. A., ZHANG, W., LI, Y., BAKER, S. J. & PARADA, L. F. 2006. Pten regulates neuronal arborization and social interaction in mice. *Neuron*, 50, 377-88.
- LACHLAN, K. L., LUCASSEN, A. M., BUNYAN, D. & TEMPLE, I. K. 2007. Cowden syndrome and Bannayan Riley Ruvalcaba syndrome represent one condition with variable expression and age-related penetrance: results of a clinical study of PTEN mutation carriers. *J Med Genet*, 44, 579-85.

- LANGDON, C. G. 2023. Nuclear PTEN's Functions in Suppressing Tumorigenesis: Implications for Rare Cancers. *Biomolecules*, 13.
- LEE, J. O., YANG, H., GEORGESCU, M. M., DI CRISTOFANO, A., MAEHAMA, T., SHI, Y., DIXON, J. E., PANDOLFI, P. & PAVLETICH, N. P. 1999. Crystal structure of the PTEN tumor suppressor: implications for its phosphoinositide phosphatase activity and membrane association. *Cell*, 99, 323-34.
- LEE, Y. R. & PANDOLFI, P. P. 2020. PTEN Mouse Models of Cancer Initiation and Progression. *Cold Spring Harb Perspect Med,* 10.
- LESCHE, R., GROSZER, M., GAO, J., WANG, Y., MESSING, A., SUN, H., LIU, X. & WU, H. 2002. Cre/loxP-mediated inactivation of the murine Pten tumor suppressor gene. *Genesis*, 32, 148-9.
- LESLIE, N. R. & LONGY, M. 2016. Inherited PTEN mutations and the prediction of phenotype. *Semin Cell Dev Biol*, 52, 30-8.
- LESLIE, N. R., MACCARIO, H., SPINELLI, L. & DAVIDSON, L. 2009. The significance of PTEN's protein phosphatase activity. *Adv Enzyme Regul*, 49, 190-6.
- LI, J., YEN, C., LIAW, D., PODSYPANINA, K., BOSE, S., WANG, S. I., PUC, J., MILIARESIS, C., RODGERS, L., MCCOMBIE, R., BIGNER, S. H., GIOVANELLA, B. C., ITTMANN, M., TYCKO, B., HIBSHOOSH, H., WIGLER, M. H. & PARSONS, R. 1997. PTEN, a putative protein tyrosine phosphatase gene mutated in human brain, breast, and prostate cancer. *Science*, 275, 1943-7.
- LIMA-FERNANDES, E., MISTICONE, S., BOULARAN, C., PARADIS, J. S., ENSLEN, H., ROUX, P. P., BOUVIER, M., BAILLIE, G. S., MARULLO, S. & SCOTT, M. G. 2014. A biosensor to monitor dynamic regulation and function of tumour suppressor PTEN in living cells. *Nat Commun*, 5, 4431.
- MA, J., BENITEZ, J. A., LI, J., MIKI, S., PONTE DE ALBUQUERQUE, C., GALATRO, T., ORELLANA, L., ZANCA, C., REED, R., BOYER, A., KOGA, T., VARKI, N. M., FENTON, T. R., NAGAHASHI MARIE, S. K., LINDAHL, E., GAHMAN, T. C., SHIAU, A. K., ZHOU, H., DEGROOT, J., SULMAN, E. P., CAVENEE, W. K., KOLODNER, R. D., CHEN, C. C. & FURNARI, F. B. 2019. Inhibition of Nuclear PTEN Tyrosine Phosphorylation Enhances Glioma Radiation Sensitivity through Attenuated DNA Repair. *Cancer Cell*, 35, 504-518 e7.
- MACCARIO, H., PERERA, N. M., GRAY, A., DOWNES, C. P. & LESLIE, N. R. 2010. Ubiquitination of PTEN (phosphatase and tensin homolog) inhibits phosphatase activity and is enhanced by membrane targeting and hyperosmotic stress. *J Biol Chem,* 285, 12620-8.
- MAEHAMA, T. & DIXON, J. E. 1998. The tumor suppressor, PTEN/MMAC1, dephosphorylates the lipid second messenger, phosphatidylinositol 3,4,5-trisphosphate. *J Biol Chem*, 273, 13375-8.

- MAGNO, L., ASGARIAN, Z., PENDOLINO, V., VELONA, T., MACKINTOSH, A., LEE, F., STRYJEWSKA, A., ZIMMER, C., GUILLEMOT, F., FARRANT, M., CLARK, B. & KESSARIS, N. 2021. Transient developmental imbalance of cortical interneuron subtypes presages long-term changes in behavior. *Cell Rep.*, 35, 109249.
- MARSH, D. J., COULON, V., LUNETTA, K. L., ROCCA-SERRA, P., DAHIA, P. L., ZHENG, Z., LIAW, D., CARON, S., DUBOUE, B., LIN, A. Y., RICHARDSON, A. L., BONNETBLANC, J. M., BRESSIEUX, J. M., CABARROT-MOREAU, A., CHOMPRET, A., DEMANGE, L., EELES, R. A., YAHANDA, A. M., FEARON, E. R., FRICKER, J. P., GORLIN, R. J., HODGSON, S. V., HUSON, S., LACOMBE, D., ENG, C. & ET Al. 1998. Mutation spectrum and genotype-phenotype analyses in Cowden disease and Bannayan-Zonana syndrome, two hamartoma syndromes with germline PTEN mutation. *Hum Mol Genet*, 7, 507-15.
- MARSH, D. J., KUM, J. B., LUNETTA, K. L., BENNETT, M. J., GORLIN, R. J., AHMED, S. F., BODURTHA, J., CROWE, C., CURTIS, M. A., DASOUKI, M., DUNN, T., FEIT, H., GERAGHTY, M. T., GRAHAM, J. M., JR., HODGSON, S. V., HUNTER, A., KORF, B. R., MANCHESTER, D., MIESFELDT, S., MURDAY, V. A., NATHANSON, K. L., PARISI, M., POBER, B., ROMANO, C., ENG, C. & ET AL. 1999. PTEN mutation spectrum and genotype-phenotype correlations in Bannayan-Riley-Ruvalcaba syndrome suggest a single entity with Cowden syndrome. *Hum Mol Genet*, 8, 1461-72.
- MASSON, G. R., BURKE, J. E. & WILLIAMS, R. L. 2016a. Methods in the Study of PTEN Structure: X-Ray Crystallography and Hydrogen Deuterium Exchange Mass Spectrometry. *Methods Mol Biol*, 1388, 215-30.
- MASSON, G. R., PERISIC, O., BURKE, J. E. & WILLIAMS, R. L. 2016b. The intrinsically disordered tails of PTEN and PTEN-L have distinct roles in regulating substrate specificity and membrane activity. *Biochem J*, 473, 135-44.
- MATOS-RODRIGUES, G., MARTINI, E. & LOPEZ, B. S. 2021. Mouse Models for Deciphering the Impact of Homologous Recombination on Tumorigenesis. *Cancers (Basel)*, 13.
- MENDES-PEREIRA, A. M., MARTIN, S. A., BROUGH, R., MCCARTHY, A., TAYLOR, J. R., KIM, J. S., WALDMAN, T., LORD, C. J. & ASHWORTH, A. 2009. Synthetic lethal targeting of PTEN mutant cells with PARP inhibitors. *EMBO Mol Med*, 1, 315-22.
- MESTER, J. L., TILOT, A. K., RYBICKI, L. A., FRAZIER, T. W., 2ND & ENG, C. 2011. Analysis of prevalence and degree of macrocephaly in patients with germline PTEN mutations and of brain weight in Pten knock-in murine model. *Eur J Hum Genet*, 19, 763-8.

- MIGHELL, T. L., EVANS-DUTSON, S. & O'ROAK, B. J. 2018. A Saturation Mutagenesis Approach to Understanding PTEN Lipid Phosphatase Activity and Genotype-Phenotype Relationships. *Am J Hum Genet*, 102, 943-955.
- MISTICONE, S., LIMA-FERNANDES, E. & SCOTT, M. G. 2016. Rapid Detection of Dynamic PTEN Regulation in Living Cells Using Intramolecular BRET. *Methods Mol Biol*, 1388, 95-110.
- MYERS, M. P., PASS, I., BATTY, I. H., VAN DER KAAY, J., STOLAROV, J. P., HEMMINGS, B. A., WIGLER, M. H., DOWNES, C. P. & TONKS, N. K. 1998. The lipid phosphatase activity of PTEN is critical for its tumor supressor function. *Proc Natl Acad Sci U S A*, 95, 13513-8.
- NELEN, M. R., PADBERG, G. W., PEETERS, E. A., LIN, A. Y., VAN DEN HELM, B., FRANTS, R. R., COULON, V., GOLDSTEIN, A. M., VAN REEN, M. M., EASTON, D. F., EELES, R. A., HODGSEN, S., MULVIHILL, J. J., MURDAY, V. A., TUCKER, M. A., MARIMAN, E. C., STARINK, T. M., PONDER, B. A., ROPERS, H. H., KREMER, H., LONGY, M. & ENG, C. 1996. Localization of the gene for Cowden disease to chromosome 10q22-23. *Nat Genet*, 13, 114-6.
- NGEOW, J. & ENG, C. 2019. PTEN in Hereditary and Sporadic Cancer. Cold Spring Harb Perspect Med.
- ODRIOZOLA, L., SINGH, G., HOANG, T. & CHAN, A. M. 2007. Regulation of PTEN activity by its carboxyl-terminal autoinhibitory domain. *J Biol Chem*, 282, 23306-15.
- OOMS, L. M., BINGE, L. C., DAVIES, E. M., RAHMAN, P., CONWAY, J. R., GURUNG, R., FERGUSON, D. T., PAPA, A., FEDELE, C. G., VIEUSSEUX, J. L., CHAI, R. C., KOENTGEN, F., PRICE, J. T., TIGANIS, T., TIMPSON, P., MCLEAN, C. A. & MITCHELL, C. A. 2015. The Inositol Polyphosphate 5-Phosphatase PIPP Regulates AKT1-Dependent Breast Cancer Growth and Metastasis. *Cancer Cell*, 28, 155-69.
- PAL, A., BARBER, T. M., VAN DE BUNT, M., RUDGE, S. A., ZHANG, Q., LACHLAN, K. L., COOPER, N. S., LINDEN, H., LEVY, J. C., WAKELAM, M. J., WALKER, L., KARPE, F. & GLOYN, A. L. 2012. PTEN mutations as a cause of constitutive insulin sensitivity and obesity. *N Engl J Med*, 367, 1002-11.
- PODSYPANINA, K., ELLENSON, L. H., NEMES, A., GU, J., TAMURA, M., YAMADA, K. M., CORDON-CARDO, C., CATORETTI, G., FISHER, P. E. & PARSONS, R. 1999. Mutation of Pten/Mmac1 in mice causes neoplasia in multiple organ systems. *Proc Natl Acad Sci U S A*, 96, 1563-8.
- POST, K. L., BELMADANI, M., GANGULY, P., MEILI, F., DINGWALL, R., MCDIARMID, T. A., MEYERS, W. M., HERRINGTON, C., YOUNG, B. P., CALLAGHAN, D. B., ROGIC, S., EDWARDS, M., NICIFOROVIC, A., CAU, A., RANKIN, C. H., O'CONNOR, T. P., BAMJI, S. X., LOEWEN, C. J. R., ALLAN, D. W., PAVLIDIS, P. & HAAS, K. 2020. Multi-model functionalization of disease-associated PTEN missense mutations identifies multiple molecular mechanisms underlying protein dysfunction. *Nat Commun*, 11, 2073.

- RANTAKARI, P., NIKKILA, J., JOKELA, H., OLA, R., PYLKAS, K., LAGERBOHM, H., SAINIO, K., POUTANEN, M. & WINQVIST, R. 2010. Inactivation of Palb2 gene leads to mesoderm differentiation defect and early embryonic lethality in mice. *Hum Mol Genet*, 19, 3021-9.
- ROY, R., CHUN, J. & POWELL, S. N. 2011. BRCA1 and BRCA2: different roles in a common pathway of genome protection. *Nat Rev Cancer*, 12, 68-78.
- SCHEI-ANDERSEN, A. J., WITJES, V. M., VOS, J. R., MENSENKAMP, A. R., VAN ALTENA, A., SCHIEVING, J., SIMONS, M., SCHUURS-HOEIJMAKERS, J. H. M., GROUP, P. S. & HOOGERBRUGGE, N. 2025.

 Non-serous ovarian cancer in PTEN Hamartoma Tumor Syndrome: additional evidence for increased risk. *Fam Cancer*, 24, 28.
- SCHONHUBER, N., SEIDLER, B., SCHUCK, K., VELTKAMP, C., SCHACHTLER, C., ZUKOWSKA, M., ESER, S., FEYERABEND, T. B., PAUL, M. C., ESER, P., KLEIN, S., LOWY, A. M., BANERJEE, R., YANG, F., LEE, C. L., MODING, E. J., KIRSCH, D. G., SCHEIDELER, A., ALESSI, D. R., VARELA, I., BRADLEY, A., KIND, A., SCHNIEKE, A. E., RODEWALD, H. R., RAD, R., SCHMID, R. M., SCHNEIDER, G. & SAUR, D. 2014. A next-generation dual-recombinase system for time- and host-specific targeting of pancreatic cancer. *Nat Med*, 20, 1340-1347.
- SCUDAMORE, C. 2014. Practical approaches to reviewing and recording pathology data. *In:* C.L., S. (ed.) *A Practical Guide to Histology of the Mouse* Chichester, UK: Wiley-Blackwell.
- SHEN, W. H., BALAJEE, A. S., WANG, J., WU, H., ENG, C., PANDOLFI, P. P. & YIN, Y. 2007. Essential role for nuclear PTEN in maintaining chromosomal integrity. *Cell*, 128, 157-70.
- SMITH, I. N. & BRIGGS, J. M. 2016. Structural mutation analysis of PTEN and its genotype-phenotype correlations in endometriosis and cancer. *Proteins*, 84, 1625-1643.
- SPINELLI, L., BLACK, F. M., BERG, J. N., EICKHOLT, B. J. & LESLIE, N. R. 2015. Functionally distinct groups of inherited PTEN mutations in autism and tumour syndromes. *J Med Genet*, 52, 128-34.
- STECK, P. A., PERSHOUSE, M. A., JASSER, S. A., YUNG, W. K., LIN, H., LIGON, A. H., LANGFORD, L. A., BAUMGARD, M. L., HATTIER, T., DAVIS, T., FRYE, C., HU, R., SWEDLUND, B., TENG, D. H. & TAVTIGIAN, S. V. 1997. Identification of a candidate tumour suppressor gene, MMAC1, at chromosome 10q23.3 that is mutated in multiple advanced cancers. *Nat Genet*, 15, 356-62.
- SUZUKI, A., DE LA POMPA, J. L., STAMBOLIC, V., ELIA, A. J., SASAKI, T., DEL BARCO BARRANTES, I., HO, A., WAKEHAM, A., ITIE, A., KHOO, W., FUKUMOTO, M. & MAK, T. W. 1998. High cancer susceptibility and embryonic lethality associated with mutation of the PTEN tumor suppressor gene in mice. *Curr Biol*, 8, 1169-78.

- TIBAREWAL, P., RATHBONE, V., CONSTANTINOU, G., PEARCE, W., ADIL, M., VARYOVA, Z., FOLKES, L., HAMPSON, A., CLASSEN, G. A. E., ALVES, A., CARVALHO, S., SCUDAMORE, C. L. & VANHAESEBROECK, B. 2022. Long-term treatment of cancer-prone germline PTEN mutant mice with low-dose rapamycin extends lifespan and delays tumour development. *J Pathol*, 258, 382-394.
- TIBAREWAL, P., ZILIDIS, G., SPINELLI, L., SCHURCH, N., MACCARIO, H., GRAY, A., PERERA, N. M., DAVIDSON, L., BARTON, G. J. & LESLIE, N. R. 2012. PTEN protein phosphatase activity correlates with control of gene expression and invasion, a tumor-suppressing phenotype, but not with AKT activity. *Sci Signal*, 5, ra18.
- TILOT, A. K., GAUGLER, M. K., YU, Q., ROMIGH, T., YU, W., MILLER, R. H., FRAZIER, T. W., 2ND & ENG, C. 2014. Germline disruption of Pten localization causes enhanced sex-dependent social motivation and increased glial production. *Hum Mol Genet*, 23, 3212-27.
- TORRES, J. & PULIDO, R. 2001. The tumor suppressor PTEN is phosphorylated by the protein kinase CK2 at its C terminus. Implications for PTEN stability to proteasome-mediated degradation. *J Biol Chem*, 276, 993-8.
- TSUZUKI, T., FUJII, Y., SAKUMI, K., TOMINAGA, Y., NAKAO, K., SEKIGUCHI, M., MATSUSHIRO, A., YOSHIMURA, Y. & MORITAT 1996. Targeted disruption of the Rad51 gene leads to lethality in embryonic mice. *Proc Natl Acad Sci U S A*, 93, 6236-40.
- VAZQUEZ, F., GROSSMAN, S. R., TAKAHASHI, Y., ROKAS, M. V., NAKAMURA, N. & SELLERS, W. R. 2001. Phosphorylation of the PTEN tail acts as an inhibitory switch by preventing its recruitment into a protein complex. *J Biol Chem*, 276, 48627-30.
- WANG, M., WEI, P. C., LIM, C. K., GALLINA, I. S., MARSHALL, S., MARCHETTO, M. C., ALT, F. W. & GAGE, F. H. 2020. Increased Neural Progenitor Proliferation in a hiPSC Model of Autism Induces Replication Stress-Associated Genome Instability. *Cell Stem Cell*, 26, 221-233 e6.
- WEI, R., HITOMI, M., SADLER, T., YEHIA, L., CALVETTI, D., SCOTT, J. & ENG, C. 2024. Quantitative evaluation of DNA damage repair dynamics to elucidate predictors of autism vs. cancer in individuals with germline PTEN variants. *PLoS Comput Biol*, 20, e1012449.
- WHITE, S. L., JAMIL, T., BELL, C., FISHBEIN, L., HAUGEN, B. R., GIGNOUX, C. R. & POZDEYEV, N. 2025.

 Population Prevalence of the Major Thyroid Cancer–Associated Syndromes. *The Journal of Clinical Endocrinology & Metabolism*.
- YAN, D. H., WEN, Y., SU, L. K., XIA, W., WANG, S. C., ZHANG, S., GAN, L., LEE, D. F., SPOHN, B., FREY, J. A., HORTOBAGYI, G. N. & HUNG, M. C. 2004. A delayed chemically induced tumorigenesis in Brca2 mutant mice. *Oncogene*, 23, 1896-901.

- YEHIA, L. & ENG, C. 2018. 65 YEARS OF THE DOUBLE HELIX: One gene, many endocrine and metabolic syndromes: PTEN-opathies and precision medicine. *Endocr Relat Cancer*, 25, T121-T140.
- YEHIA, L., KEEL, E. & ENG, C. 2020. The Clinical Spectrum of PTEN Mutations. *Annu Rev Med*, 71, 103-116.
- YEHIA, L., NGEOW, J. & ENG, C. 2019. PTEN-opathies: from biological insights to evidence-based precision medicine. *J Clin Invest*, 129, 452-464.
- YEHIA, L., PLITT, G., TUSHAR, A. M., LIU, D., JOO, J., NI, Y., PATIL, S. & ENG, C. 2025. Extended spectrum of cancers in PTEN hamartoma tumor syndrome. *NPJ Precis Oncol*, 9, 61.
- YIP, H. Y. K., CHEE, A., ANG, C. S., SHIN, S. Y., OOMS, L. M., MOHAMMADI, Z., PHILLIPS, W. A., DALY, R. J., COLE, T. J., BRONSON, R. T., NGUYEN, L. K., TIGANIS, T., HOBBS, R. M., MCLEAN, C. A., MITCHELL, C. A. & PAPA, A. 2020. Control of Glucocorticoid Receptor Levels by PTEN Establishes a Failsafe Mechanism for Tumor Suppression. *Mol Cell*, 80, 279-295 e8.
- YUAN, E., TSAI, P. T., GREENE-COLOZZI, E., SAHIN, M., KWIATKOWSKI, D. J. & MALINOWSKA, I. A. 2012. Graded loss of tuberin in an allelic series of brain models of TSC correlates with survival, and biochemical, histological and behavioral features. *Hum Mol Genet*, 21, 4286-300.
- ZHOU, J., BLUNDELL, J., OGAWA, S., KWON, C. H., ZHANG, W., SINTON, C., POWELL, C. M. & PARADA, L. F. 2009. Pharmacological inhibition of mTORC1 suppresses anatomical, cellular, and behavioral abnormalities in neural-specific Pten knock-out mice. *J Neurosci*, 29, 1773-83.

Figures and Tables

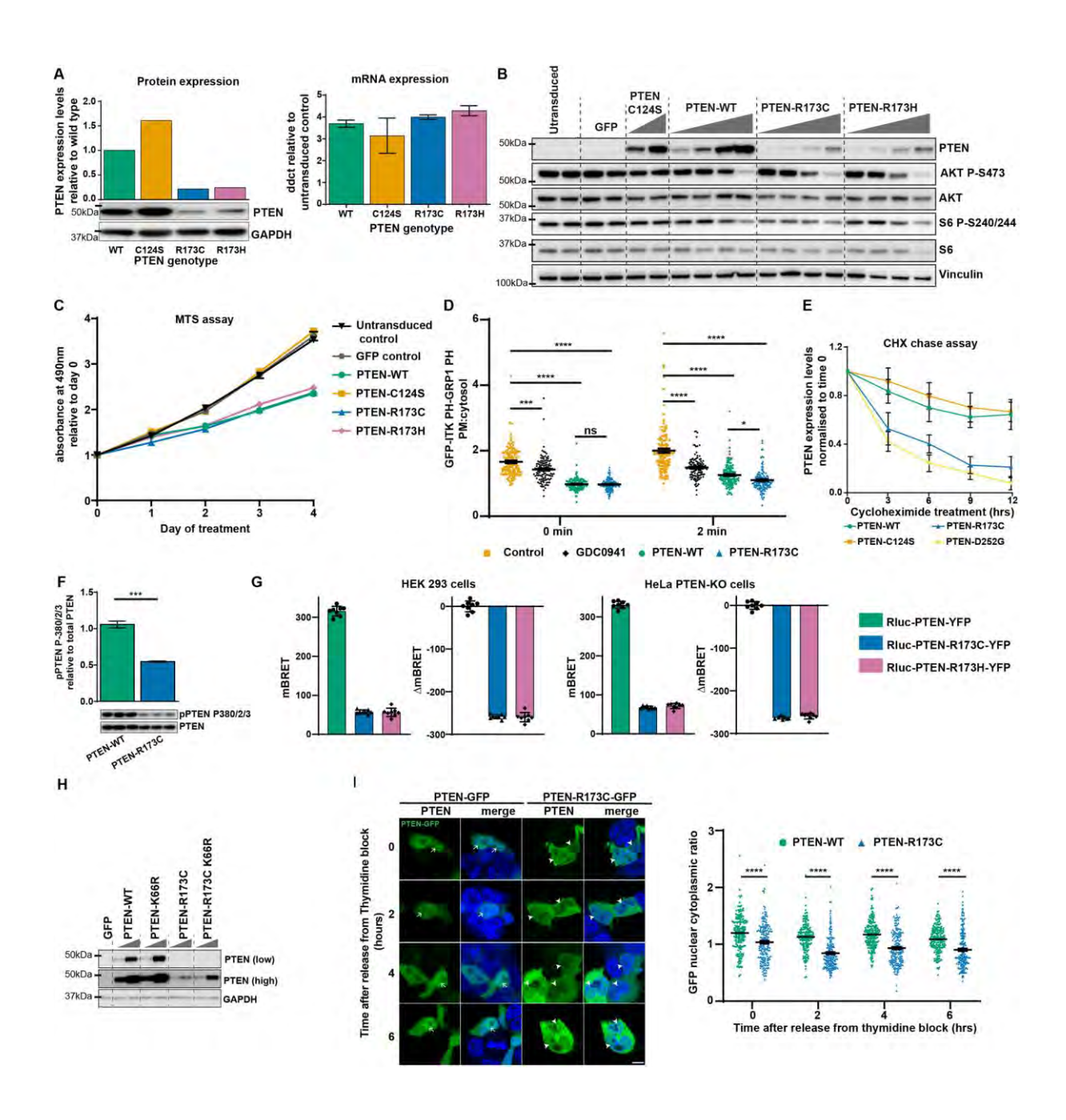


Fig. 1. Characterisation of PTEN-R173C/H. (A-F, H) Transient lentiviral expression in U87 cells of PTEN-WT or mutants at fixed (A, C-F, H) or increasing concentrations of lentiviral particles (B). (A) qPCR analysis was performed to determine PTEN mRNA levels (mean±SEM, n=3, right panel). (A and B) PTEN expression and (B) AKT P-S473 and S6 P-S240/244 assessed by immunoblotting. (B) Representative immunoblot from n=3. (C) Cell proliferation as determined by MTS assay over 4 days. Graph shows the mean±SEM of absorbance at 490 nm relative to day 0 from 10 replicate wells of a representative experiment from n=2. (D) U87 cells expressing a PIP₃ biosensor, with or without

PTEN-WT or PTEN-R173C, were pre-treated + GDC-0941 (1 μM) for 1 h, followed + insulin treatment (100 nM) for 2 min. Mean fluorescence intensity (MFI) of the PIP₃ biosensor at the plasma membrane normalized to the MFI of the PIP₃ biosensor in the cytosol shown as mean±SEM from 3 independent experiments, analysed using 2-way ANOVA. (E) Cells were treated with cycloheximide and PTEN protein expression levels determined by immunoblotting at the indicated time points. Graph shows PTEN protein levels normalized to time 0, data shown as mean±SEM, n=6. (F) Phosphorylation of PTEN on S380/T382/T383 was determined by immunoblotting. Graph shows mean ± SEM, n=3, analysed using unpaired t-test. (G) mBRET and ΔmBRET values, obtained in live HEK-293T and HeLa PTEN KO cells, transfected with Rluc-PTEN-WT-YFP, Rluc-PTEN-R173C-YFP or Rluc-PTEN-R173H-YFP. Graphs represent mean±SD of n=8 points from a representative experiment from 3 independent experiments. (H) Protein extracts from U87 cells were used for immunoblotting to assess PTEN protein levels. (I) Lenti-X™ 293T cells expressing GFP-tagged PTEN-WT or PTEN-R173C were arrested in the G1/S phase of cell cycle by double-thymidine block and imaged by confocal microscopy at the indicated time points after release from thymidine block, for expression of PTEN-GFP. Left panel shows representative images, arrows indicate nuclear PTEN-WT or reduced nuclear PTEN-R173C, scale bar: 10 μm. Graph shows the nuclear:cytoplasmic ratio of the MFI of the PTEN-GFP signal (mean±SEM; n=3, analysed using 2-way ANOVA followed by Tukey's multiple comparison test). *p<0.05; ***p<0.001; ****p<0.0001; ns, not-significant (p>0.05).

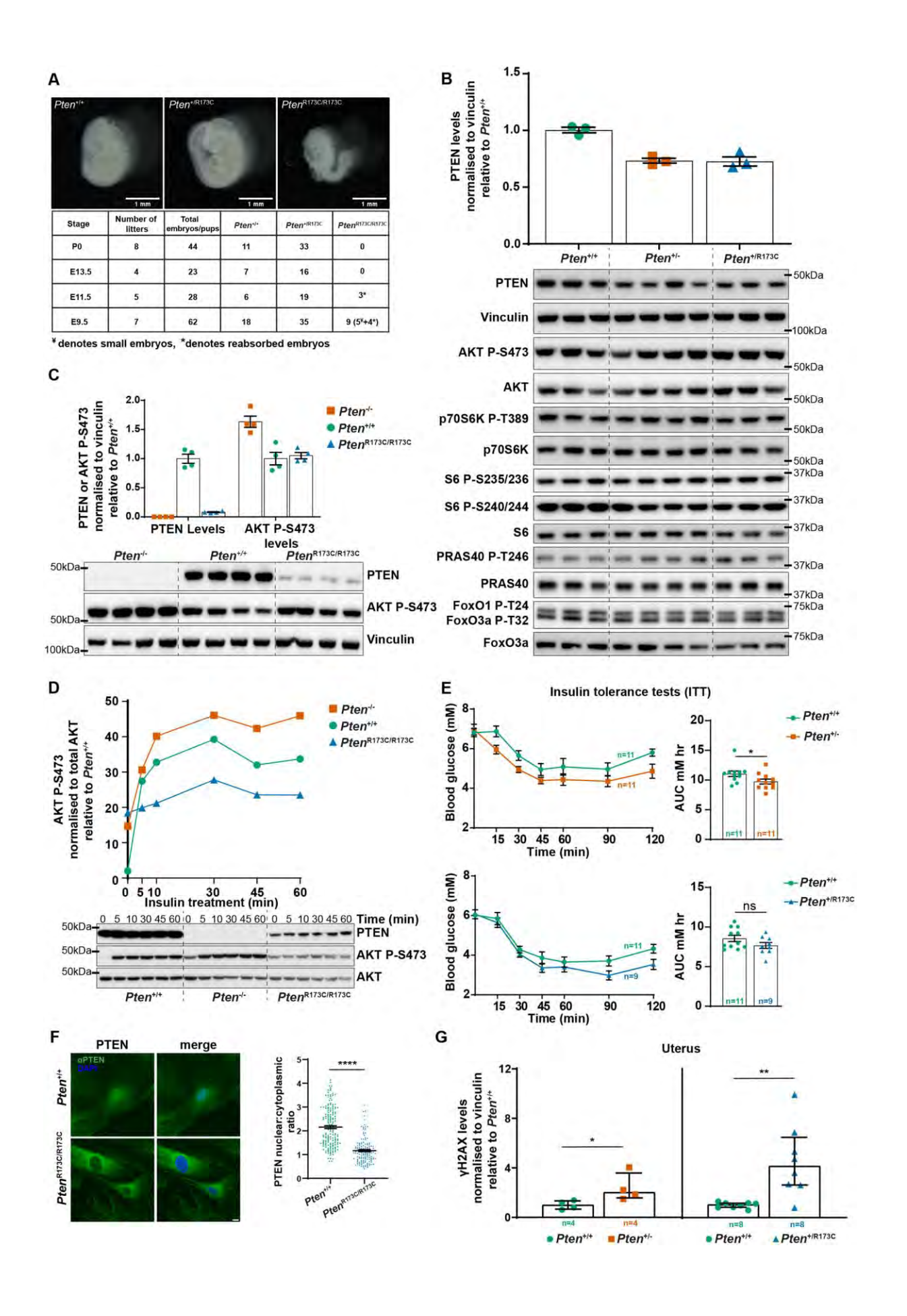


Fig. 2. Characterisation of Pten^{+/R173C} mice. (A) Images show morphology of E9.5 Pten^{+/+}, Pten^{+/R173C} and Pten^{R173C/R173C} embryos,scale bar: 1 mm, table shows the number of embryos/pups of each genotype obtained at the indicated time points. ¥ indicates embryos smaller in size and * indicates embryos that had been reabsorbed. (B, C) Protein extracts from MEFs of the indicated genotype were used for immunoblotting with the antibodies shown. Data shown as mean±SEM. At least 3 independent MEF lines of each were used for (B) and 2 independent MEF lines were used for (C). (D) MEFs of the indicated genotype were treated with insulin (100 nM) for the indicated times and protein extracts immunoblotted with the antibodies shown. Data shown as mean from 2 independent MEF lines for each genotype. (E) ITT assays on 3-month-old male mice of the indicated genotypes. XY curves show blood glucose levels post insulin injection over time. Bar graphs show mean ± SEM of measurements of Area Under the Curve (AUC), analysed using unpaired t-test. (F) MEFs of the indicated genotype were arrested in the G1/S phase of the cell cycle by doublethymidine block, immunostained with antibodies to PTEN (green) and DAPI (blue) and imaged by confocal microscopy 6 h after release from thymidine block. Scale bar: 10 µm. Graphs show nuclear:cytoplasmic ratio of the GFP MFI (mean±SEM from 3 independent experiments) analysed using unpaired t-test. (G) 6-week-old mice of the indicated genotypes were treated with 7Gy yradiation and protein extracts from uterus were used for immunoblotting. Graph shows levels of yH2AX relative to littermate Pten+++ controls as median with interquartile rangeanalysed using Mann-Whitney U tests.. *p<0.05; **p<0.01;; ****p<0.0001; ns, not-significant (p>0.05). Mice used for generating MEF lines in (A-D and F) and in (E and G) were on a C57BL/6J background.

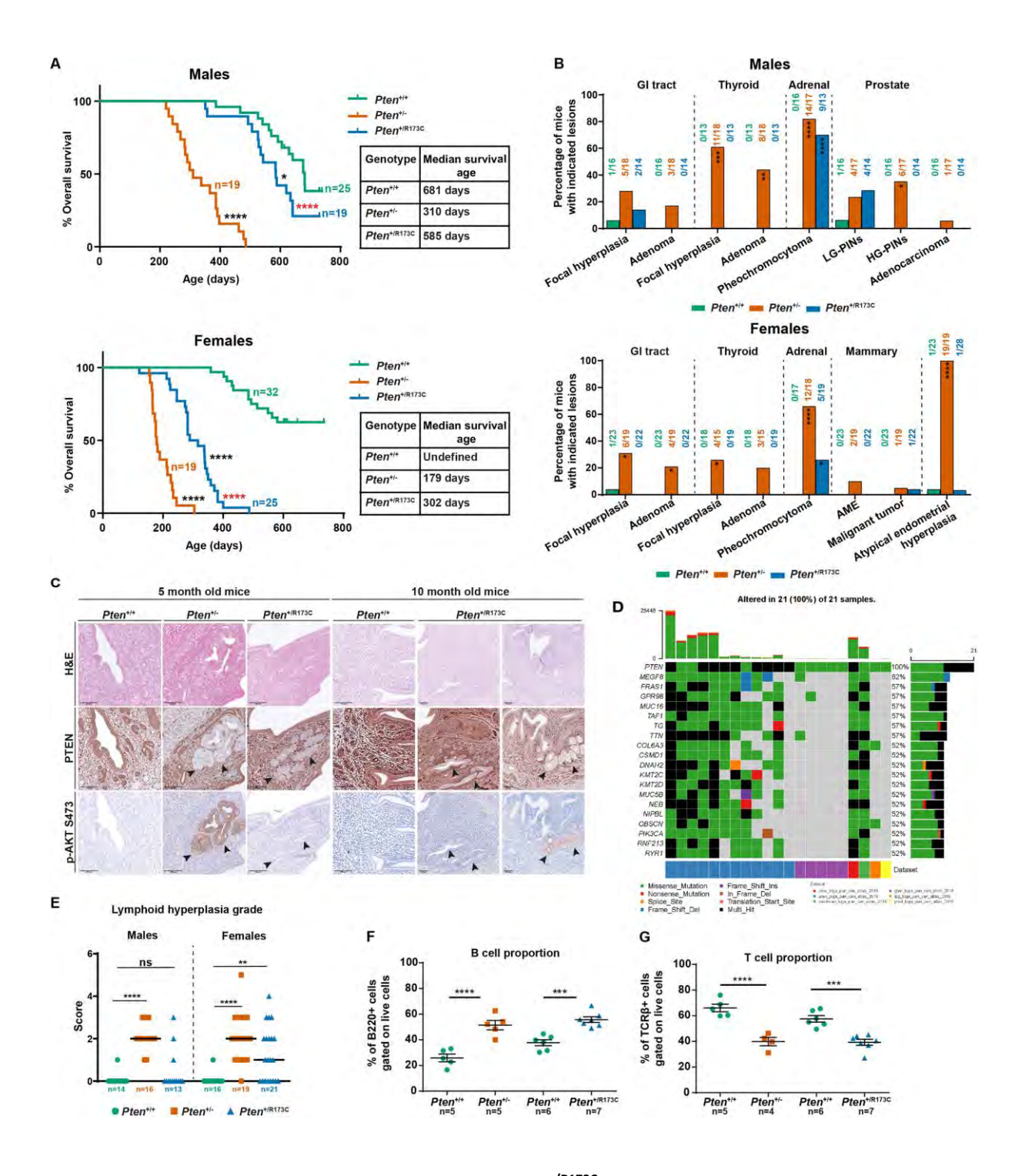


Fig. 3. Survival and histopathological analysis of *Pten*^{+/R173C} mice. Mice on a mixed C57BL/6J x Sv129 background were allowed to age and euthanized for welfare reasons or at a specified age. (A) Kaplan–Meier survival curves for male and female mice analysed using Log-rank (Mantel–Cox) test and Gehan–Breslow–Wilcoxon test. Comparisons were made to *Pten*^{+/+} mice (p-values shown as black stars) or *Pten*^{+/-} mice (p-values shown as red stars). Table show median survival age of the mice. (B) Incidence of specific tumour types in male and female mice, as assessed by histopathological analysis on all mice, analysed performed using Fisher's exact test. (C) Representative IHC images of uteri from female mice at the indicated timepoints, black arrowheads indicate loss of PTEN

immunoreactivity and the corresponding AKT P-S473 immunoreactivity. **(D)** Oncoplot showing cooccurrence of mutations in the indicated genes in tumor samples harbouring PTEN-R173C mutation (cBioportal). **(E)** . Scatter plot of lymphoid hyperplasia scores from individual mice at the end of study with line at median, analysed using Fisher's exact test. **(F-G)** Flow cytometry analysis was performed on the lymph nodes of female $Pten^{+/R173C}$, $Pten^{+/-}$ and littermate $Pten^{+/+}$ controls at 5 and 10 months of age. Graphs show the proportion of (F) B220+ B-cells and (G) TCR β + T-cells, analysed using oneway ANOVA . *p<0.05; **p<0.01; ***p<0.001; ****p<0.0001; ns, not-significant (p>0.05).

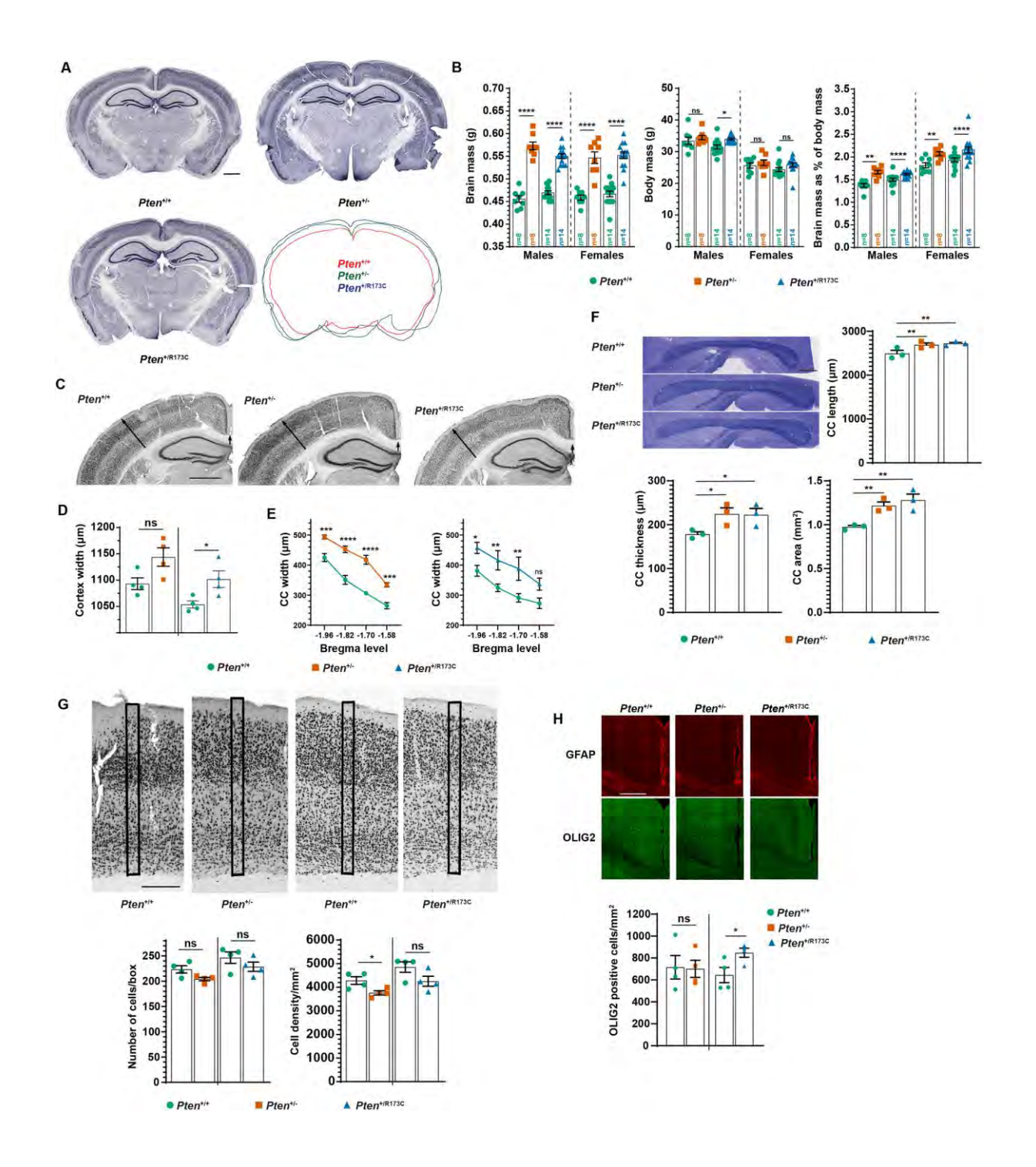


Fig. 4. Enlarged brain phenotype with associated changes in grey and white matter areas in *Pten* mutant mice. (A) Representative NeuN immunostaining of coronal sections. The overlay of the contours of the depicted slices is also shown, scale bar: $1000 \, \mu m$. (B) Brain mass, body mass and brain mass as a % of body mass shown as mean±SEM, analysed using two-way ANOVA followed by Tukey's multiple comparison test. (C) Representative NeuN immunostaining from coronal sections, scale bar: $1000 \, \mu m$. (D) Quantification of cortical thickness in the primary somatosensory cortex barrel field (area indicated with long arrows in C) from n=4 mice of each sex and genotype shown as mean±SEM, analysed using Two-tailed unpaired t-test. (E) Quantification of the thickness of the

corpus callosum at the indicated Bregma levels (area indicated with short arrows in C) from n=4 mice of each sex and genotype, shown as mean±SEM, analysed using Two-way RM ANOVA with uncorrected Fisher's LSD test. (**F**) Representative sagittal sections from mouse brains at Bregma level stained with Toluidine Blue, scale bar: 500 µm and quantification of the corpus callosum length, thickness, and area.from n=3 mice per genotype shown as mean±SEM, analysed using One-way RM ANOVA followed by uncorrected Fisher's LSD test. (**G**) Top: Representative images of coronal sections from the somatosensory cortex stained for NeuN, scale bar: 250 µm. Bottom: Quantification of the number and density of neurons in the indicated boxed areas in (G), from n=4 mice of each sex each genotype shown as mean±SEM; analysed using Two-tailed unpaired t-test. (**H**) Top: Representative images of sections immunostained with OLIG2 and GFAP, scale bar: 100 µm, and bottom: quantification of OLIG2 positive cells in the motor cortex from n=4 mice per genotype shown as mean±SEM analysed using Two-tailed unpaired Student's t-test. *p<0.05; **p<0.01; ***p<0.001; ****p<0.001; ns, not-significant (p>0.05). Mice used were 3-month-old on a mixed C57BL/6J x Sv129 background.

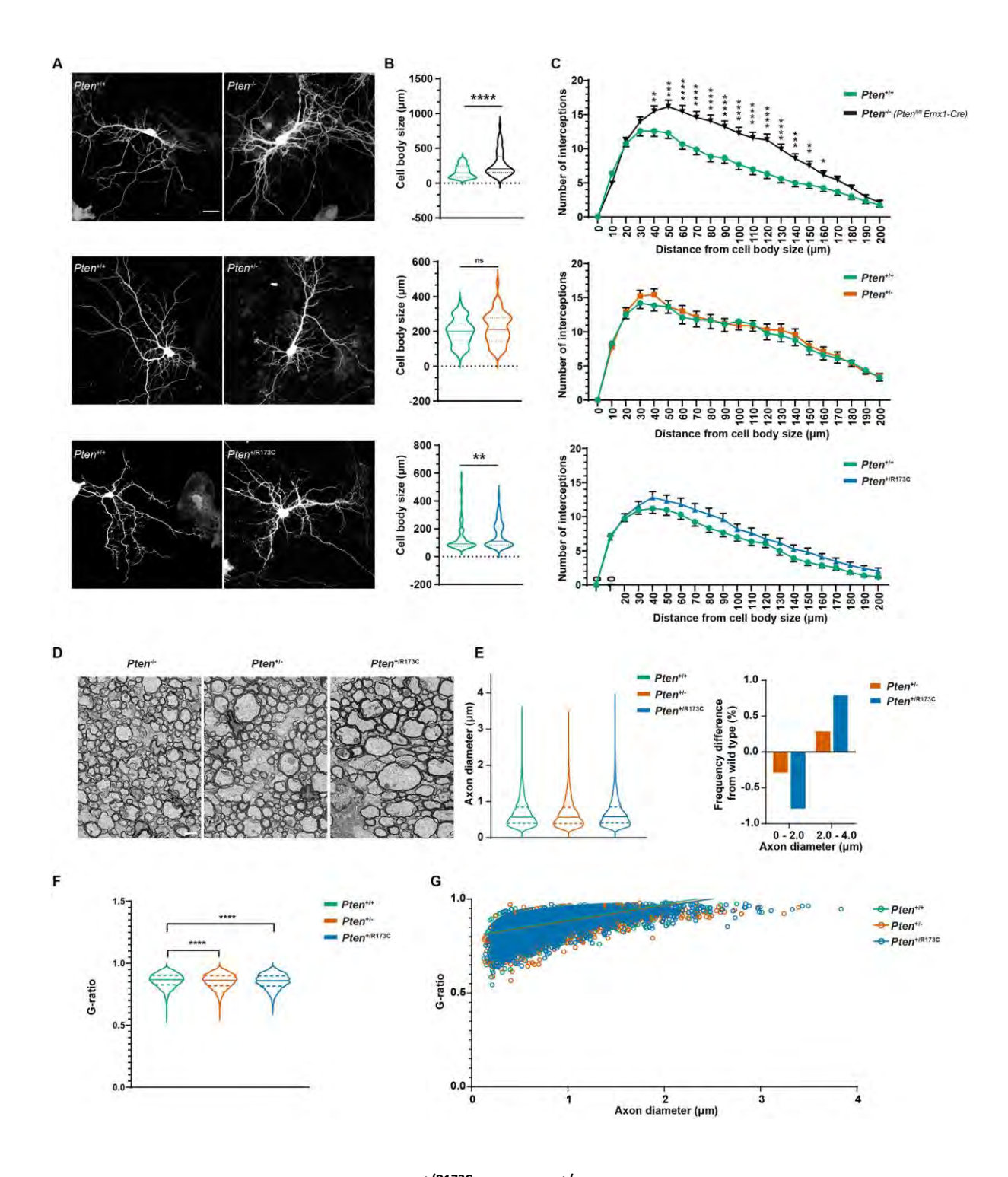


Fig. 5. Neuronal and glial deficits in *Pten*^{+/R173C} and *Pten*^{+/-} mice. (A) Representative images from GFP-transfected cortico-hippocampal neurons at DIV12/13. Neurons were stained for GFP, scale bar: 20 μm. (B) Quantification of cell body size of neurons shown in (A) from n>60 cells for each genotype from 3-6 independent experiments. Violin plots show median (thick line) and interquartile range (dotted lines), analysed using Mann-Whitney test. (C) Sholl analysis of neurons shown in (A) from n=63–122 cells from 3–5 independent experiments shown as mean±SEM, analysed using Two-way RM ANOVA followed by uncorrected Fisher's LSD test. (D) Representative electron micrographs of

the corpus callosum in cross-sections from 3-month-old mice, scale bar: 1 μ m. (**E**) Quantification of axonal dimeters and their frequency difference from >4500 axons measured from n=3 mice per genotype. Violin plots show median (thick line) and interquartile range (dotted lines), analysed using Kruksal-Wallis test. (**F**) Quantification of g-ratios for corpus callosum axons from >4500 axons measured from n=3 mice per genotype analysed using Kruskal-Wallis test followed by Dunn's multiple comparisons test. (**G**) Scatter plot of g-ratios as a function of axon diameter from >4500 axons measured from n=3 mice per genotype. Linear regression analysis showed no statistical differences among the three genotypes *p< 0.05; **p<0.01; ***p<0.001; ****p<0.0001; ns, not-significant (p>0.05). Mice used in (A-C) were on a C57BL/6J background, and in (D-G) on a mixed C57BL/6J x Sv129 background.

Table 1. Clinical phenotypes of PHTS patients with *Pten-R173* variants and other nuclear excluded *Pten* variants

mo, age in months; y, age in years; m, males; f, females, NR, not recorded. Phenotypic categories include the following: Developmental disorders; global developmental delay, delay in speech development, mental retardation, autism spectrum disorder, special educational needs. Cutaneous pathology; hamartomas, tricholemmoma, mucocutaneous lesions, acral keratoses, palmoplantar keratoses, oral papillomas, penile freckling, facial papules, café-au-lait spots, skin tags. Vascular abnormalities; haemangiomas, venous malformations, arterio-venous malformations. Immune/lymphoid features; recurrent upper respiratory tract infections, hypogammaglobulinemia, enlarged tonsils and adenoids, lymphadenopathy, splenomegaly. Thyroid benign lesions; cyst, nodules, adenomas. Thyroid malignant cancer; follicular cancer, papillary-follicular thyroid cancer. Breast benign lesions; fibrocystic disease of the breast, fibroadenomas, benign breast disease. Breast malignant cancer; ductal breast carcinoma, invasive ductal carcinoma and ductal carcinoma in-situ of the breast. Ovary benign lesions; ovarian cysts, benign neoplasm. Ovary malignant cancer; malignant neoplasm of the ovary. Uterus benign lesions; uterine fibroids, endometrial polyp. The phenotypes of individual patients are listed in Tables S1 and S2.

		PHTS patients with other nuclear excluded <i>PTEN</i> variants	PHTS patients with <i>PTEN</i> R173 variants	Both groups combined		
	Number of patients	25	34	59		
Patient demographics (N)	Age range (median age)	1 year-40 years (6 years)	7 months-63 years (12.5 years)	7 months-63 years (10 years)		
	Gender distribution N (%)	Males: 12 (48%) Females: 9 (36%) NR: 4 (16%)	Males: 19 (56%) Females: 14 (41%) NR: 1 (3%)	Males: 31(52%) Females: 23 (39%) NR: 5 (8%)		
Phenotypes (N (%))						
Neuro-developmental	Macrocephaly	21 (84%)	32 (94%)	53 (90%)		
	Developmental disorders	16 (64%)	18 (53%)	34 (58%)		
Cutaneous and vascular features	Cutaneous pathology	12 (48%)	16 (47%)	28 (47%)		
	Vascular abnormalities	3 (12%)	5 (15%)	8 (14%)		

a	
.은	
Œ	
U	
S	
_ =	
ā	
ë	
⁻	
_	
Q	
Φ	
ب	
Ω	
Φ	
Ū	
ŭ	
ď	
$\overline{}$	
2	
\sim	
_	
•	
·S	
. SL	
· sw	
. SL	
· sw	
anisms •	
• smsiu	
anisms •	
hanisms •	
chanisms •	
chanisms •	
chanisms •	
chanisms •	
& Mechanisms •	
ls & Mechanisms •	
& Mechanisms •	
ls & Mechanisms •	
ls & Mechanisms •	
dels & Mechanisms •	
dels & Mechanisms •	
dels & Mechanisms •	
Models & Mechanisms •	
Models & Mechanisms •	
Models & Mechanisms •	
Models & Mechanisms •	

	Lipomas 4 (169		-	4 (7%)	
	Malignant cancer of skin	-	1 (3%) Age: 63 years	1 (1.7 %)	
	Benign lesions	4 (16%)	6 (18%)	10 (17%)	
Thyroid	Malignant cancer	1 (4%) 29 years			
Gastro-intestinal	Benign polyps	5 (20%)	4 (12%)	9 (15%)	
Breast	Benign lesions	1 (4%)	2 (6%)	3 (5%)	
	Malignant cancer	-	2 (6%) Ages: 54 years and 59 years	2 (3%)	
	Benign lesions	-	3 (9%)	3 (5%)	
Ovary	Malignant cancer	-	1 (3%) Age: 63 years	1 (1.7 %)	
Uterus	Benign lesions	-	3 (9%)	3 (5%)	
Other cancers	Testicular cancer	1 (4%) Age: 29 years	-	1 (1.7%)	
	Lung cancer	1 (4%) Age: NR	-	1 (1.7%)	

Table 2. Neuronal and behavioural phenotypes in mice with *Pten* **mutations**: Table shows data from *Pten*^{+/R173C}, *Pten*^{+/-}, and conditional *Pten*^{-/-} mice from this study, and *Pten*^{+/m3m4} and Pten^{m3m4/m3m4} mice as reported in (Mester et al., 2011, Tilot et al., 2014). NT; not tested. The behavioural assays (sociability, motor coordination and locomotion) are relative to wild type littermate mice.

Dhanaturas	Mouse genotype					
Phenotypes	Pten ^{+R173C}	Pten ^{+/-}	Pten ^{-/-}	Pten ^{+/m3m4}	Pten ^{m3m4/m3m4}	
Increased brain size	Yes	Yes	NT	Yes	Yes	
Bigger corpus callosum	Yes	Yes	NT	NT	NT	
Increased numbers of oligodendroglia cells	Yes	No	NT	No	Yes	
Astrogliosis	No	No	NT	No	Yes	
Increased cell body size	Yes	No	Yes	No	Yes	
Increased neuronal complexity	No	No	Yes	No	No	
Enlarged axons	Yes	Yes	NT	NT	NT	
Thicker myelin	Yes	Yes	NT	NT	NT	
Sociability	No significant difference	NT	NT	No significant difference	Too social with revised criteria	
Motor coordination	NT	NT	NT	NT	reduced	
Locomotion	reduced	NT	NT	NT	NT	

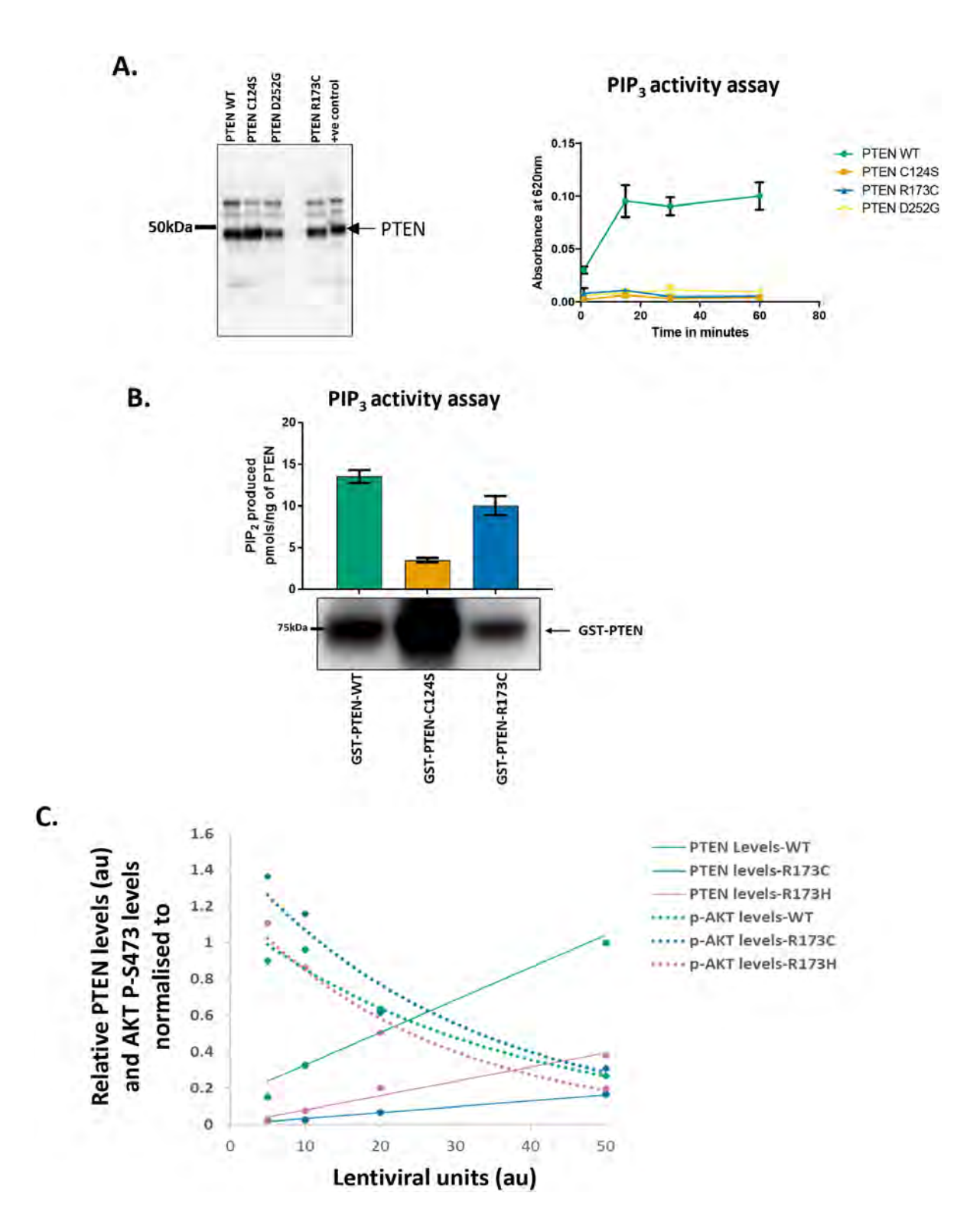


Fig. S1. Characterisation of PTEN-R173C. (A) Recombinant untagged PTEN wild-type (WT) and mutant proteins were purified from *E. coli* and used in a PIP₃ lipid phosphatase assay. *Left,* Coomassie blue-stained SDS-PAGE gel showing the level of purified recombinant protein. A previous batch of purified PTEN protein is used as a positive control. *Right,* Graph showing PTEN activity measured as absorbance at 620 nm in a malachite green assay. Data shown as mean ±SEM from n=3. (B) Affinity-purified GST-tagged PTEN wild-type and mutant proteins expressed in Lenti-X 293T cells were subjected to a PIP₃ lipid phosphatase assay. Graph shows PIP₂ produced per ng of recombinant PTEN from one experiment. Data show mean±SEM from three technical replicates. Immunoblot of GST-PTEN expression levels is shown under the graph. (C) Quantification of PTEN and p-AKT from blots from Fig. 1B, au: arbitrary units. p-AKT levels have been normalised to untransduced controls.

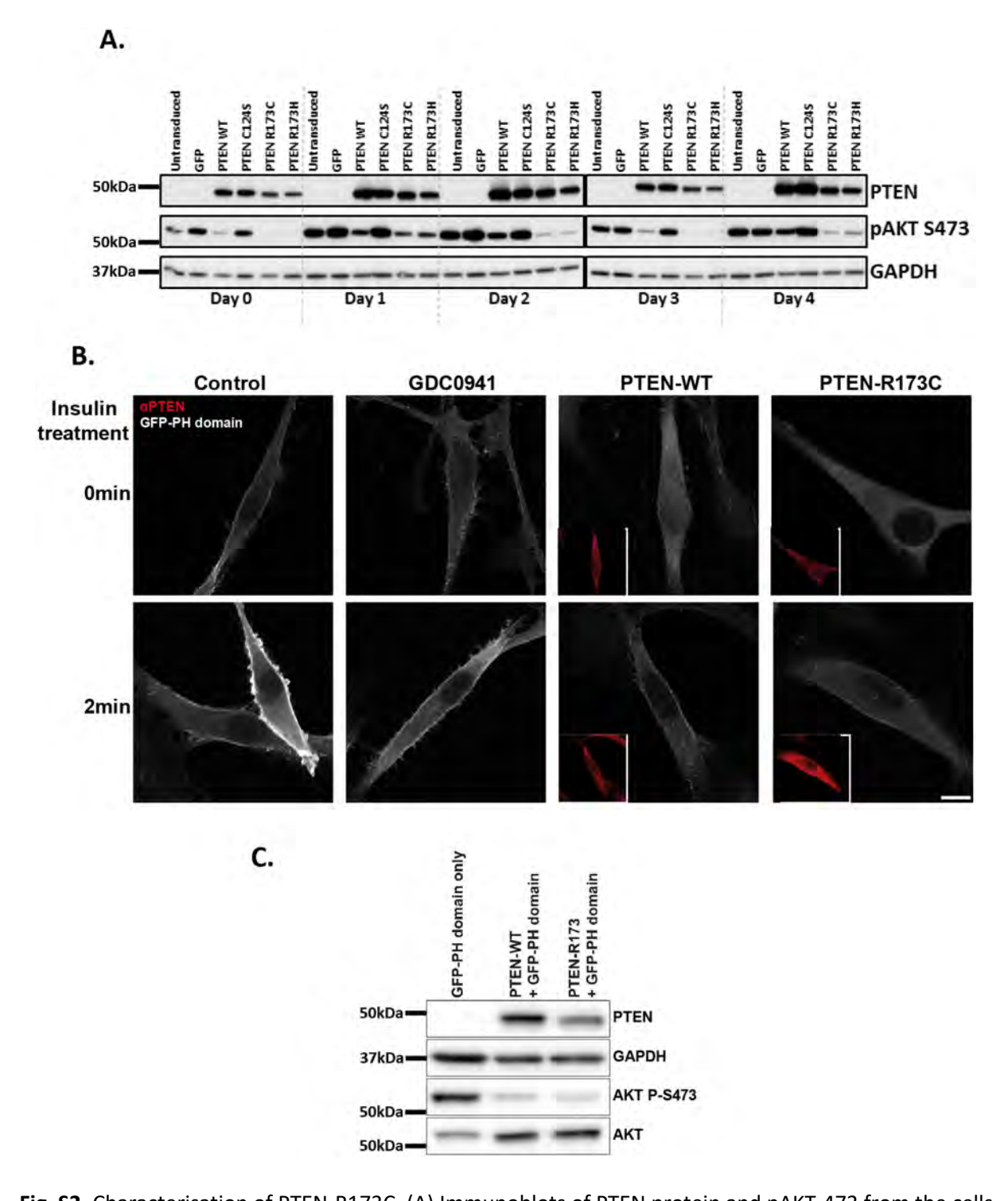
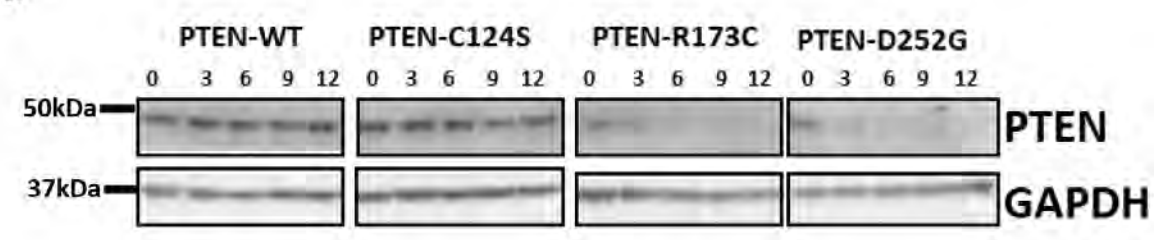
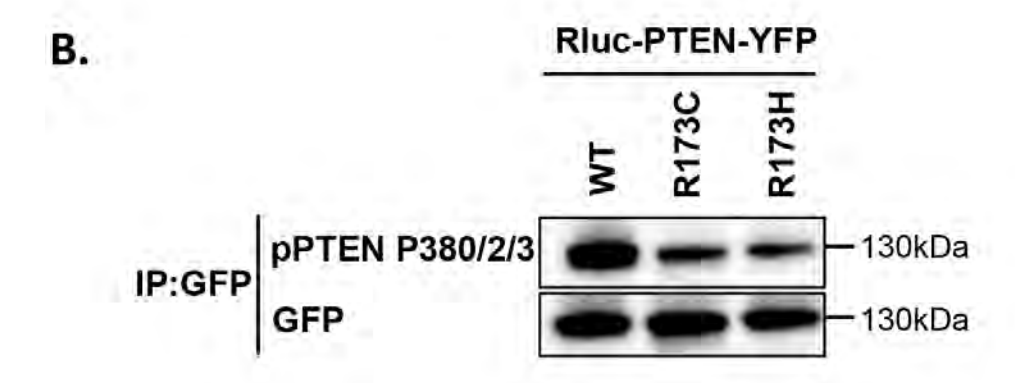


Fig. S2. Characterisation of PTEN-R173C. (A) Immunoblots of PTEN protein and pAKT-473 from the cells in Fig. 1C. (B) U87 cells, transiently transduced with lentivirus encoding a PIP $_3$ biosensor, with or without PTEN-WT or PTEN-R173C, were pre-treated \pm GDC-0941 (1 μ M) for 1 h, followed \pm insulin treatment (100 nM) for 2 min. The cells were stained with antibodies to PTEN (red inset) and imaged by confocal microscopy. Quantification of the mean fluorescence intensity (MFI) of the PIP3 biosensor is shown in Fig. 1D. (C) Immunoblots of PTEN, AKT P-S473, AKT and GAPDH from the cells in (B) and Fig. 1D.







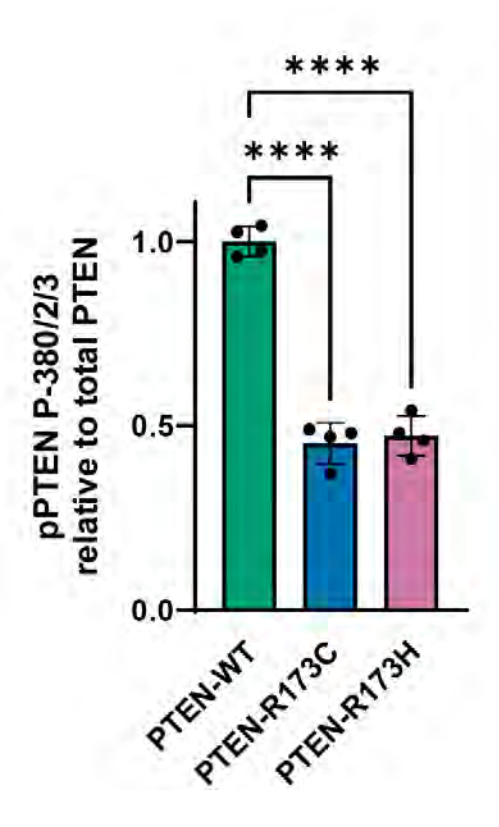


Fig. S3. Characterisation of PTEN-R173C. (A) Transient lentiviral expression of PTEN wild-type (WT) or the indicated PTEN mutants in U87 cells. The cells were treated with cycloheximide, and PTEN protein expression levels were determined by immunoblotting at the indicated time points. Representative blots are shown. (B) Lysates of HEK-293T cells expressing Rluc-PTEN-WT-YFP, Rluc-PTEN-R173C-YFP or Rluc-PTEN-R173H-YFP were immunoprecipitated using anti-GFP antibodies and immunoblotted for PTEN-P-S380/T382/T383. Representative immunoblots from n=4 showing phosphorylated and total PTEN levels. Graph shows quantification of 4 experiments shown as mean±SEM. Statistical analysis was performed using one-way ANOVA. p-values: ****p<0.0001.

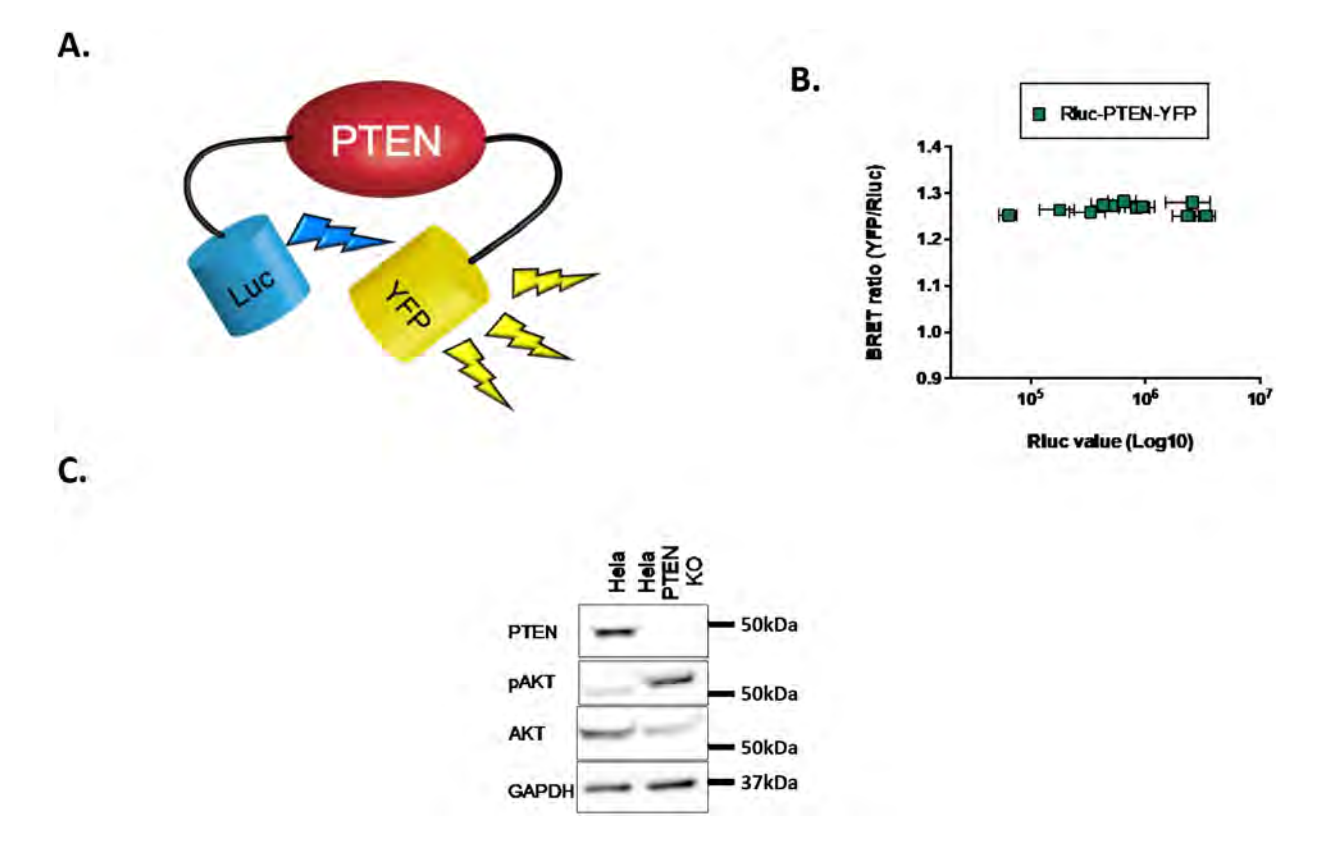
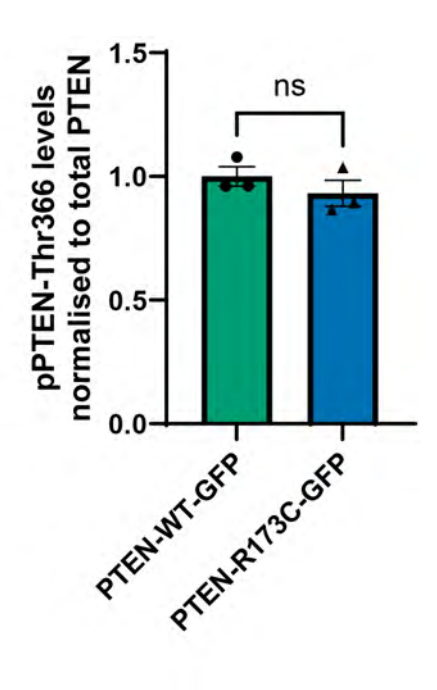


Fig. S4. BRET analysis of PTEN. (A) Cartoon showing the intramolecular bioluminescent resonance energy transfer (BRET)-based biosensor (Rluc-PTEN-YFP). The biosensor can reveal dynamic changes in PTEN conformational rearrangement and function, due to shifts in energy transfer between the donor/acceptor couple. (B) The conformational readout (measured as BRET ratio) is independent from expression levels of the biosensor, as seen by a stable BRET signal when the biosensor (Rluc-PTEN-YFP) is expressed over 2 log differences (measured as Rluc value). (C) Validation of PTEN knock out by immunoblotting in the PTEN-KO HeLa cell line.





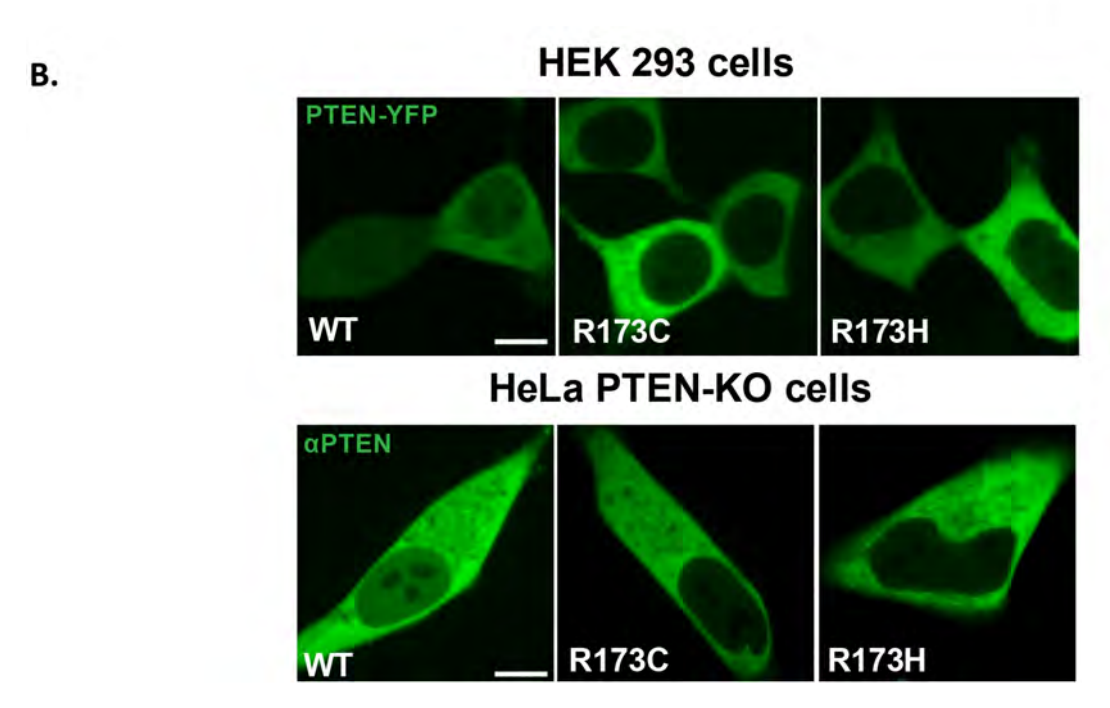


Fig. S5. Investigating protein phosphatase activity and sub-cellular distribution of PTEN-R173 mutants. (A) Lenti-X 293T cells were transfected with plasmids expressing PTEN-WT-GFP or PTEN-R173C-GFP. The cells were lysed, and protein extracts were immunoblotted for pPTEN-Thr366 or total PTEN. Graph on right \S hows mean±SEM pPTEN-Thr366 levels normalised to total PTEN levels from n=3 experiments. Statistical analysis was performed using Unpaired Student's t-test. p-values : ns, not-significant (p>0.05). Corresponding immunoblots shown on the left. (B)Live HEK-293T cells or PTEN-KO HeLa cells expressing Rluc-PTEN-WT-YFP, Rluc-PTEN-R173C-YFP or Rluc-PTEN-R173H-YFP were imaged in 4-well μ slides (IBIDI) by confocal microscopy to assess the subcellular localisation of PTEN-YFP. Figure shows representative images from n=3. Scale bar: 10 μ m.

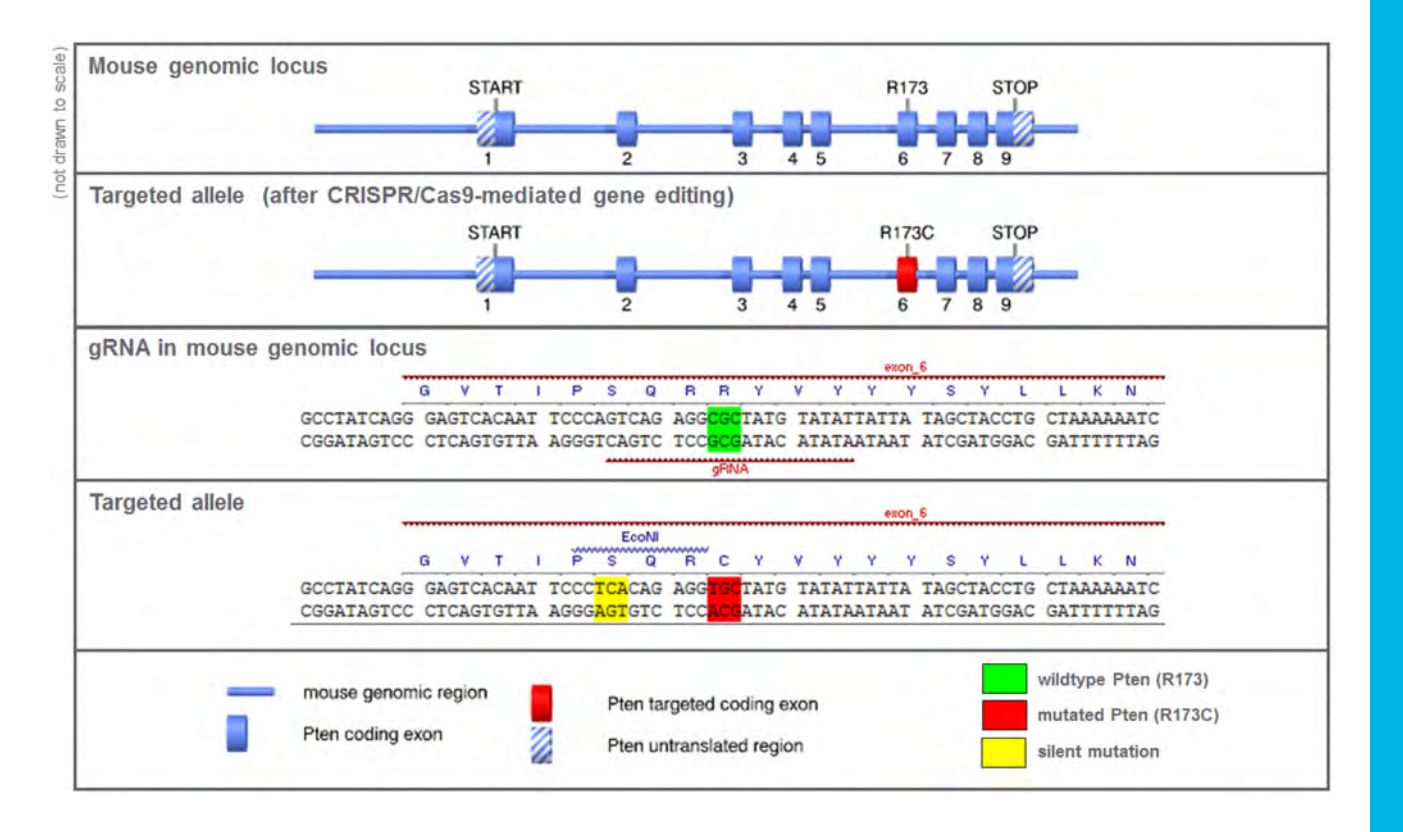


Fig. S6. Generation and characterization of *Pten*^{+/R173C} **mice.** The R173C mutation was introduced into the mouse *Pten* locus using a CRISPR-Cas9 approach. gRNA was designed to contain the R173C mutation (c.517C>T) and a silent mutation containing the *Eco*NI restriction site upstream of the R173 site, to allow discrimination of wild-type and knock-in allele by PCR analysis. The figure above shows the gRNA sequence and the targeting strategy. gRNA was microinjected into C57BL/6J mouse zygotes along with recombinant Cas9. The zygotes were then transferred to pseudopregnant mothers. The litters born (founder animals) were sequenced to check for the incorporation of the R173C mutation and percentage of mosaicism. They were then used as a breeder to generate F1 animals. F1 males positive for the R173C mutation and negative for any off-target mutations were used to generate further animals by IVF using C57BL/6J females.

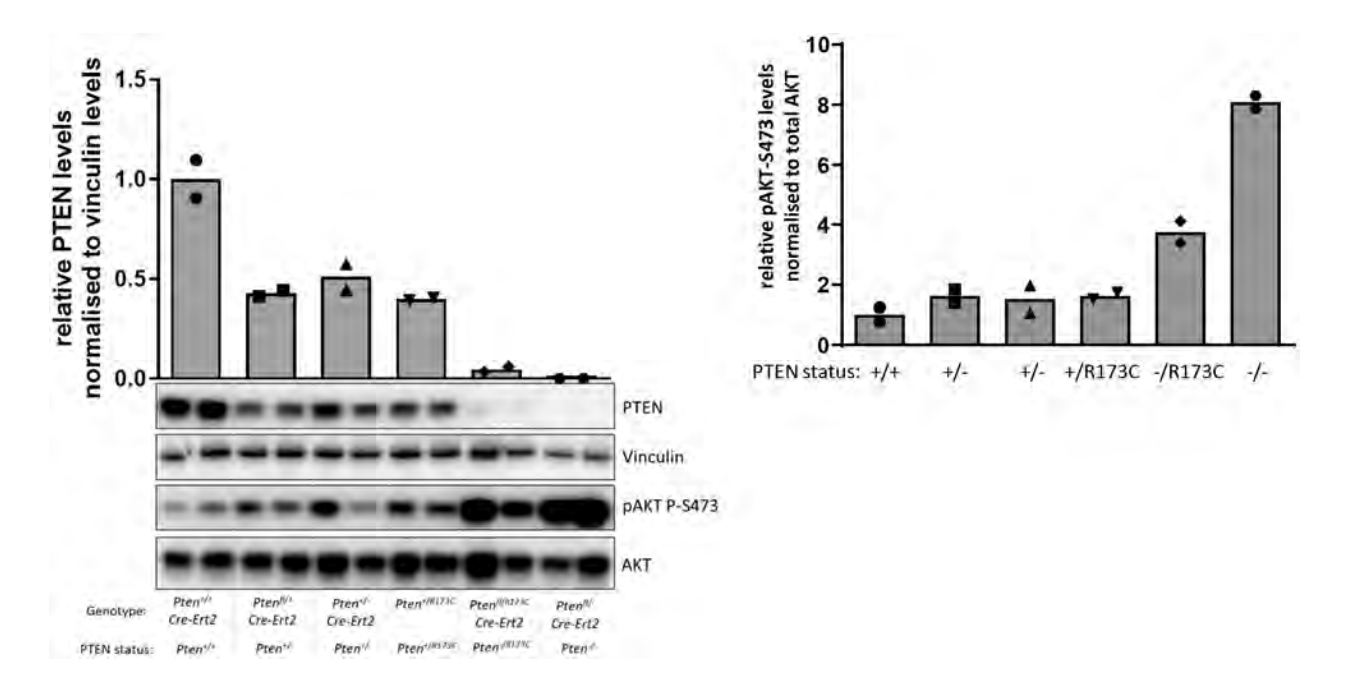


Fig. S7. *In vivo* characterisation of PTEN-R173C. (A) Immunoblots of PTEN protein (quantification in graph on the left) and pAKT-473 (quantification in graph on the right) from MEFs of the indicated genotypes. Quantification shown as mean from 2 MEF lines for each genotype. The MEFs were generated form mice on a C57BL/6J background.

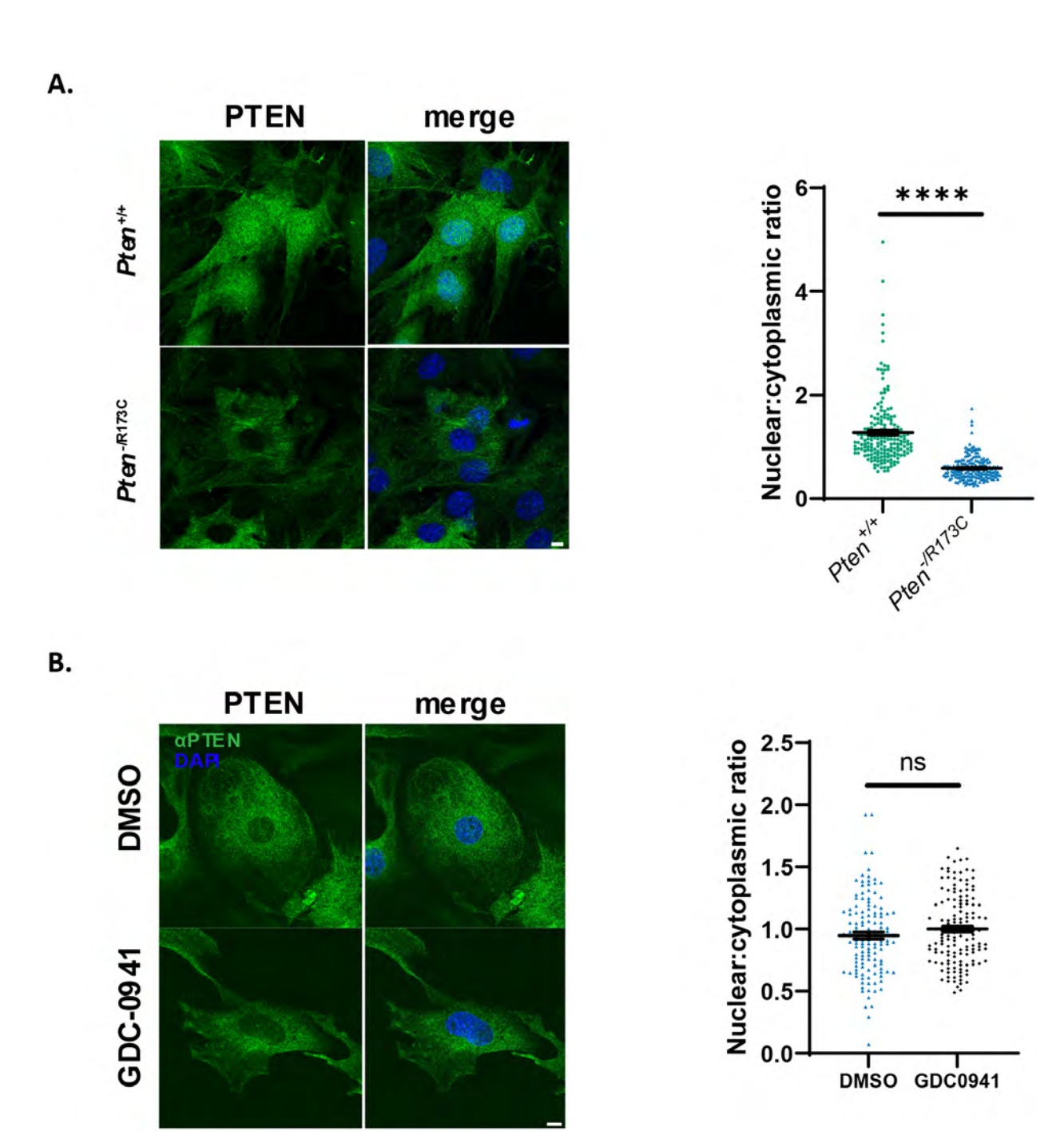
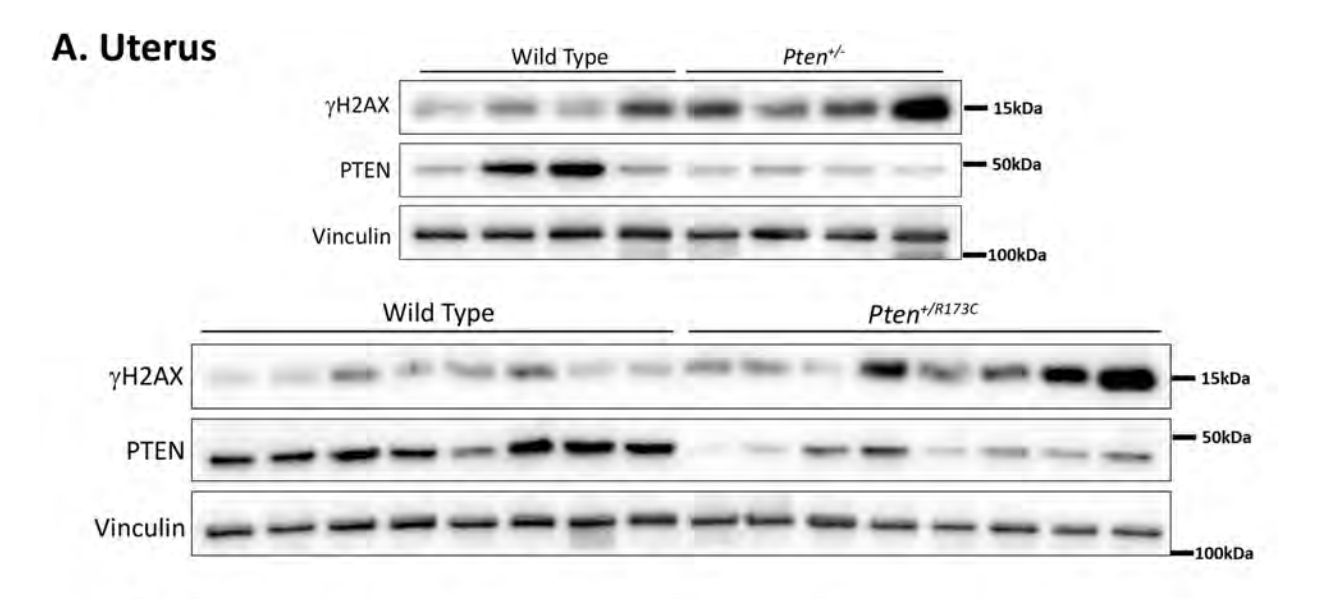
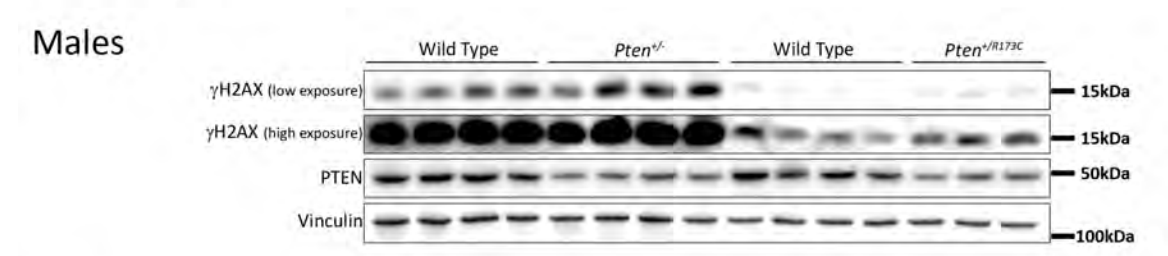
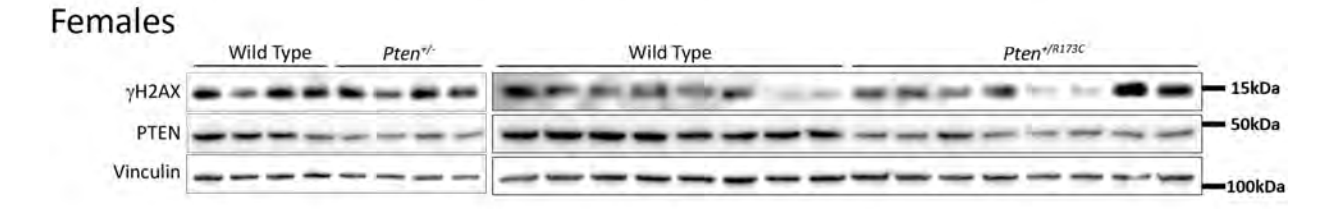


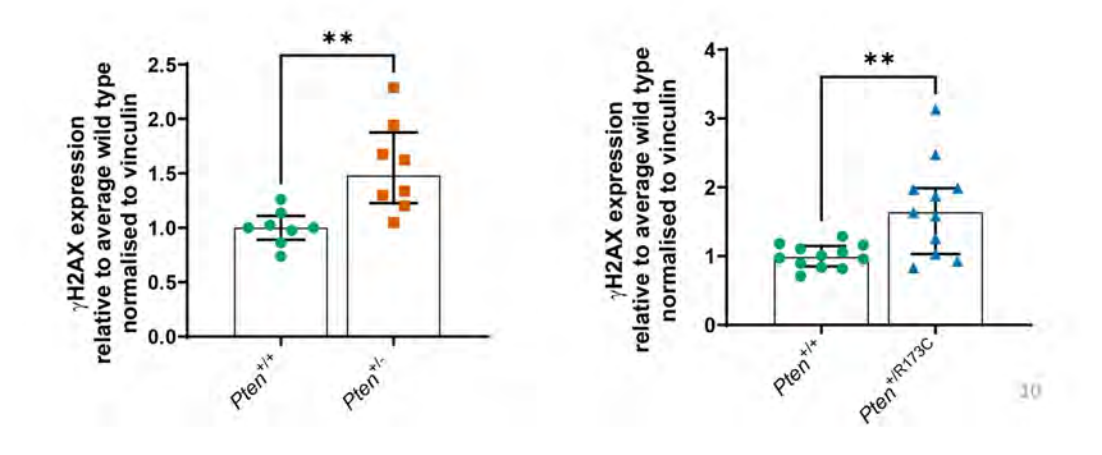
Fig. S8. Sub-cellular localisation of PTEN-R173C. Subcellular localisation of PTEN-R173C. (A-B) MEFs of the indicated genotype were immunostained with antibodies to PTEN (green) and DAPI (blue) and imaged by confocal microscopy. Scale bar: 10 μ m. Cells in (A) were arrested in the G1/S phase of the cell cycle by double-thymidine block and analysed 6 h after release from thymidine block. Cells in (B) were pre-treated with or without GDC-0941 (1 μ M) for 1 h, as indicated. Graphs show nuclear:cytoplasmic ratio of the GFP MFI (mean \pm SEM from 3 independent experiments). Statistical analysis was performed using Unpaired Student's t-test. p-values: ****p<0.0001; ns, not-significant (p>0.05). The MEFs were generated from mice on a C57BL/6J background.



B. Kidney

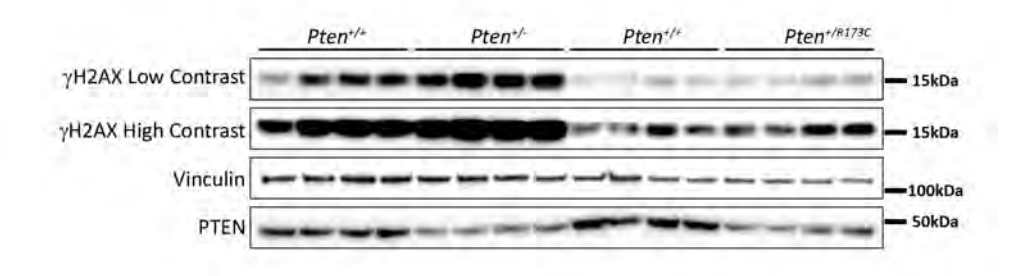






C. Liver

Males



Females

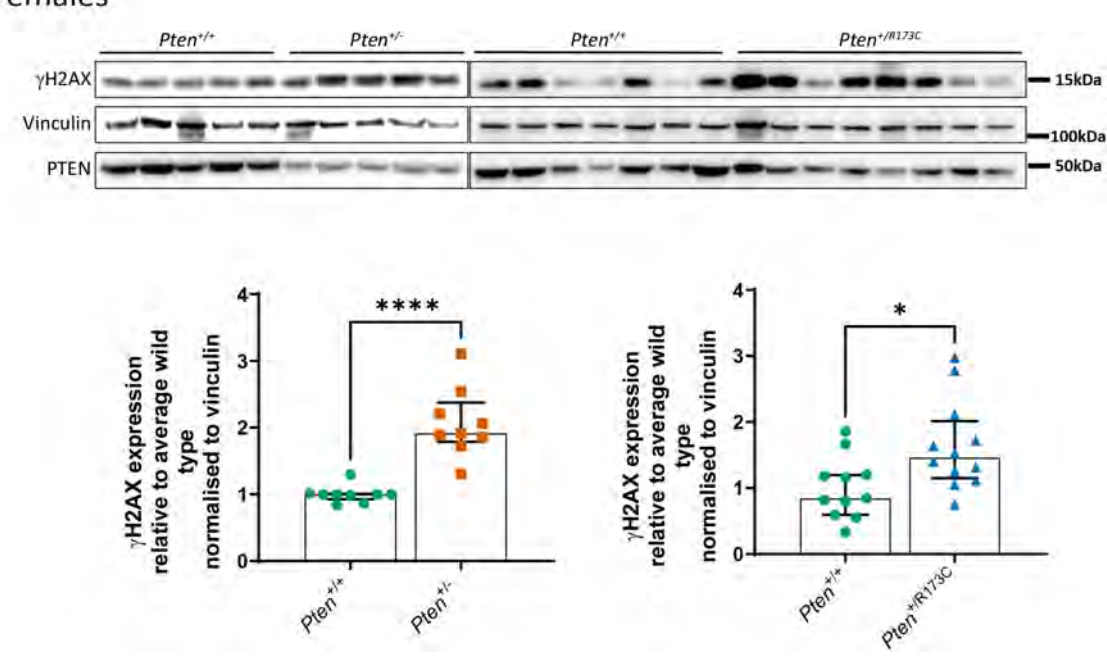
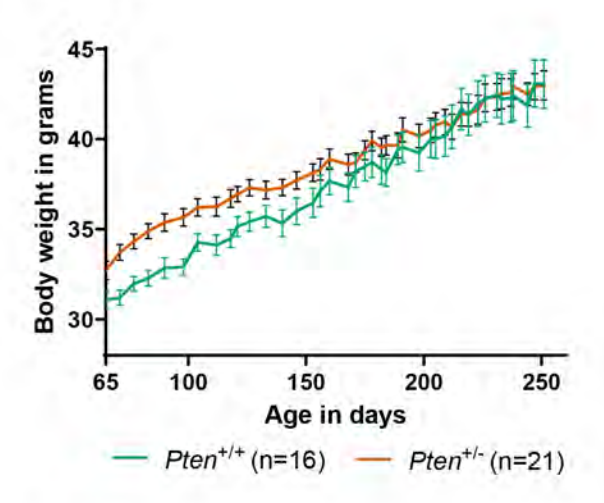
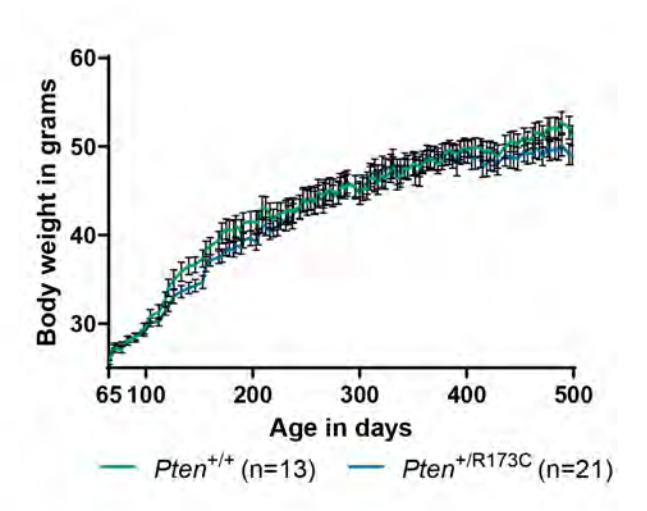


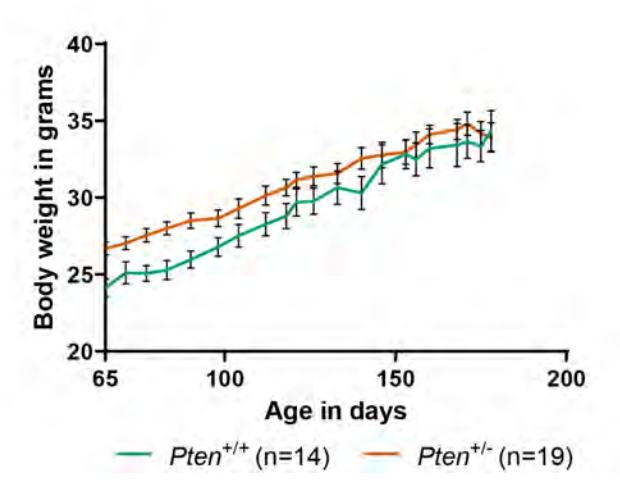
Fig. S9. *In vivo* characterisation of PTEN-R173C. 6-week-old mice on a C57BL/6J background of the indicated genotypes were treated with 7Gy γ -radiation and protein extracts from tissues indicated were used for immunoblotting. Immunoblots showing levels of γ H2AX in (A) uterus (quantification in Fig. 2G), (B) kidney and (C) liver. Graphs show quantification of immunoblots. Bars show median with interquartile range. Pairwise comparisons were performed using Mann–Whitney U test. p-values: *p< 0.05; **p<0.01; ****p<0.0001.

A. Males





B. Females



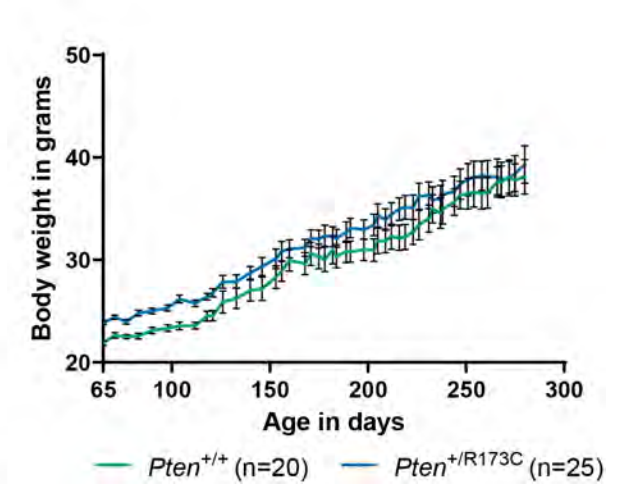


Fig. S10. Age-dependent body weights of *Pten* mutant mice. *Pten*^{+/R173C} and *Pten*^{+/-} mice, and their littermate controls, on a mixed C57BL/6J x Sv/129 background were allowed to age. The mice weighed once a week. Data show mean±SEM.

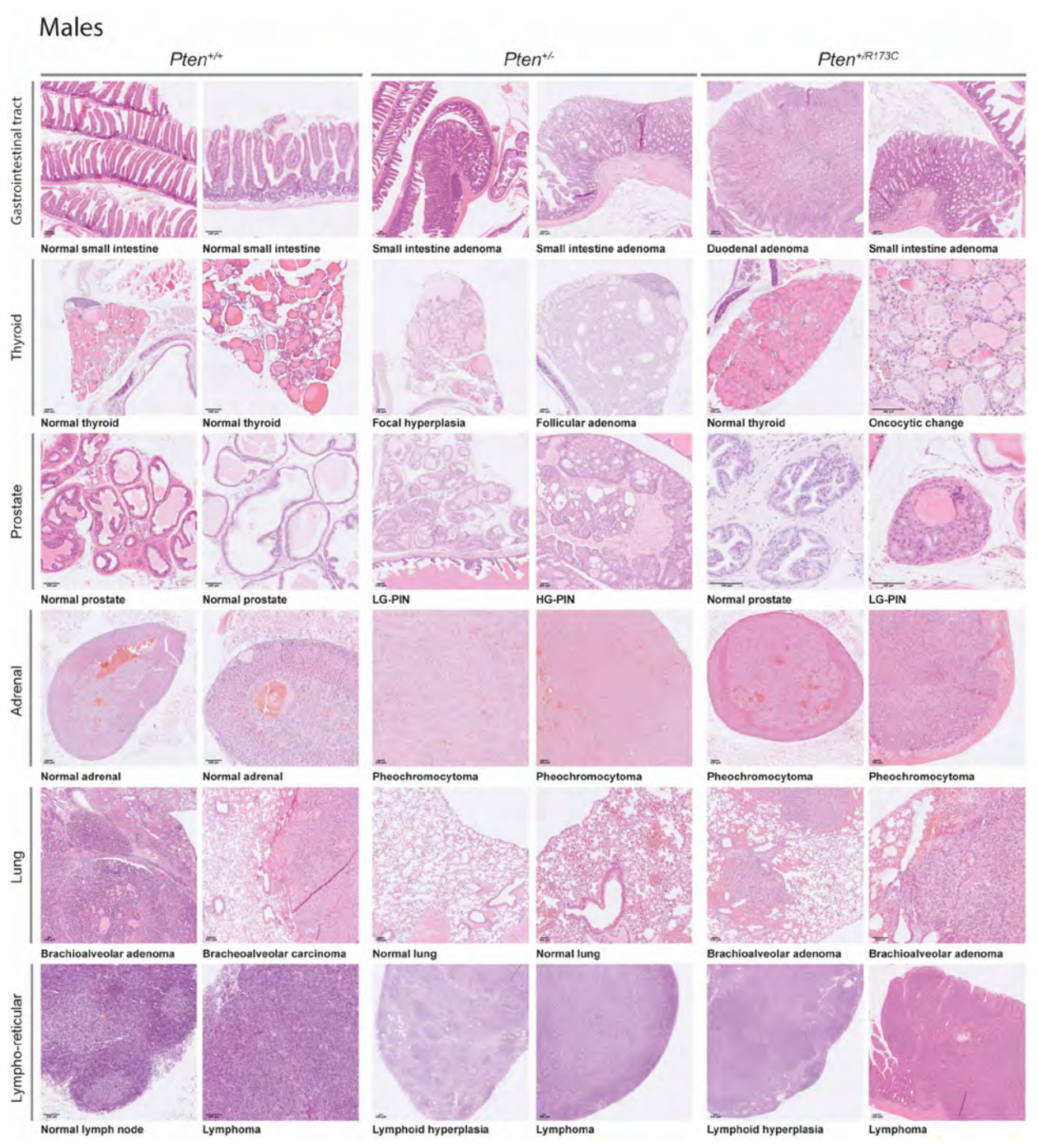


Fig. S11. Histopathological analysis of male $Pten^{+/R173C}$ mice. $Pten^{+/R173C}$ and $Pten^{+/-}$ mice, and their littermate control $Pten^{+/+}$ mice, on a mixed C57BL/6J x Sv129 background were allowed to age. Mice were euthanised for welfare reasons (ill health or masses with a combined size of \geq 1.4 cm² surface area) or at a specified age. Representative photomicrographs of H&E-stained sections of indicated tissues from male mice. Scale bar 100 μ m

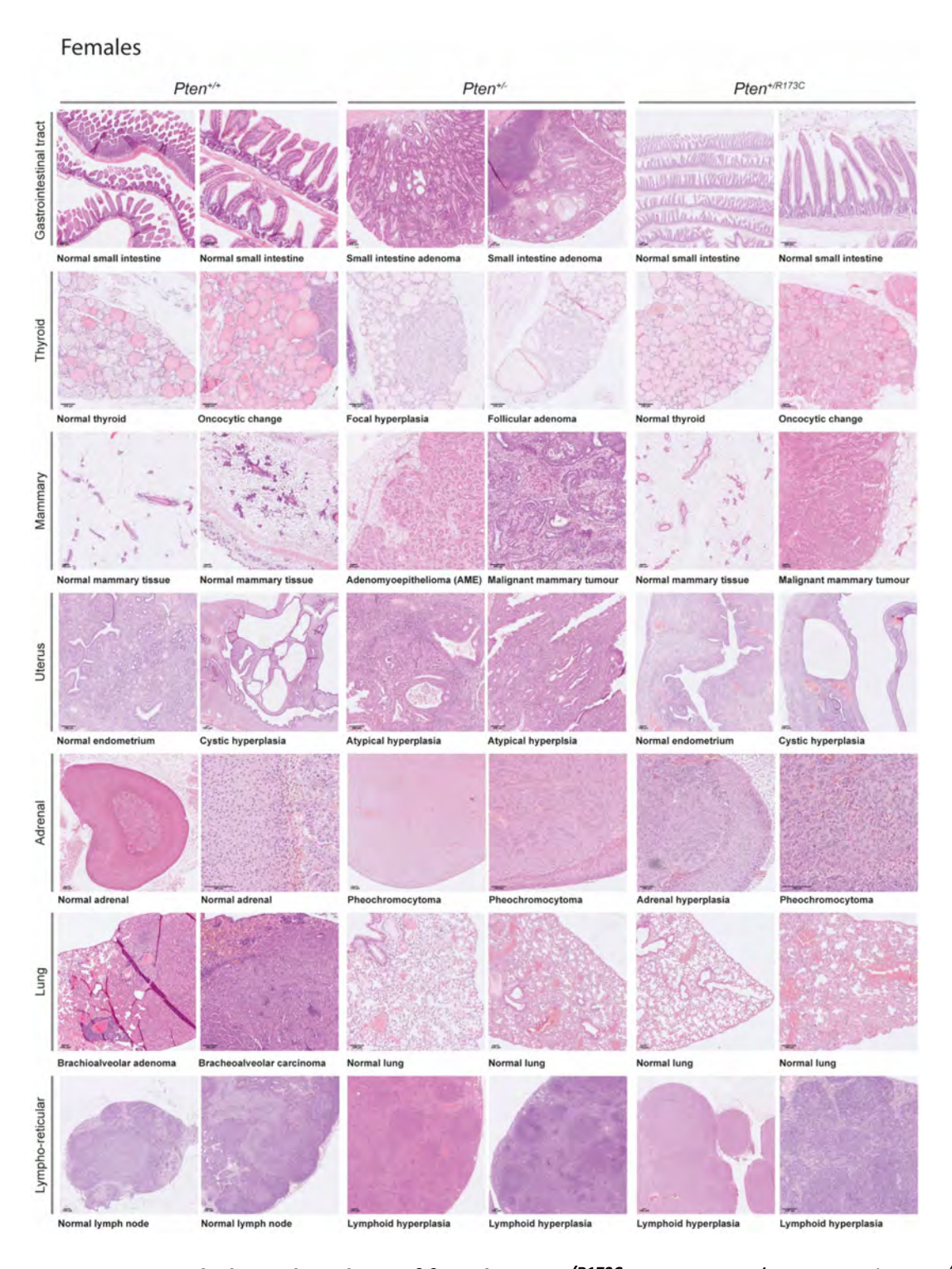
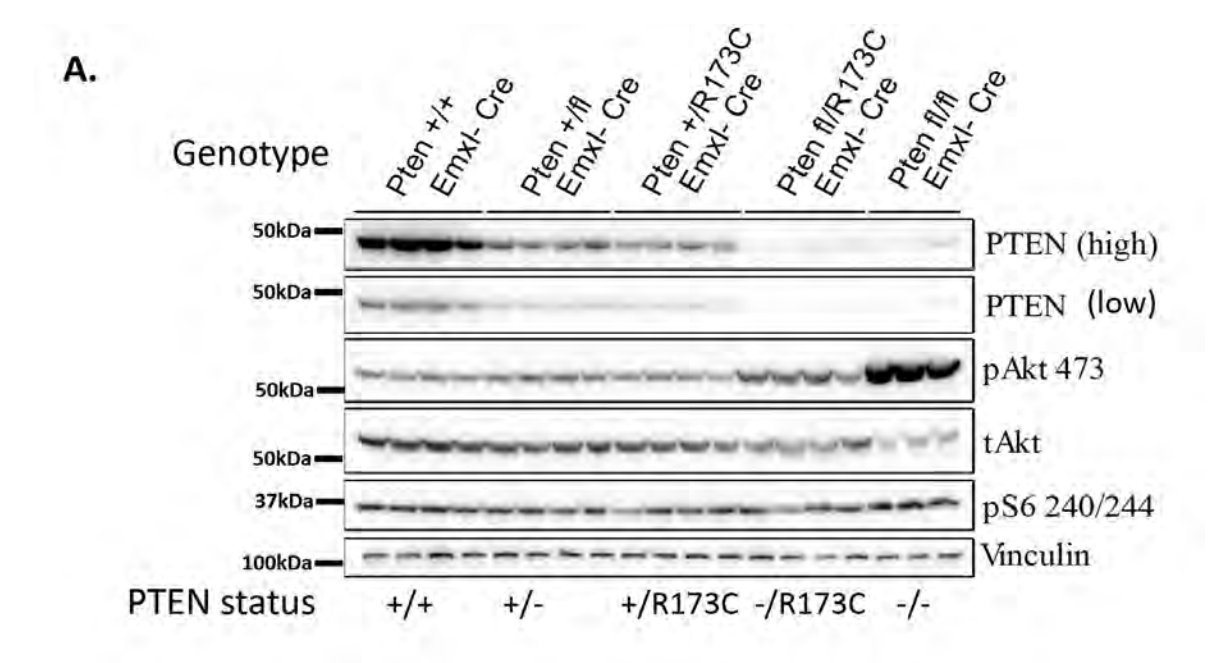


Fig. S12. Histopathological analysis of female $Pten^{+/R173C}$ mice. Pten+/R173C and $Pten^{+/-}$ mice, and their littermate control $Pten^{+/+}$ mice, on a mixed C57BL/6J x Sv129 background were allowed to age. Mice were euthanised for welfare reasons (ill health or masses with a combined size of ≥ 1.4 cm² surface area) or at a specified age. Representative photomicrographs of H&E-stained sections of indicated tissues from female mice. Scale bar 100 μ m



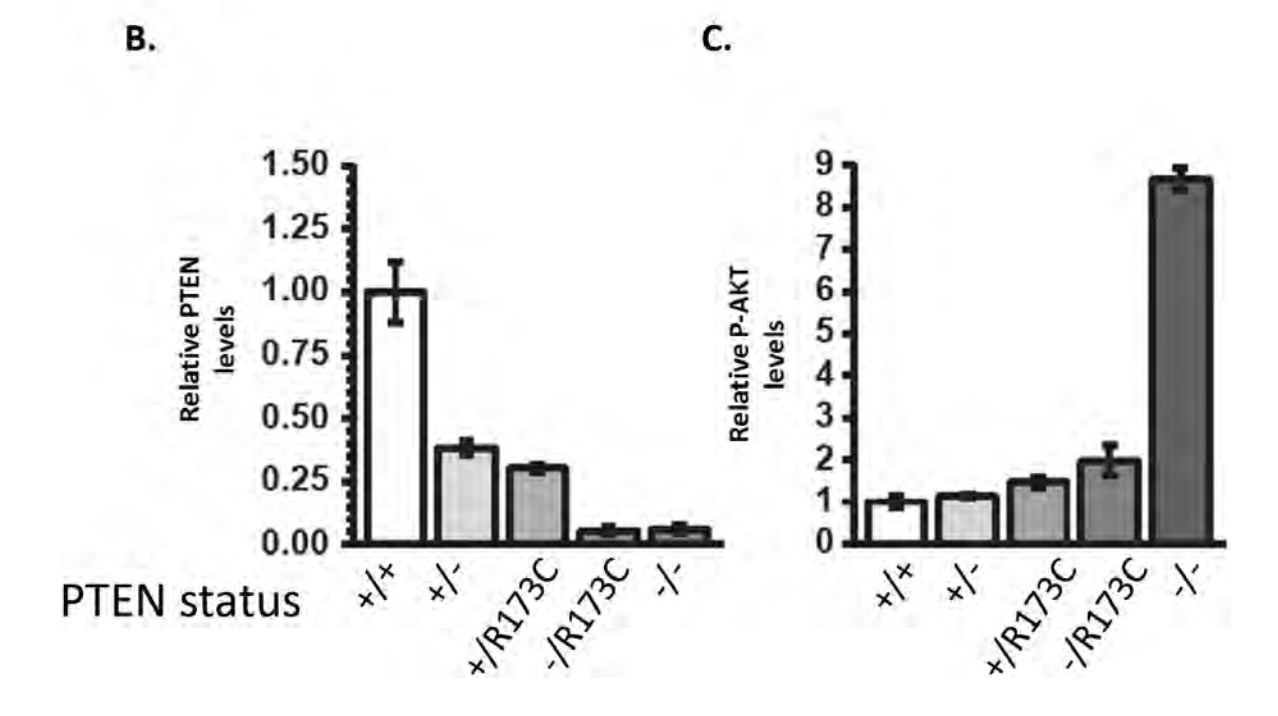


Fig. S13. Expression of PTEN and downstream pathway component in brain cortical lysates. (A) Immunoblots of PTEN protein and downstream PI3K pathway components in cortico-hippocampal lysates of postnatal pups (P1/P2) from the indicated genotypes. (B) Quantification of PTEN protein, normalised to the vinculin loading control. Data show mean±SEM (C) Quantification of p-AKT normalised to total AKT. n=4 for all mutants except for *Pten*^{fl/fl};*Emx1-Cre* where n=3. Data show mean±SEM. All mice were on a C57BL/6J background

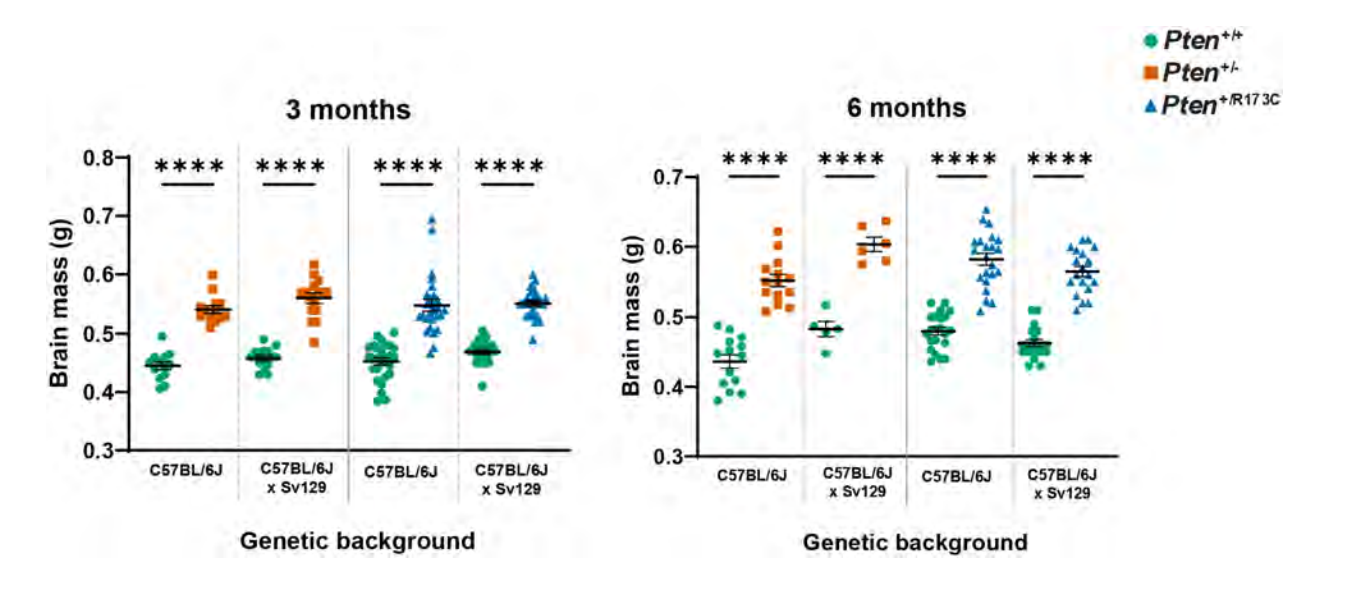
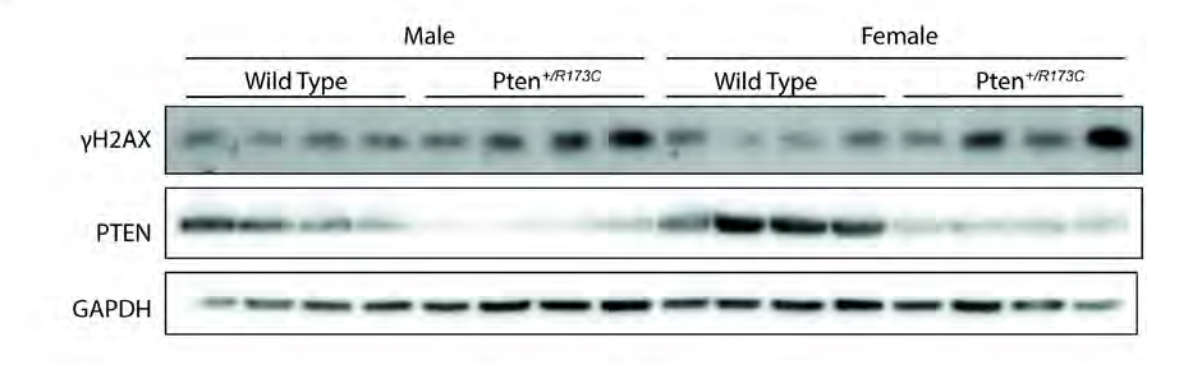
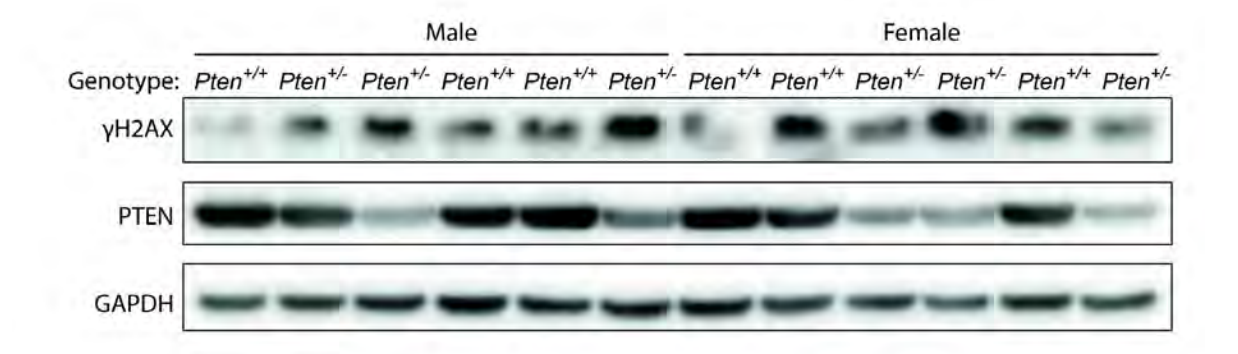


Fig. S14. Analysis of brain mass in mice. Brain mass of $Pten^{+/-}$, $Pten^{+/R173C}$ and $Pten^{+/+}$ littermate controls of both sexes at 3 and 6 months of age on the indicated genetic backgrounds. Data show mean \pm SEM, statistical analysis done using One-way ANOVA followed by Tukey's multiple comparison test, ****p<0.0001







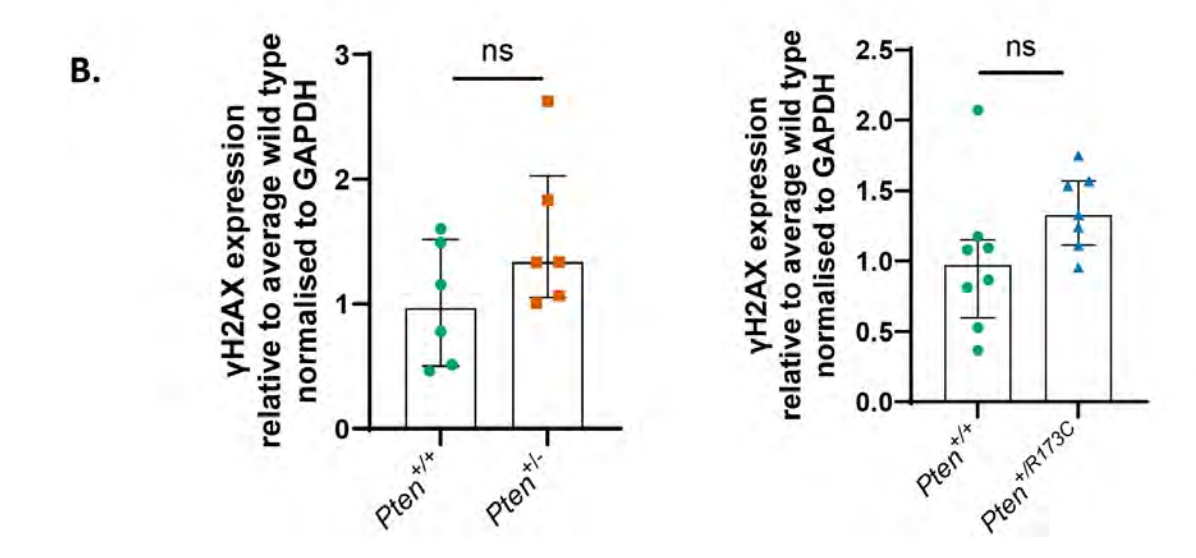


Fig. S15. *In vivo* characterisation of PTEN-R173C. (A) 6-week-old mice on a C57BL/6J background of the indicated genotypes were treated with 7Gy γ-radiation and protein extracts from brain were used for immunoblotting. Immunoblots showing levels of γH2AX. (B) Graphs show quantification of immunoblots. Bars show median with interquartile range. Pairwise comparisons were performed using Mann–Whitney U test. ns, not-significant (p> 0.05).

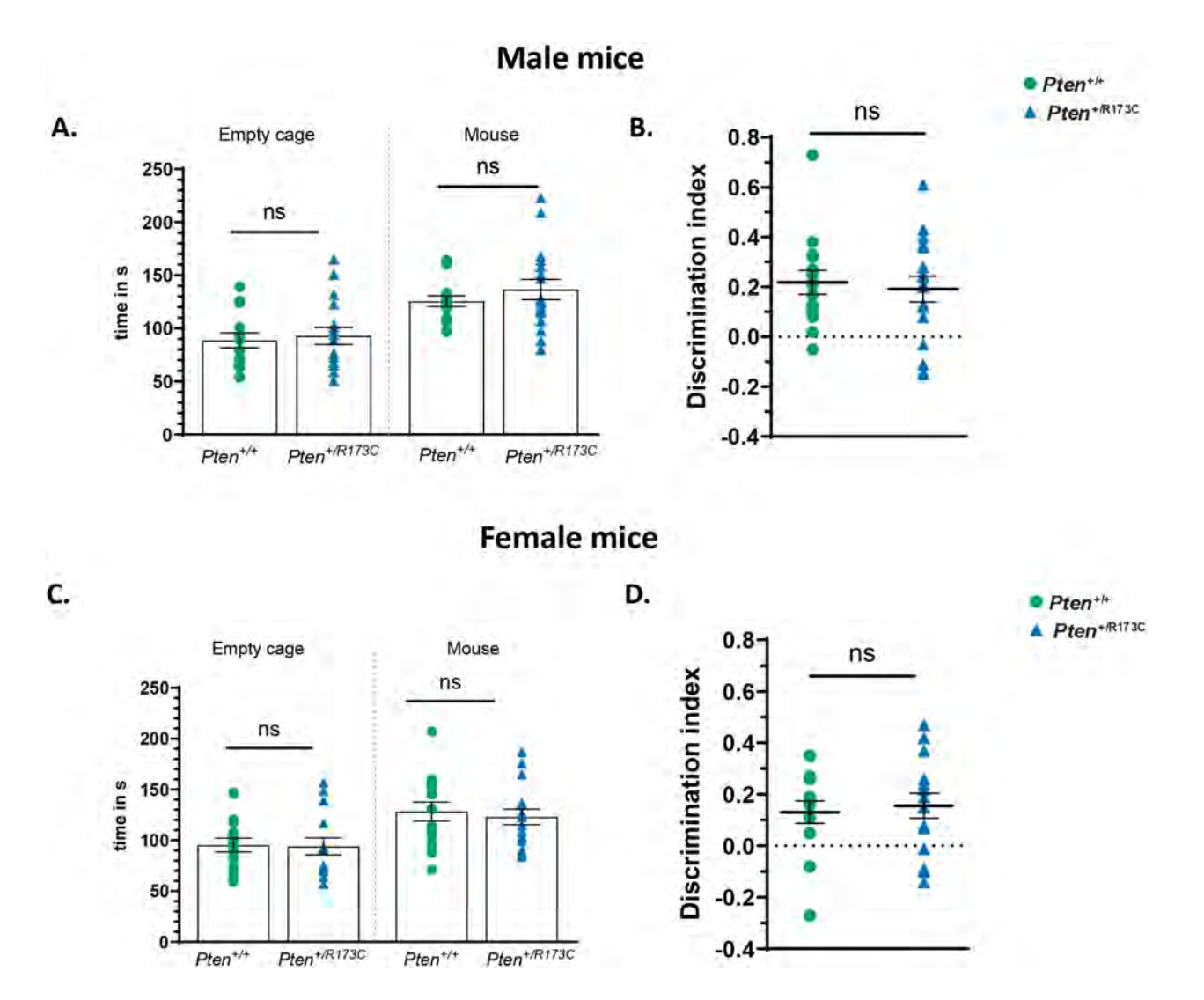
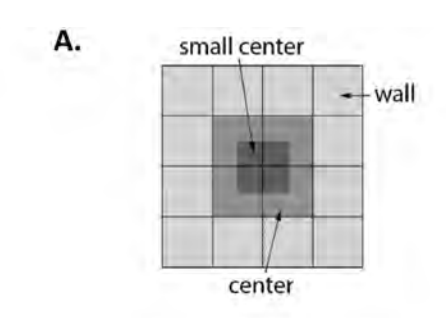
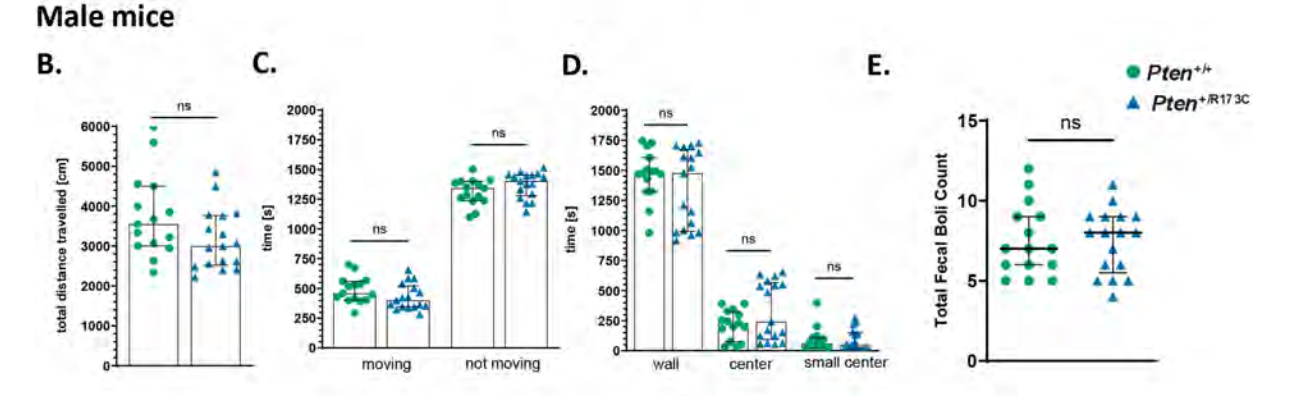


Fig. S16. Lack of sociability deficits in *Pten*^{+/R173C} mice in Crawley's sociability test. Analysis of sociability of male (A) and female (C) *Pten*^{+/R173C} mice and littermate controls. In Crawley's three chamber test, mice were analysed for their preference of a mouse versus an empty cage. Data show mean±SEM analysed using Ordinary one-way ANOVA. (B and D) Discrimination indexes for male and female WT and *Pten* mutant animals analysed in A and C. Males: n=14 for *Pten*^{+/+} and n=17 for *Pten*^{+/-} *R173C* mice. Females: n=16 mice of each genotype. Data show mean SEM, statistical analysis done using Unpaired Student's t-test. ns, not-significant (p>0.05).





Female mice

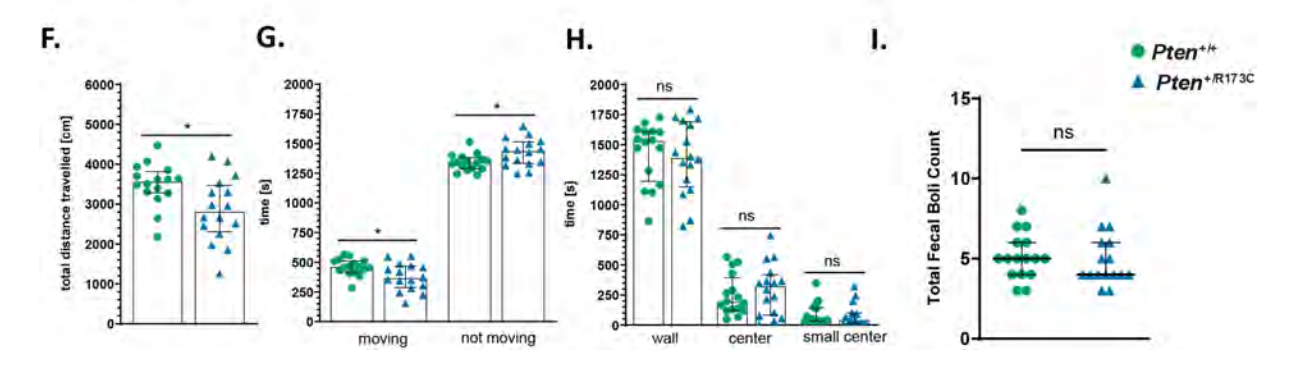


Fig. S17. Female $Pten^{+/R173C}$ mice show reduction in exploratory locomotion in the open field test. (A). Scheme of the open field arena. Parameters measured in the open field test for male (B, C, D and E), and female (F, G, H, I) $Pten^{+/R173C}$ mice and their littermate WT controls. Total distance travelled (B and F), time spent moving and not moving (C and G), time spent in each of the three zones as indicate in A (D and H) and defecation during the test (E and I). There were no differences between $Pten^{+/R173C}$ and control male mice. Female $Pten^{+/R173C}$ mice spent less time moving and travel smaller distances compared to their WT littermate controls indicating possible exploratory locomotion deficits. Males: n=15 for WT and n=17 $Pten^{+/R173C}$ mice. Females: n=16 mice of each genotype. Data show median with interquartile range. Two-tailed Mann-Whitney U test. p-values : *p< 0.05; ns, not-significant (p>0.05).

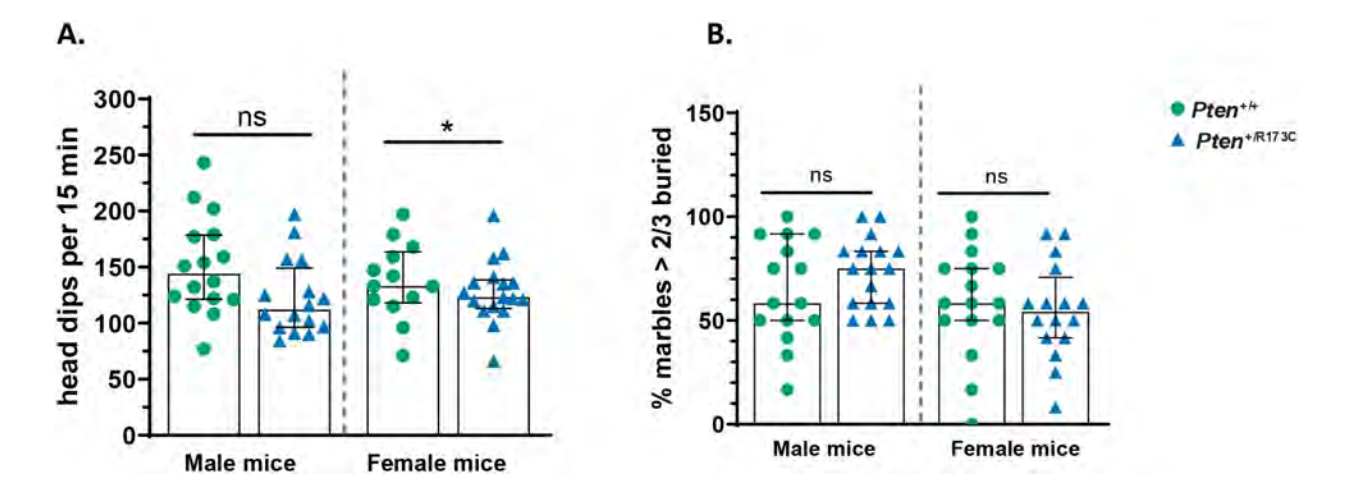


Fig. S18. Female $Pten^{+/R173C}$ mice show reduction in exploratory locomotion in the hole board test. (A). Hole board test: female $Pten^{+/R173C}$ mice made significantly fewer head dips than $Pten^{+/+}$ littermate controls. Males: n=13 $Pten^{+/+}$ and 17 $Pten^{+/R173C}$ mice. Females n=16 mice per genotype. Data show mean \pm SEM. Two-tailed Mann-Whitney U test. *p<0.05. (B). Marble Burying test: there was no significant difference between $Pten^{+/R173C}$ and $Pten^{+/+}$ controls of either sex in this test. Males: n=15 for $Pten^{+/+}$ and n=17 for $Pten^{+/R173C}$ mice. Females n=16 mice per genotype. Data show median with interquartile range. Two-tailed Mann-Whitney U test. p-values: *p<0.05; ns, not-significant (p>0.05).

Table S1. Clinical findings of PHTS patients with nuclear excluded but catalytically active PTEN variants

Available for download at

https://journals.biologists.com/dmm/article-lookup/doi/10.1242/dmm.052527#supplementary-data

Table S2. Clinical findings of PHTS patients with PTEN-R173 mutations

Available for download at

https://journals.biologists.com/dmm/article-lookup/doi/10.1242/dmm.052527#supplementary-data

Table S3. Reason for euthanasia of *Pten*^{+/+}, *Pten*^{+/-} and *Pten*^{+/R173C} mice

Available for download at

https://journals.biologists.com/dmm/article-lookup/doi/10.1242/dmm.052527#supplementary-data

Table S4. Frequency and grade of lesions in male mice

Available for download at

https://journals.biologists.com/dmm/article-lookup/doi/10.1242/dmm.052527#supplementary-data

Table S5. Frequency and grade of lesions in female mice

Available for download at

https://journals.biologists.com/dmm/article-lookup/doi/10.1242/dmm.052527#supplementary-data

Table S6. Frequency and grade of genetic background specific and immune findings in male mice

Available for download at

https://journals.biologists.com/dmm/article-lookup/doi/10.1242/dmm.052527#supplementary-data

Table S7. Frequency and grade of genetic background specific and immune findings in female mice

Available for download at

https://journals.biologists.com/dmm/article-lookup/doi/10.1242/dmm.052527#supplementary-data

Table S8. DNA constructs

Available for download at

https://journals.biologists.com/dmm/article-lookup/doi/10.1242/dmm.052527#supplementary-data

Table S9. Primers for site-directed mutagenesis

Available for download at

https://journals.biologists.com/dmm/article-lookup/doi/10.1242/dmm.052527#supplementary-data

Table \$10. Primers used for genotyping

Available for download at

https://journals.biologists.com/dmm/article-lookup/doi/10.1242/dmm.052527#supplementary-data

Table S11. Antibodies used

 $A vailable\ for\ download\ at \\ https://journals.biologists.com/dmm/article-lookup/doi/10.1242/dmm.052527 \# supplementary-data$

Table S12. qRT PCR primers

Available for download at https://journals.biologists.com/dmm/article-lookup/doi/10.1242/dmm.052527#supplementary-data

Table S13. Statistical tests and p values

Available for download at https://journals.biologists.com/dmm/article-lookup/doi/10.1242/dmm.052527#supplementary-data